Computer-aided and Robot-assisted Radiofrequency Ablation of Large Liver Tumor

Duan Bin

(B. Eng., Harbin Institute of Technology)

A THESIS SUBMITTED

FOR THE DEGREE OF DOCTOR OF PHILOSOPHY

DEPARTMENT OF MECHANICAL ENGINEERING

NATIONAL UNIVERSITY OF SINGAPORE

2016

Declaration

I hereby declare that the thesis is my original work and it has been written by me in its entirety. I have duly acknowledged all the sources of information which have been used in the thesis.

This thesis has also not been submitted for any degree in any university previously.

Duan Bin

27 July 2016

Acknowledgements

First and foremost, I would like to express my sincere gratitude to my supervisors, Assoc. Professor Chui Chee Kong and Assoc. Professor Chua Kian Jon, Ernest, for their constant guidance and support in the past four years. I feel very lucky to be their student.

I would also like to thank all the people from my research group, including Dr. Wen Rong, Dr. Fu Yabo, Dr. Xiong Linfei, Mr. Chng Chin Boon, Dr. Nguyen Phu binh, Dr. Ho Yick Wai, Yvonne Audrey, Dr. Lee Chun Xiong, Mr. Agus Pratondo, Mr. Tan Xiaoyu, and many others for their discussions and comments on my research. My sincere thanks also goes to Mr. Sakthi, Mrs. Ooi and Mdm. Hamidah in the Control and Mechatronics Lab for their help in the past four years.

Last but not least, I would like to acknowledge the National University of Singapore (NUS) for giving me the opportunity to pursue my PhD degree at this prestigious university. I also want to thank the China Scholarship Council (CSC) for awarding me the scholarship during my PhD study.

This work is supported in part by Singapore-China 9th Joint Research Program (SG-CN JPR) Grant (WBS: R265-000-467-305).

Table of Contents

Summary

Liver tumor is one of the most common intra-abdominal malignancies. The traditional way for liver tumor treatment is liver resection, which means removal of a portion of the liver tissue that encapsulate the tumor. However, many patients are not physically fit for liver resection for various reasons such as unfavorable tumor anatomic location, inadequate liver reserve, or severe co-morbid conditions. For these patients, Radio-frequency ablation (RFA) serves as a very good alternative.

RFA is the most widely used minimally invasive method for non-resectable liver tumor patients. It destroys tumor by the heat generated from high frequency alternating current (in the range of 350-500 kHz). One limitation of RFA is that it can only treat a small volume of tumor each time due to the limited working range of most current RFA needles. For large liver tumors which can grow up to 10cm, multiple ablations are required to completely destroy the whole tumor volume. However, it is a difficult task for clinician to perform multiple RFAs percutaneously due to the poor quality of the feedback image during the procedure. In addition, accurate and consistent insertion of multiple RFAs is also hard for the clinician. A solution to these problems is using computer-aided and robot-assisted RFA needle insertion system. In my study, several key issues, including RFA simulation and planning, design and control a robot for RFA needle insertion, and compensation of registration error, are researched.

RFA simulation and planning is necessary in preoperative stage. However, it is challenging to accurately simulate the shape and size of RFA lesion due to the intrinsic variations of the thermal-electrical properties of soft tissue. Current RFA simulation and planning methods ignore the variations of the tissue properties. Current RFA simulation and planning methods ignore the variations of the tis-

sue properties. Therefore, a probabilistic bio-heating finite element (FE) model is proposed and developed to predict the RFA lesion. Confidence levels of shape and size of lesion are generated by the FE model incorporated with mean-value first-order second-moment (MVFOSM) method. Based on the probabilistic FE method, a workflow of RFA planning is introduced to enable clinicians to preoperatively view the predicted RFA lesion in three-dimension (3D) within a hepatic environment.

The robot plays an important role in RFA needle insertion. To minimize the invasiveness, the RFA needle is expected to go through a single insertion port for multiple RFAs. This can be achieved by a specific manipulation of the needle named Remote Center of Motion (RCM). Previous RCM mechanism cannot achieve single insertion port (SIP) in RFA needle insertion due to their mechanical constraints. In this study, a novel RCM robot for RFA needle insertion is developed and a new analytical method, which overcomes the limitations of previous analysis, is proposed to model the kinematics of this robot. Combined position and velocity control is applied to control the robot.

Surgical registration refers to the process that determines the relationship among surgical images, patient and surgical tools. For robotic surgery, registration between patient and robot refers to the process to determine the position and orientation of patient coordinate system relative to the robot coordinate system. It can synthesize the preoperative planning data and the real surgical environment. The accuracy of the RFA needle insertion largely depends on the accuracy of registration. Most current registration methods focus on image registration. There is a lack of effective and efficient registration method between patient and robot. In this study, a novel marker-based registration method was proposed to transform the computed tomography (CT) image data to the robot coordinate system. This method establishes the transformation between the patient coordinate system and

robot coordinate system by finding the feature points of the patient marker using the robot. This method works well in our system but has limitations for other robot systems. Therefore, a generic vision-based registration was also proposed. The experiment results showed that both registration methods can achieve the required accuracy in RFA for liver tumor based on the clinician's claim.

List of Tables

List of Figures

Chapter 1

Introduction

1.1 Background and Motivation

Liver cancer is the fifth most common malignancy in men and the eighth in women worldwide [1]. Hepatic resection, which removes a portion of liver tissue encapsulating the tumor, offers the greatest potential for eliminating the tumor cells. However, hepatic resection creates large incision on both organ and patient, thus causing massive blood loss, post-operative complications and long-time recovery. Many patients are not physically fit for hepatic resection for various reasons such as unfavorable tumor anatomic location, inadequate liver reserve, or severe comorbid conditions [2]. For these patients, minimally invasive thermal therapies can be good alternatives for liver tumor treatment. Thermal therapy refers to the application of thermal energy to living tissues for increasing (or decreasing in the case of cryoablation) their temperatures to achieve the therapeutic aim. It is widely used in tumor treatment. There are many types of thermal energy including Radiofrequency(RF) ablation (RFA), Ultrasound ablation, Laser ablation, Cryoablation and Microwave ablation.

Among the various thermal therapies, RFA is the most widely used minimally

invasive method for non-resectable liver tumor patients. It destroys tumor by the heat generated from high frequency alternating current (in the range of 350 – 500 kHz). The heat generated in the tissue could cause coagulation necrosis of the tumor so that tumor cells are eliminated. RFA can be performed in open surgery, laparoscopically or percutaneously. To minimize the invasiveness of RFA procedure, percutaneous RFA is usually performed. Percutaneous RFA means inserting the RFA needle through the skin directly. It is usually performed under ultrasound guidance (as shown in Figure 1.1). Using ultrasound guidance, the clinician inserts a RFA needle through the skin and directly into the tumor. The generator is then activated and tumor cells around the RFA needle can be killed by the RFA heat.

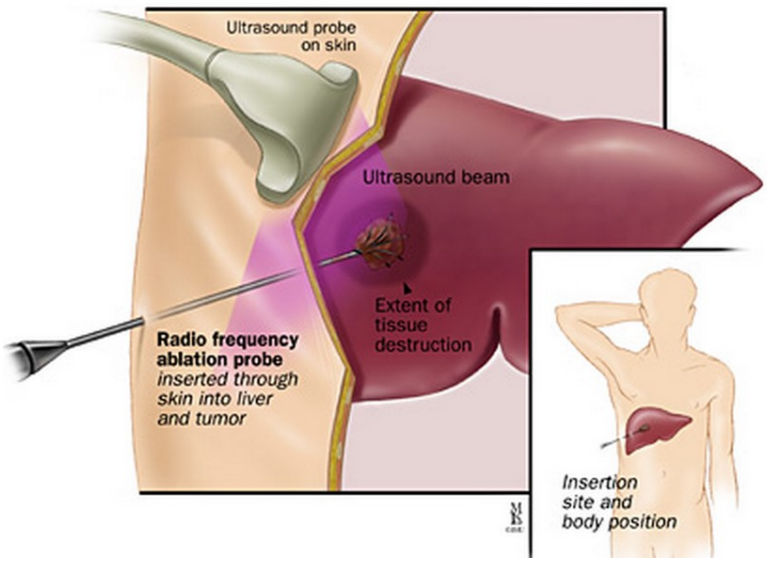

Figure 1.1: Illustration of percutaneous RFA procedure. (https://gi.jhsps.org/GDL_Disease.aspx?CurrentUDV=31&GDL_Cat_ID=AF793A59-B736-42CB-9E1F-E79D2B9FC358&GDL_Disease_ID=A349F0EC-5C87-4A52-9F2E-69AFDB80C3D1)

Therapeutic effect of percutaneous RFA therapy is challenged by the following problems. Firstly, it is difficult to provide a clear guidance for the clinician during multiple RFAs. RFA can only treat a small volume of tumor each time due to the limited spreading range of most current RFA needles [3]. Multiple ablations are

thus required for large liver tumors which can grow up to 10cm or more in length. Since human tissue contains water, RFA could cause numerous micro-bubbles of gas in the heated tissue[4, 5]. These micro-bubbles will blur the images and make insertion of RFA needle to target points a very difficult task for the clinician. Secondly, it is very hard for the clinician to insert the RFA needle to the target points as planned accurately. The insertion of RFA needle largely depends on the experience of the clinician. They can only rely on their experience to decide where to insert the needle and how deep to go. Thus to achieve high accuracy and consistency for percutaneous RFA needle insertion is challenging. Considering the problems in current percutaneous RFA therapy, a computer-aided and robot-assisted RFA needle insertion system for percutaneous RFA of large liver tumor is investigated.

1.2 Overview of Computer-aided and Robot-assisted RFA Needle Insertion System

A computer-aided and robot-assisted RFA needle insertion system should include the following components: RFA simulation, preoperative modeling and planning, registration, and robot execution (as shown in Figure 1.2). Firstly, a reliable RFA simulation should be conducted to give the clinician a guidance of the size and shape of RFA lesion. Based on the RFA simulation results and the medical images of the patient, the patient specific model is constructed and RFA planning is built. The next step is surgical registration. Since the preoperative planning data is based on the patient coordinate system, it can not be used directly by the RFA needle insertion robot. Registration is a process that builds a map between these two coordinate system. The last step of the computer-aided and robot-assisted RFA needle insertion is robot execution. In this process, the

robot read the preoperative planning data and execute the task accordingly. A user-friendly interface should also be provided to allow the clinician to control the execution process.

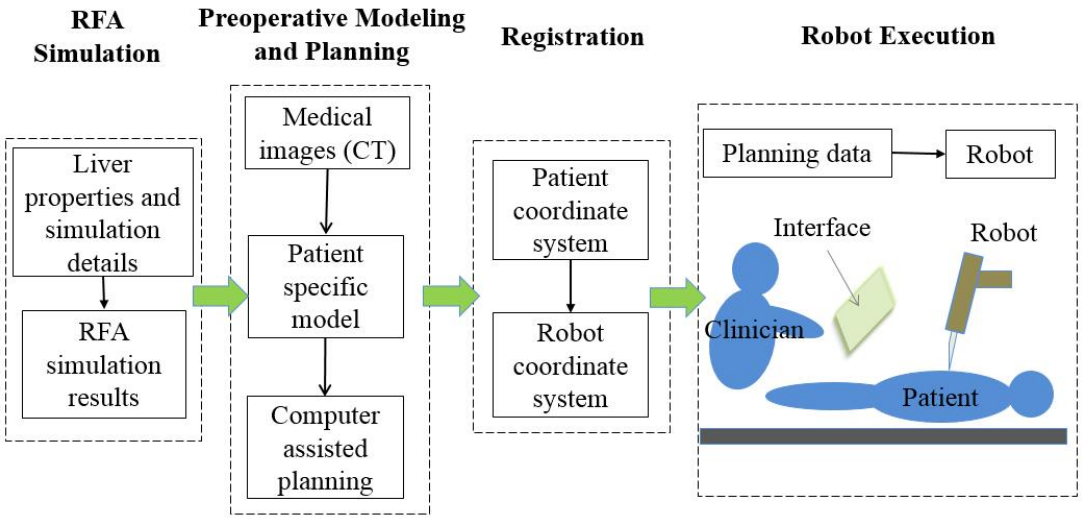

Figure 1.2: Components of a computer-aided and robot-assisted RFA needle insertion system.

With the help of the computer-aided and robot-assisted RFA needle insertion system, the effect of micro-bubbles on misguidance of needle placement could be counteracted and the insertion accuracy and consistency can be increased. Some key issues about the computer-aided and robot-assisted RFA needle insertion system need to be further researched.

Firstly, reliable RFA simulation for preoperative RFA planning is challenging. The clinician does not know how much lesion volume is created by the RFA procedure. RFA simulation significantly depends on thermal-electrical properties of liver tissue such as thermal conductivity, tissue density, specific heat, blood perfusion rate and electrical conductivity. However, thermal-electrical properties of soft tissue are often subjected to inherent variations due to anatomic microstructural differences and individual patient differences [6–11]. Hence, it is important to consider the variation of the thermal-electrical properties in RFA sim-

ulation. In this case, a reliable RFA simulation and planning method is required to guarantee the accuracy and safety of percutaneous RFA therapy.

Secondly, an effective RFA needle insertion robot for large liver tumor treatment is still not available. To minimize the trauma imposed on patient body, the RFA needle is expected to go through a Single Insertion Port (SIP) for multiple needle insertions (as shown in Figure 1.3). This can be achieved using a specific manipulation of the needle named Remote Center of Motion (RCM) [12–14]. RCM has been defined as the center of rotation fixed at a point (usually the insertion point in minimally invasive surgery(MIS)) where no mechanical component exists [15]. Ideally, the remote center of the RCM mechanism is coincident with the insertion port so that the RFA needle always pass through the insertion port no matter how we rotate the needle. Commercially available robot systems, such as da Vinci and ZEUS, are commonly used in robotic surgeries. Both systems consist of a console for the surgeon and several robotic arms. The da Vinci system has four robotic arms and ZEUS system has three arms. However, these systems are expensive and some robotic arms are not required and hence, redundant in the application of RFA. There are robots developed specially for RFA [16, 17], but these robots are bulky and cannot achieve SIP in RFA of large liver tumor treatment due to their mechanical constraints. Therefore, an effective RFA needle insertion robot that can achieve SIP for large liver tumor treatment has to be developed.

Thirdly, accurate registration among surgical robot, patient and computed image is a challenging task. Most existing registration methods and algorithms focus on image registration (i.e. registration between two sets of computer image or between computer image and real environment). However, registration in robotic surgery is not only limited to image registration, but also includes registration among surgical robot, patient and computer image. Therefore, an accurate registration method for robotic surgery, especially between surgical robot and patient

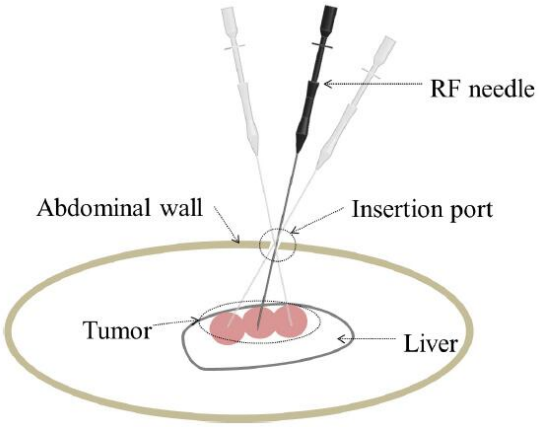

Figure 1.3: Multiple RFA needle insertions through a single insertion port.

is required.

1.3 Objective and Scope

The objective of this study is to research and develop a computer-aided and robot-assisted RFA needle insertion system to improve the treatment outcome of percutaneous RFA. To be specific, the following goals will be achieved in my study:

- A generalized probabilistic bio-heating finite element (FE) model which takes into consideration the intrinsic variations of human tissue properties will be developed to determine the probabilistic distribution of the shape and size of RFA lesion. Based on the probabilistic simulation, an ablation planning strategy for manual or robot-assisted operation will be proposed.

- A surgical robot which can manipulate multiple RFA needle insertions through SIP will be designed and advanced control strategy will be developed for the RFA needle insertion robot.

- An effective registration method for our RFA needle insertion system will be proposed.

This study focuses on the percutaneous RFA of large liver tumor. Our research is restricted to the preoperative simulation and planning, and the intra-operative execution. The postoperative examination and analysis is beyond the scope of this study.

1.4 Thesis Contribution

The major contribution of this thesis can be summarized as follows:

- A computer-aided and robot-assisted RFA needle insertion system is designed and developed. Experiment of the prototype system on porcine model demonstrates its effectiveness for large liver tumor ablation.

- A probabilistic RFA simulation method is proposed. The method has improved the reliability of RFA simulation. Our probabilistic simulation method contributes to a better understanding of the intrinsic variations of biological tissue properties and may provide reference for other biological tissue related simulation.

- A spherical mechanism is proposed and investigated for robotic RFA needle insertion. By realizing RCM of the RFA needle, single port access can be achieved using this mechanism. A novel analytical method is used to accurately model the spherical mechanism.

- An effective marker-based registration method is proposed to register the pre-operative CT images with the robot coordinate system. A generic vision-based registration and calibration method is also proposed. Both registration methods are equally effective.

1.5 Thesis Organization

The theme of this thesis is developing a computer-aided and robot-assisted RFA needle insertion system for large liver tumor. Three key issues, i.e. preoperative simulation and planning, RFA needle insertion robot, and registration, will be covered in the remainder of this thesis. This thesis is organized into seven chapters.

Chapter 2 gives a detailed literature review of the three main topics related to computer-aided and robot-assisted RFA, i.e. researches on pre-operative RFA simulation and planning, intra-operative robotic RFA execution, and registration in surgery.

Chapter 3 describes a probabilistic bio-heating finite element (FE) model for prediction of the RFA lesion. This model takes into account the probabilistic nature of five thermal-electrical liver properties: thermal conductivity, liver tissue density, specific heat, blood perfusion rate and electrical conductivity. Based on the probabilistic FE method, a workflow of RFA planning is introduced to enable clinicians to pre-operatively view the predicted RFA lesion in three-dimension (3D) within a hepatic environment.

Chapter 4 presents a RCM robot mechanism which is able to conduct multiple RFA needle insertions covering the entire tumor volume through a Single Insertion Port (SIP). A spherical mechanism comprising two semi-circular arches were used to realize the RCM. Two motorized linear slides were incorporated into the system to achieve SIP. A novel analytical method for modeling this RCM mechanism was proposed. This method can overcome the limitation of previous method in existing literature. Integrative speed and position control strategy was implemented to allow the robot to move smoothly and precisely. Experiments were conducted to test the accuracy and feasibility of the RFA needle insertion robot.

Chapter 5 presents a manual registration method to transform the CT image

data to the robot coordinate system. This method works well in our system but has limitations for other robot systems. A vision-based registration, which can be used in general robot systems, was also proposed. The experiment results showed that both registration methods can achieve the required accuracy in RFA for liver tumor based on the clinician's claim.

Chapter 6 describes the ex-vivo and in-vivo experiments for the RFA needle insertion robot system. Preoperative RFA planning, registration, and robot execution were connected to test the whole system. The results demonstrate that our robot system is capable of accurately executing multiple RFAs of large liver tumor through SIP.

Chapter 7 concludes the dissertation and discusses possible improvements and directions for future work.

Chapter 2

Literature Review

This chapter reviews literature on computer-aided and robot-assisted RFA. Basics of RFA are introduced in the first section. The second section reviews researches related to preoperative RFA simulation and planning. Existing works on RFA simulation and planning and probabilistic Finite Element method are covered in this section. The third section introduces existing works on intraoperative RFA execution robot. Robotic surgery are introduced and remote center of motion (RCM) mechanism are reviewed in this section. Works on the surgical registration are introduced in the forth section. Research gap is identified by reviewing the literatures.

2.1 Basics of RFA

RFA is a minimally invasive procedure which applies high frequency alternating current (in the range of 350–500 kHz) to destroy tumor cells. By applying a voltage on the RFA electrode, an electric field is generated in the tissue. The electric field can induce electric force on the charged ions within the electrolytic medium of the tissue. This force causes friction between ions and the surrounding

fluid medium, generating heating effect thus leading to coagulative necrosis in the tissue.

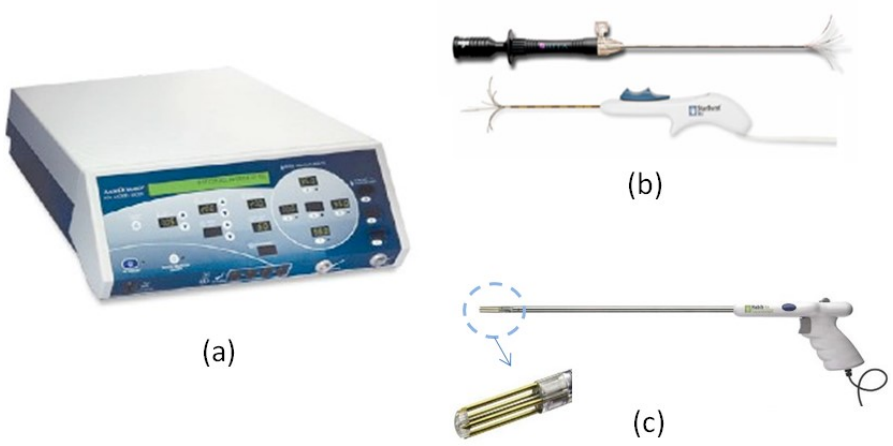

Figure 2.1: RFA devices: (a) RFA generator; (b) mono-polar RFA probe; (c) Bipolar RFA probe. ((http://www.angiodynamics.com/products/generator_and_hardware))

In general, an RFA system consists of an RFA generator and RFA probes (as shown in Figure 2.1). The RFA generator is used to provide high frequency RF power and RFA probes are needle electrodes which are inserted into the tissue during RFA. There are mainly two types of RFA probe: mono-polar RFA probe and bipolar RFA probe. Mono-polar probe is always used together with an grounding pad which is placed on the patient skin. The current enters human body from the electrode tip and flows through the body then exits from the grounding pad. The current density is highest around the electrodes and decreases as the current flows out the body. Therefore, the Joule-heating effect mainly occurs around the electrodes. Monopolar probes are always small and slim, hence suitable for percutaneous or laparoscopic RFA treatment. Bipolar probe has both positive and negative electrodes for current flow. It can be used individually and does not require a grounding pad. Since the electrical field caused by the bipolar probe is between the positive and negative electrodes, the current density is higher than

that of mono-polar probe and thus the heating is more efficient. Bipolar RF probe is commonly used in open surgery.

RFA is commonly used for tumor treatment as a form of direct treatment. Tumor cells are directly killed by the heat created during RFA procedure. However, some studies indicate that RFA can also be used to assist liver resection. Liver resection, which removes a portion of liver tissue encapsulating the tumor, is the gold standard for liver tumor treatment. A crucial goal in liver resection procedure is to minimize the blood loss for best treatment survivability. Jiao et al reported a surgical procedure which uses RFA in liver resection to reduce the blood loss [18]. This surgical procedure started by performing RFA on the preplanned line of resection to generate a coagulated zone, then followed by a manual resection using the surgical scalpel.

RFA is efficient for small tumor treatment. It can also be used in the treatment for large tumors (up to 10cm or more in length). Full coverage of large tumor could be achieved by overlapping RFA lesion zone in tissue [17], and many methods have been developed to increase the RFA lesion. Livraghi et al reported that saline injection can help increasing the RFA lesion zone by increasing the electrical conductivity [19]. Goldberg et al found that cooled-tip electrodes can help to reduce charring and thus enlarge the lesion [20]. McGahan et al developed a bipolar array to increase the RFA lesion [21].

2.2 RFA Simulation and Planning

In clinical RFA, one challenging problem is to determinate the complete temperature field and lesion size throughout both tumor and normal tissue. Since RFA devices can only sample the temperature at limited locations during the process, the temperature remains unknown in most part of the tissue. Similarly, it

is necessary to predict the temperature field and lesion size in pre-operative RFA planning so that the treatment can be optimized. Computer simulation provides us a way to predict the temperature field and make a proper ablation plan. Researches about RFA simulation and planning will be reviewed in this section.

2.2.1 Existing works on RFA simulation and planning

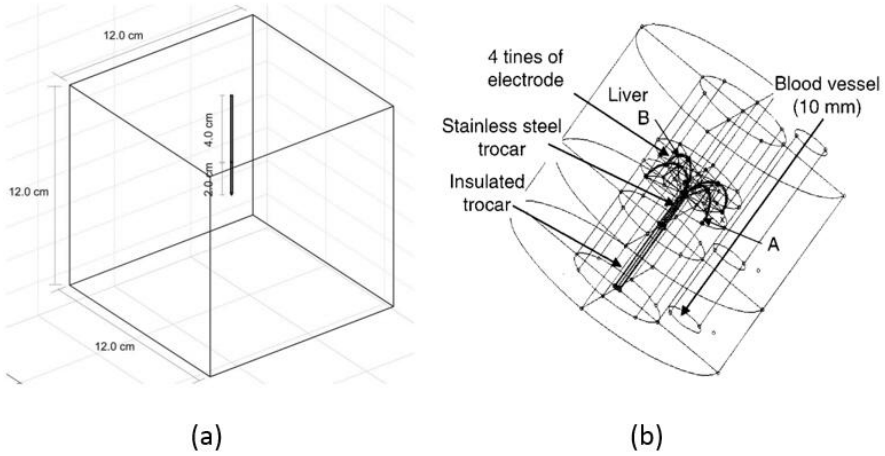

Figure 2.2: Two commonly used geometries for tissue modeling in 3D RFA simulation. (a) The cube model in Chang's simulation [22]. (b) The cylinder model in Tungjitkusolmun's simulation [23].

RFA in human tissue is a very complex process and it is impossible to reproduce this process accurately in computer simulation. All RFA simulations start with the simplification of the real physical situation. Firstly, the geometry of the simulation model is always simplified. Cube and cylinder are two commonly used geometry to model the tissue in 3D finite element analysis of RFA (see Figure 2.2). Chang used a 12.0 cm $\times$ 12.0 cm $\times$ 12.0 cm cubic region to simulate the surrounding tissue in a finite element analysis of hepatic RFA [22]. Jain and Wolf also used a cube to model the tissue in his finite element model of RFA [24]. Tungjitkusolmun et al used a cylinder to model the hepatic tissue in a 3D finite element simulation of RFA [23]. Similar cylinder model can be found in [25, 26].

In some studies, symmetric planes or axes were used to simplify the 3D model into a two dimensional model when the model is symmetric [27–36]. Some studies even simplified this physical problem into a single dimension [37, 38]. Secondly, it is common to consider only the most significant tissue and ignore the microscopic structures such as nerves, glands etc. Only the thermal and electrical properties for the whole tissue are available in the literature.

RFA simulation involves the electrical-thermal heating phenomenon. The spatial temperature distribution in the tissue can be obtained by solving a Bio-heat equation proposed by Pennes [39].

$$\rho c \frac{\partial T}{\partial t} = \nabla \cdot k \nabla T + q - Q_p + Q_m, \tag{2.1}$$

where ρ is the density (Kg/m^3), T is the temperature (K), c is the specific heat ($J/Kg{\cdot}K$), k is the thermal conductivity ($W/m{\cdot}K$), q is the heat source (W/m^3), Q_p is the perfusion heat loss (W/m^3), and Q_m is the metabolic heat generation (W/m^3). T, q, Q_p, and Q_m are all scalar fields on three-dimensional Euclidean space. A scalar field associates a scalar value to every point in a space. ∇T means the gradient of T, it can be represented as:

$$\nabla T = grad\ T = \frac{\partial T}{\partial x}\hat{i} + \frac{\partial T}{\partial y}\hat{j} + \frac{\partial T}{\partial z}\hat{k}, \tag{2.2}$$

where $\hat{i}$, $\hat{j}$, $\hat{k}$ are the unit vectors in the Cartesian coordinates. The gradient of T is a vector field. Let $\vec{T} = T_x\hat{i} + T_y\hat{j} + T_z\hat{k}$ denote the gradient of T. The divergence of the vector field $\vec{T}$ is a scalar function that can be represented as:

$$\nabla \cdot \vec{T} = div\vec{T} = \frac{\partial T_x}{\partial x} + \frac{\partial T_y}{\partial y} + \frac{\partial T_z}{\partial z}. \tag{2.3}$$

Thus, $\nabla \cdot k\nabla T$ in Equation 2.1 results in a scalar field on three-dimensional

Euclidean space. The metabolic heat generation Q_m can be ignored since it has been shown to be insignificant for ablation in [40–42]. The perfusion heat loss Q_p plays an important role in RFA of high perfusion tissues, such as liver [22, 23, 25, 34, 38, 43–45]. But it can be ignored in RFA of non-vascular tissues, such as cornea [46–48]. Q_p can be calculated by:

$$Q_p = \rho_{bl} c_{bl} \omega_{bl} (T - T_{bl}), \tag{2.4}$$

where ρ_{bl} is the blood density (Kg/m^3), c_{bl} is the blood specific heat ($J/Kg{\cdot}K$), ω_{bl} is the blood perfusion rate (s^{-1}) and T_{bl} is the blood temperature (K).

As indicated in [49, 50], the tissues can be considered purely resistive at the frequency of RFA (300 kHz-1 MHz). Then the electric field in tissue can be calculated using a quasi-static approach. The heat source q caused by Joule heating effect can be calculated by

$$q = J \circ E, \tag{2.5}$$

where J is the current density (A/m^2), and E is the electric field intensity (V/m), J and E have the same dimensions and $\circ$ means Hadamard product of two matrices. It produces another matrix where each element ij is the product of elements ij of the original two matrices. These two scalar fields should meet the requirements of the Laplace's equation:

$$\nabla \cdot \sigma \nabla V = 0 \tag{2.6}$$

where V is the voltage (V) and σ is the electrical conductivity (S/m), V is a scalar field and $\nabla \cdot \sigma \nabla V$ is also results in a scalar field.

FE simulation for liver tumor RFA has been reported in literatures. Ahmed [51] investigated the combined effects of varying perfusion, electrical and thermal conductivity on RFA heating using an established computer simulation model

of RFA. Varying electrical and thermal conductivities were assigned to tissue, fats and saline injection to represent their different thermal-electrical properties. Haemmerich et al [45] studied the differences between monopolar and bipolar RFA devices using a FE model. Their results showed that the bipolar RFA device could create larger lesions. Compared to monopolar RFA heating, bipolar RFA heating is more robust and less dependent on inhomogeneity of liver tissue thermal-electrical properties. Chang and Nguyen [25] used a two-dimensional (2D) FE model to simulate RFA process in soft tissue. The model was integrated with a self-updating structure which updates thermal conductivity and blood perfusion during simulation. Haemmerich et al [44] conducted a FE study of RFA induced coagulation zones close to blood vessels. They concluded that the recurrence rates of tumor cell close to blood vessels could be reduced by bipolar RFA through increasing current density and heat deposition in the perivascular spaces. Tungjitkusolmun et al [52] investigated effects of changing myocardial properties in cardiac RFA using FE modeling. Their results showed that changes of myocardial properties affect the results of the FE analysis of power-controlled RFA more than those of temperature-controlled RFA. Kröger et al [53] presented a novel method to predict the vascular cooling effect in RFA simulation. A look up table was used to store the results of vascular cooling effect which depends on radius of blood vessel and distance of RFA applicator from the vessel.

In order to completely destroy large tumors, Chen et al [54] adopted mathematical protocol to optimize the process of RFA planning. Different overlapping modes were introduced for different sizes of tumors. The objective of this method was to achieve safety margin of 5 mm with adequate overlapping. One-ablation, six-ablation and 14-ablation models were proposed in Dodd et al [55] for large tumor RFA planning. Ablation spheres were optimally overlapped in order to achieve maximum coverage volume with a 10 mm tumor free-margin. Nicolau et

al [56] proposed an augmented reality-based planning method for liver ablation. Their system was evaluated in both phantom and clinical studies. The maximum errors for phantom and clinical studies are below 2 mm and 5 mm respectively. The results are favorable since radiologists claim that an accuracy better than 5mm can avoid destroying too much healthy cells. Khajanchee et al [57] explored the relationship between tumor size and smallest number of ablations for complete tumor destruction. Assuming that the tumor and ablation lesions have a perfect spherical shape, they computed the required number of ablations for different tumor sizes and concluded that the minimum number of ablations for complete tumor destruction increases significantly as the tumor size increases. Baegert et al [58] presented a trajectory planning for hepatic RFA. Some practical constraints were brought into this study. Their method could achieve a satisfactory result regarding different constraints. Yang et al [17] presented a robotic navigation system for large liver tumor ablation. Overlapping ablation technique was used for needle path planning. The ablation lesion was treated as a perfect sphere with constant size. The navigation system was tested through an animal experiment. Their results showed good ablation accuracy with an average 1.5 mm deviation between ablated zone and tumor. Altrogge and Preusser [59] presented an optimization method for probe placement during RFA which considers the uncertainty of biophysical tissue properties. Their results showed significant sensitivity of the temperature with respect to variations in tissue properties.

2.2.2 Probabilistic Finite Element method

When the input parameters to a finite element (FE) analysis have some variations, probabilistic analysis should be integrated to the FE model to obtain the variations and confident levels of the results. Probabilistic finite element method broadly refers to the method that can integrates conduct probabilistic analysis in

a FE study.

Probabilistic uncertainty analysis was mainly used to solve structural engineering problems [60, 61] while it recently draws interests in the field of biomedical applications. Hu [62] studied the behavior of human placenta tissue using stochastic FE analysis. Visco-hyperelastic material parameters with statistical nature were utilized. They showed agreement between simulated results and actual data. Delalleau [63] applied stochastic method to determine elastic property of skin which was modeled by a classic single layer hyperelastic model and a double layer Neo-Hookean potential model. They concluded that the stochastic method had potential in solving optimization problems. In the study conducted by Santos [64], they proposed a probabilistic FE method to model the variations of tissue thermal-electrical properties. The probabilistic model was based on a simple two-dimensional monopolar electrode model. Their results showed that blood perfusion rate and thermal conductivity account for more than 95% of the variability in coagulation zone volume. Huang and Chui [65] described a preliminary RFA planning system using stochastic FE method by which the inherent variations of physical properties of the liver tissue was discussed.

Since the thermal-electrical properties of soft tissue are subjected to inherent variations due to anatomic microstructural differences and patient individual differences [6–11], it is important to consider the variations of the thermal-electrical properties in RFA simulation. The variations of the thermal-electrical properties need to be modeled and a probabilistic FE method needs to be developed to predict the variations of RFA results.

2.3 Robot-assisted RFA Needle insertion

2.3.1 Robot in surgery

Surgical robot is defined as 'a powered computer controlled manipulator with artificial sensing that can be reprogrammed to move and position tools to carry out a range of surgical tasks' in Davies' study [66]. The use of robots in surgery could facilitate complex surgical procedures, provide good accuracy and precision, and make some difficult or unfeasible surgeries possible [67]. Robot can help the surgeon in many ways. One way is to hold surgical tools at appropriate positions so that the surgeon can operate the tools much easier [68, 69]. The robot can also be used to position the surgical tools at a target through a predefined path accurately [16, 17]. Another commonly used application is the master-slave robot system. The master (surgeon) can control the slave (robot manipulator) from a console. The master-slave robot system can provide enhanced dexterity and precision. It also make remote surgery possible. Two examples of this are the 'da Vinci' surgical system (Intuitive Surgical Inc.)[70] and the 'Zeus' surgical system (Computer Motion Inc.)[71].

Nowadays, a lot of robotic surgical systems have been researched. Schurr et el [72] introduced a master-slave manipulator system (ARTEMIS) for laparoscopic surgery. The system has two robotic arms which are controlled from a console. The experiments demonstrated that their robotic manipulators are feasible for endoscopic surgery. Dario et al [73] presented a miniature robot which is capable of performing colonoscopy. They demonstrated that their system has many new applications in endoluminal diagnosis, therapy, and surgery with computer assistance. Hu et al [74] integrated haptic feedback in a robot-assisted gastrointestinal surgery. They developed a novel setup which can display the tactile feedback on the haptic interface device. Experiments were done to show the feasibility of their

approach. Similar researches about haptic feedback in robot assisted surgery were reported in [75–77].

There are two commercially available systems need to be mentioned: the daVinci system (Intuitive Surgical Inc.)[70], the Zeus system (Computer Motion Inc.)[71]. Both systems are used clinically for minimally invasive surgery. The da Vinci System consists of a console for the surgeon, and a patient-side cart with four interactive robotic arms (see Figure 2.3). The arms can be used for holding the surgical tools, and can also act as scissors, scalpels and so on. Over the past decade, more than 1.5 million surgeries have been performed using the da Vinci surgical systems. A significant advantage to using the da Vinci system is that the surgeon is able to control the surgery from a seated position separated from the patient. This method of performing surgery distanced from the patient is known as remote surgery and can theoretically be performed from any distance. The

Figure 2.3: Da Vinci robotic surgical system.
(http://intuitivesurgical.com/company/media/images/davinci_s_images.html)

Zeus system was designed for minimally invasive microsurgeries. It consists of a surgeon control console and three robotic arms (see Figure 2.4). Two of its robotic arms mimic the hand movements of surgeon. The surgeon's hand movements are scaled down to allow precise and small cuts. The Zues system can also be used

for remote surgery. Since 2003, Zeus was no longer commercially available with the merger of Computer Motion and Intuitive Surgical.

Figure 2.4: Zeus robotic surgical system.
(http://allaboutroboticsurgery.com/zeusrobot.html)

2.3.2 Remote Center of Motion Mechanism

Percutaneous RFA needle insertion is considered as an effective minimally invasive procedure for liver tumor treatment. Robotic RFA needle insertions with a systematical needle insertion plan could increase insertion accuracy and consistency [17]. To minimize the trauma imposed on the patient body, the RFA needle is expected to go through a Single Insertion Port(SIP) for multiple needle insertions. This can be achieved using a specific manipulation of the needle named Remote Center of Motion (RCM) [12–14]. RCM has been defined as the center of rotation fixed at a point (usually the insertion point in minimally invasive surgery(MIS)) where no mechanical component exists [15].

The RCM can be realized in two ways: software control and mechanical design. The software control method realizes RCM by controlling multiple joints work in coordination. A small number of surgical robots realize RCM in this way. The

DLR MIRO reported by Hagn [78] realized RCM by configuring null-space of redundant kinematics and applying position and force control accordingly. Yang et al [79] demonstrated a model-based design analysis for programmable RCM in MIS. They claimed that their approach can be applied to the analysis of general manipulator. The other way to realize RCM is using specific mechanical designs such as spherical joint, spherical links, concentric multi-link spherical joint [80]. The two popular commercial robot systems for MIS, da Vinci [81] and ZEUS [82], realize RCM in this way. The da Vinci surgical system uses parallel mechanism to realize RCM while ZEUS uses a serial chain. Mitchell et al [83] proposed a "C-arm" RCM mechanism for MIS. They conducted complete kinematic analysis and calculated the optimal link lengths of the manipulator. Similar work could be found in [84] [85] [86] [87]. Kuo et al [88] reported a fully-decoupled parallel manipulator to achieve RCM. By analyzing the singularity and reachable collision-free workspace, they validated the feasibility of this manipulator. Pan et al [89] proposed a novel triangle mechanism which can provide RCM with the optimization link angle calculated. Wu et al [90] used a cable-driven spherical mechanism with a RCM 15 mm above the skin to do robotic positioner for Cryoablation. They claimed that the average targeting error is 2.0 mm, which is validated in needle-placement experiments. Kang et al [91–94] described a RCM mechanism with two semi-circular arches for robot assisted suturing in minimally invasive surgery. Similar mechanism has been exploited for different applications. Yang et al [95] used similar mechanism in a robot manipulator for laparoscopic surgical training. Walsh et al [96, 97] applied this mechanism in a needle guidance and insertion system. Yoon et al [98] applied this mechanism in an automatic lighting system.

Some RFA needle insertion robots has been developed in previous studies. Patriciu et al [16] used a bridge like structure comprising XYZ cartesian stage

and a PAKY-RCM robotic module to execute RFA needle insertions (see Figure 2.5). The PAKY-RCM module was used to achieve the single insertion port and the XYZ cartesian stage was used to adjust the initial robot position to make sure the needle is at the skin entry site. Yang et al [17] used a robot sys-

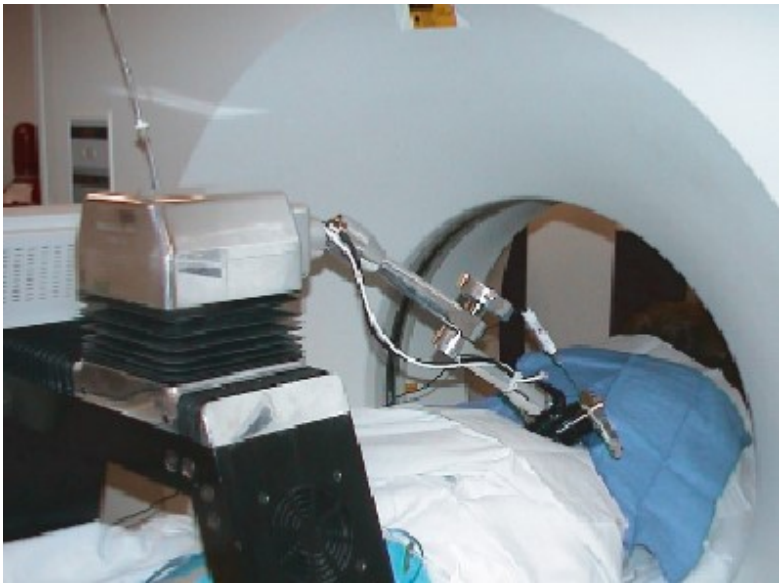

Figure 2.5: The RFA needle insertion robot in patriciu's study [16].

tem comprising a main manipulator and a sub-manipulator (see Figure 2.6). The sub-manipulator consists of four translational stage and a wrist interface with two orthogonal revolution joints. RCM of the RFA needle is achieved by software control method.

From the literature, we observe that existing RFA needle insertion robots did not possess effective mechanical design (such as spherical joint, spherical links) to achieve RCM. A typical system is bulky with complex control algorithms. Current RCM mechanisms that can be used for RFA needle insertion cannot achieve SIP for very large tumor due to their mechanical constraints. Therefore, a RFA needle insertion robot using modified RCM mechanism has to be designed and developed.

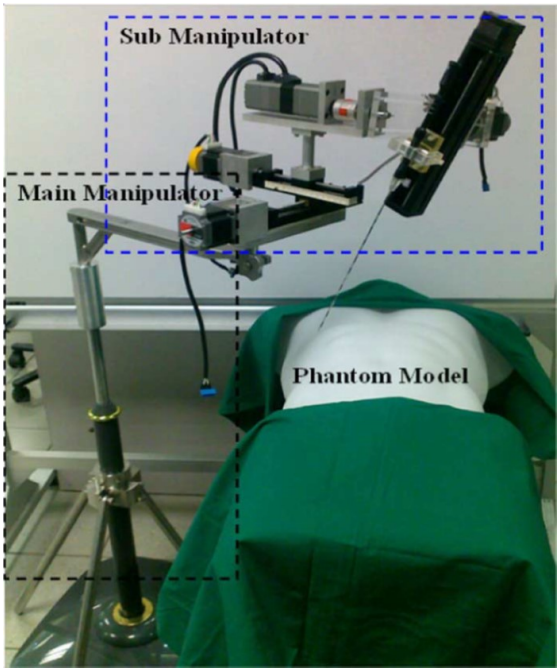

Figure 2.6: The RFA needle insertion robot in Yang's study [17].

2.4 Registration in Surgery

Medical images, such as CT image and magnetic resonance (MR) image, are increasingly used for planning and guiding the treatment. Registration of the pre-operative data and intra-operative data is a key issue in image guided surgery. Image registration is a process that is used to match two or more images of the same scene at different times, by different sensors or from different views [99]. Many effective methods have been proposed for image registration. According to Maintz and Viergever's study [100], medical image registration methods can be divided into two main categories: extrinsic registration methods and intrinsic registration methods. Extrinsic registration methods are based on artificial objects attached to the patient. The attached objects should be well visible in the medical image. Stereotactic frames [101–104] are commonly used for localization and guidance in surgery. Screw-mounted markers[105–108] and skin-glued makers are also [109–111] widely used for registration. The patient is assumed

to be rigid in extrinsic registration methods. These methods are not suitable for non-rigid transformations. Intrinsic registration methods are based on patient image only. Image features and properties are used to map the pre-operative image and intra-operative image. Landmarks-based registration methods [112–114], segmentation-based registration methods [115–117] and voxel property-based registration methods are three commonly used methods for intrinsic registration. Landmark-based registration methods are based on a set of distinct points. Segmentation-based registration methods are based on the segmented structures. Prior data is required in both methods. Voxel property-based registration methods use the image density directly. Many algorithms have been proposed in the literature, including cross-correlation [118–120], Fourier transformation [121, 122], and histogram clustering [123, 124].

Most registrations in the literature are image registration. However, registration in image guided robotic surgery is not limited to the image registration, but also includes registration among surgical tools, patient body and computer image. Some works on image guided robotic surgery are reported in the literature.

Patriciu et al [125] presented a CT image guided robot system for Kidney and Spine Percutaneous Procedures. A simple method for robot registration in CT imaging systems was presented. The registration method involved the laser system on the CT scanner (see figure 2.7). The needle had to be placed in the scanning range of the CT scanner. The application of this registration method is limited since it can only be conducted in the CT room. Similar work can be found in another study [16] of the same author.

Taylor et al [126] presented a CT image guided robot system for orthopedic surgery. The author claimed that the registration between CT planning data and reality was accomplished by using landmark pins. The author also indicates that the registration can be achieved by real-time tracking of makers placed on

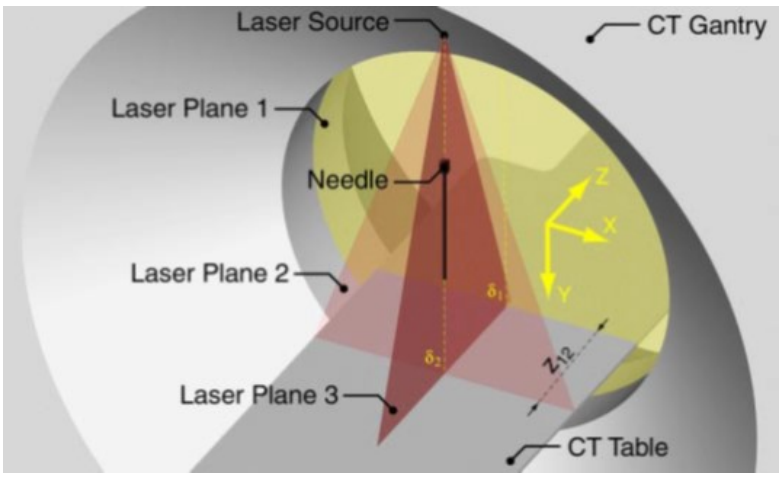

Figure 2.7: Laser registration method for robot registration [125].

the patient. However, The detailed registration method was not presented in this paper. Anthony et al [127] also reported a robot assisted orthopedic surgery under CT image guidance. To track the bone structures and tools, tracking devices were attached to the targeted bone and tools. This method causes large invasiveness to the patient and requires a lot of sensors.

Yang et al [17] developed a robotic system for RFA of liver tumor under the guidance of pre-operative CT images. To register the pre-operative data with reality, they used a noninvasive approach based on fiducial skin marker. A rigid transformation approach was implemented using an optical triangulation system. They tested the system on a static abdominal phantom and demonstrated the feasibility of the system. Since the optical triangulation system will introduce registration error, an error compensation method is therefore required to guarantee the accuracy of registration.

The existing registration methods in image guided robotic surgery still have a lot of limitations. Effective registration methods, especially the registration between patient and robot, in image guided robotic surgery need to be further researched.

2.5 Summary

In this chapter, we review three key issues on computer-aided and robot-assisted RFA. In RFA simulation and planning, the thermal-electrical properties of soft tissue are subjected to inherent variations due to anatomic microstructural differences and patient individual differences. Hence, it is important to consider the variations of the thermal-electrical properties in RFA simulation. Probabilistic FE simulation and planning for RFA needs to be further researched.

Since we focus on RFA of large liver tumor, multiple RFAs are required to entirely cover the tumor. To achieve a single insertion port during multiple RFAs, a robot which can realize RCM should also be developed.

Registration of the pre-operative data and intra-operative data is a key issue in image guided surgery. However, most registrations in the literature focus on image registration. In robotic surgery, registration between patient and robot is very important to guarantee the accuracy of robot execution. There is a lack of efficient and generic registration method between patient and robot. Effective registration methods, especially the registration between patient and robot, in image guided robotic surgery need to be further researched.

Chapter 3

RFA Simulation and Planning

A challenging problem of radiofrequency ablation(RFA) in liver surgery is to accurately estimate the shape and size of RFA lesion whose formation depends on intrinsic variations of the thermal-electrical properties of soft tissue. Large tumor, which can be as long as 10 cm or more, has further complicated the problem. In this chapter, a probabilistic bio-heating finite element (FE) model is proposed and developed to predict the RFA lesion. Uncertainties of RFA lesion are caused by the probabilistic nature of five thermal-electrical liver properties: thermal conductivity, liver tissue density, specific heat, blood perfusion rate and electrical conductivity. Confidence levels of shape and size of lesion are generated by the FE model incorporated with mean-value first-order second-moment (MVFOSM) method. Based on the probabilistic FE method, a workflow of RFA planning is introduced to enable clinicians to preoperatively view the predicted RFA lesion in three-dimension (3D) within a hepatic environment. Accurate planning of the RFA needle placements can then be achieved based on the interactive simulation and confidence level selection.

3.1 Overview of the Probabilistic RFA Simulation and Planning Method

In general, RFA is considered as a safe, well-tolerated and effective treatment only for small liver tumors which are less than 6.0 cm in diameter[128]. Reliable RFA simulation and planning are important for large liver tumor treatment. The objective of RFA simulation and planning is to assist clinicians to verify that the lesions produced by multiple RFAs can fully cover a large tumor with minimal damages to the surrounding healthy tissues. We proposed a probabilistic RFA simulation and planning method to predict the RFA lesions for treatment planning. This probabilistic method may improve the safety and effectiveness of RFA treatment for large tumor.

In our RFA planning procedure, the clinician should specify the positions of RFA needle. The probabilistic bio-heat FE simulation is then applied to predict the RFA lesions according to the specified RFA needle positions. Different shapes and sizes of RFA lesions, along with their probabilities, can be displayed. The results can provide clinicians an overview of ablation effect for potential risk evaluation, and help them to decide which specific RFA plan to adopt for the patient.

Figure 3.1 shows the workflow of probabilistic bio-heat FE simulation-based RFA planning. Geometric information including critical anatomic structures for FE model construction is acquired from preoperative medical images. After the position and geometric profile of tumor are identified from the medical images, the safety margin of tumor will be specified. A local coordination system is established at the center of the targeted tumor. This coordination system defines the RFA planning space. Tissue thermal-electrical properties, initial and boundary conditions, such as temperatures of the liver, are assigned to construct the bio-heat FE model. Multiple RFA needle placements are set within the bio-heat FE model.

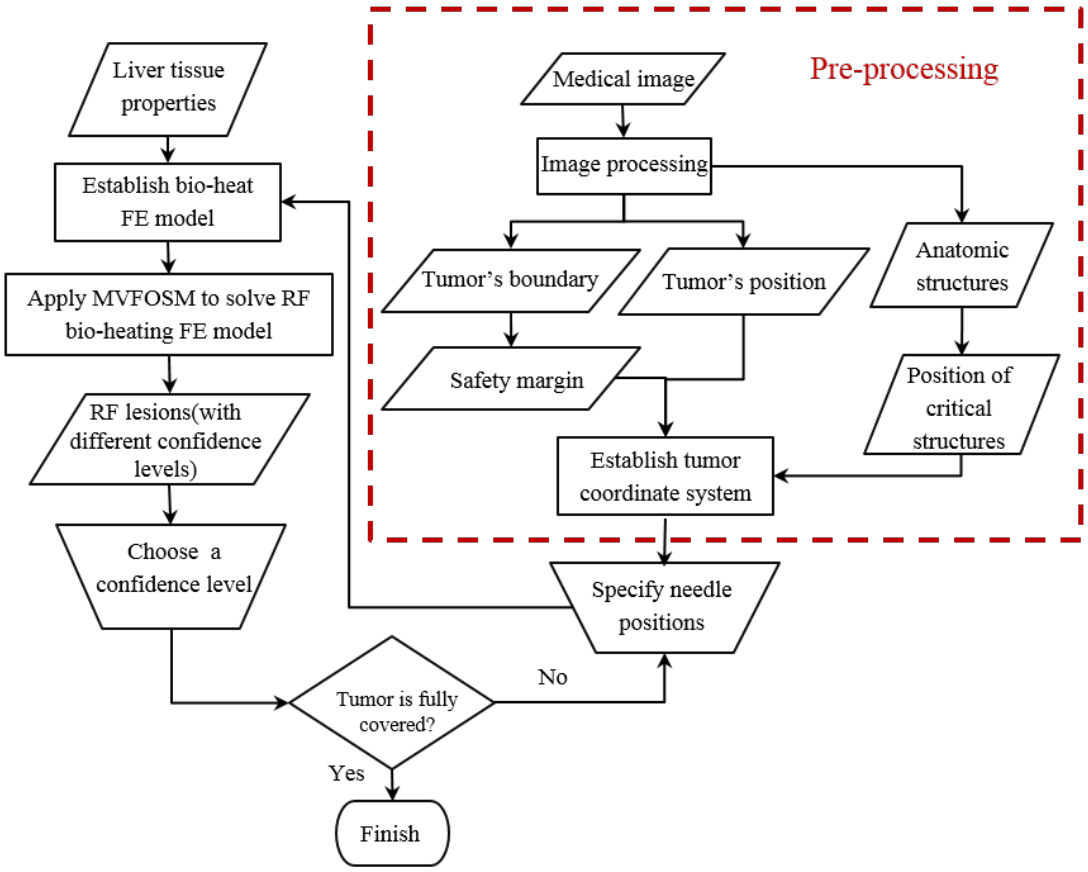

Figure 3.1: Probabilistic bio-heat FE simulation based RFA planning.

The probabilistic distribution of temperature can then be calculated using the MV-FOSM method. The probabilistic simulation allows clinicians to choose different confidence levels and generates the corresponding 3D views of the RFA lesions. Clinicians will choose a specific confidence level according to patient-specific condition and their own experiences. They can try different needle placements until a satisfactory result has been achieved. The following sections will explain how the probabilistic FE RFA model is built, demonstrate the computational results and experimental results, and present the multiple RFA planning results.

3.2 Probabilistic Bio-heat Model for RFA

According to Arkin's investigation on heat transfer modeling of blood perfused tissue, Pennes' model was demonstrated to be the best approach to simulate RFA [129]. In this study, we simulated RFA of liver tissue using Pennes' bio-heat equation which can be written as

$$\rho c \frac{\partial T}{\partial t} = \nabla \cdot k \nabla T + J \cdot E - \rho_{bl} c_{bl} \omega_{bl} (T - T_{bl}), \tag{3.1}$$

where ρ is the density, T is the temperature, k is the thermal conductivity, J is the current density, E is the electric field, ρ_{bl} is the blood density, c_{bl} is the blood specific heat, ω_{bl} is the blood perfusion rate and T_{bl} is the blood temperature.

Since the objective of our simulation is to predict the lesion after RFA, Arrhenius equation is used to model the thermal damage of the tissue [25]. The tissue injury degree Ω can be calculated by

$$\Omega = ln(\frac{c(0)}{c(t)}) = A \int_0^t e^{-\Delta E/[RT]} dt, \tag{3.2}$$

where $c(t)$ is the concentration of living cells, $c(0)$ is the initial concentration of living cells, R is the universal gas constant ($8.314 J \cdot mol^{-1} \cdot K^{-1}$), A is a 'frequency' factor for the kinetic expression, and ΔE is the activation energy for the irreversible damage reaction. For liver tissue, $A = 7.39 \times 10^{39} s^{-1}$ and $\Delta E = 2.577 \times 10^5 J \cdot mol^{-1}$ [25]. In this study, the cell is considered dead when $\Omega > 1$ and it is reported that tissue coagulation first occurs when $\Omega = 1$ [130]. The blood perfusion rate is modeled as a function of tissue injury degree Ω according to the study by Schutt et al.[131]. The blood perfusion can be modelled as

$$DS = 1 - e^{-\Omega}, \tag{3.3}$$

and

$$\omega(t) = \omega_0(1 - DS), \tag{3.4}$$

where DS is degree of vascular stasis, $\omega(t)$ represents the time dependent perfusion, and ω_0 is the base line perfusion.

Probabilistic uncertainty analysis is used to quantify the effect of input random variables on system outputs [132]. Consider the performance function

$$y = g(x), \tag{3.5}$$

where x is a random vector $X = [x_1, x_2...x_n]$ representing uncertain parameters. As x is randomly distributed, y is also randomly distributed. The cumulative distribution function (CDF) of y can be calculated by a multi-dimensional integral

$$F(y) = P(Y \leq y) = \int_{(g(x) \leq y)} f_X(x), \tag{3.6}$$

where $f_X(x)$ is the joint probability density function of random vector X.

In probabilistic uncertainty analysis, it is difficult to obtain an analytical solution to the integration in Equation 3.6 due to both its nonlinear integration boundary and high dimensionality. Various probabilistic analysis techniques have been proposed to obtain the solution to such problem in the last decades. These techniques can be categorized into three classes: (1) sampling based methods, (2) moment matching methods, and (3) most probable point (MPP) based methods [132]. The moment matching methods [60, 61] which only consider the first few moments of the variables distribution are often employed to simplify the problem. One commonly used method is the MVFOSM method, which uses a first order Taylor expansion at the mean values of the input variables and the first and second moments of the input variables [133]. MVFOSM method is a prob-

abilistic method to determine the stochastic moments of a function with random input variables. Assuming variables in x follow normal distribution, temperature in Equation (3.5) can be calculated by

$$y \cong g(\mu_x) + \sum_{i=1}^{n} \frac{\partial g(\mu_x)}{\partial x_i}(x_i - \mu_{x_i}), \tag{3.7}$$

where μ_x is the mean vector of x. y, estimated to be a linear combination of variables in x, is normally distributed. The mean and standard deviation of y can be calculated by

$$\mu_y \cong g(\mu_x) \tag{3.8}$$

and

$$\sigma_y \cong \sqrt{\sum_{i=1}^{n} (\frac{\partial g(\mu_x)}{\partial x_i}\sigma_{x_i})^2}, \tag{3.9}$$

where σ_{x_i} is the standard deviation of the ith element of X.

Liver tissue RFA simulation can also be considered as a probabilistic analysis problem, by which the distribution of tissue temperature T and tissue injury degree Ω can be approximated by the probabilistic approach. In this study, we adopted the MVFOSM method for RFA simulation. Based on Equation 3.1 and Equation 3.2, tissue temperature T and tissue injury degree Ω can be rewritten as

$$T = g_{FE}(U), \tag{3.10}$$

and

$$\Omega = f_{FE}(U), \tag{3.11}$$

where $U = [\rho, k, c, \omega_{bl}, \gamma]$ is the vector of liver tissue thermal-electrical properties.

Assuming variables in U follow normal distribution, the tissue temperature T and tissue injury degree Ω will also be normally distributed. Applying the MV-

FOSM method as shown in Equation 3.8 and Equation 3.9, mean and standard deviation of T and Ω can be approximated by

$$\mu_T \cong g_{FE}(\mu_U), \tag{3.12}$$

$$\sigma_T \cong \sqrt{\sum_{i=1}^{n}(\frac{\partial g_{FE}(\mu_U)}{\partial U_i}\sigma_{U_i})^2}, \tag{3.13}$$

$$\mu_\Omega \cong f_{FE}(\mu_U), \tag{3.14}$$

$$\sigma_\Omega \cong \sqrt{\sum_{i=1}^{n}(\frac{\partial f_{FE}(\mu_U)}{\partial U_i}\sigma_{U_i})^2}, \tag{3.15}$$

whereμ_T, σ_T, μ_Ω, σ_Ω are the mean and standard deviation of T, mean and standard deviation of Ω respectively. $\mu_U = [\mu_\rho, \mu_k, \mu_c, \mu_\omega, \mu_\gamma]$ is the mean value of U, n is the length of U and $\frac{\partial g_{FE}(\mu_U)}{\partial U_i}$ is the partial derivative of g_{FE} at the mean vector μ_U with respect to the ith element of U, σ_{U_i} is the standard deviation of ith parameter of vector U, $\frac{\partial f_{FE}(\mu_U)}{\partial U_i}$ is the partial derivative of f_{FE} at the mean vector μ_U with respect to the ith element of U.

3.3 FE RFA Simulation

The probabilistic bio-heat model described above was used to implement the FE simulation of RFA. The spatial distribution of temperature T and tissue injury degree Ω can be obtained from the probabilistic FE simulation. COMSOL Multiphysics software (COMSOL, Burlington, MA, USA) was used to conduct the simulation on a PC with Intel Core i5 CPU and 8GB memory. The effectiveness of using the MVFOSM method for FE RFA simulation was validated by Monte Carlo simulations. Experimental RFA lesions were also compared with the computational RFA lesions to prove that the experimental lesions follow the predicted

probability distribution.

3.3.1 FE Model Construction

In the simulation study, COMSOL Multiphysics software was used to implement our probabilistic FE RFA model. Equation 3.1 and Equation 3.2 were used as the governing equations for the FE model. The FE model was then implemented by the following steps. Firstly, the geometry of the FE model was built by constructing the 3D model of the RFA probe and the liver. Since human liver is a very complex and heterogeneous organ, it is very difficult to reproduce the exact liver structure accurately in computer simulation. RFA simulations in the literature typically start with a simplification of the real physical situation. Cube [22, 24] and cylinder [23, 25, 26] are two commonly used geometry to model biological tissue in 3D FE analysis of RFA. Since our RFA experiment was conducted on pig liver to validate our simulation, we made our tissue size similar to that of the real pig liver size. The maximum thickness of pig liver is about $60mm$ and both the length and width are about $160mm$. Therefore, a cube of $160 \times 160 \times 60$ mm (Figure3.2(b)) was used to represent the target liver tissue and a model of RITA Starburst RFA probe (Figure3.2(a)) was modeled as the RFA needle. The ther-

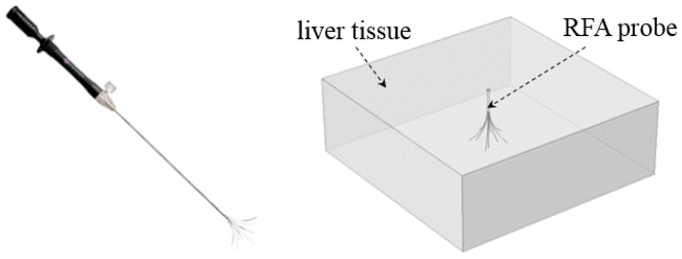

(a) (b)

Figure 3.2: Geometry of the FE model. (a)RITA starburst RFA probe. (b)3D model of the RFA probe and the liver.

mal and electrical properties of liver tissue were then assigned to the liver model.

Previous studies [6–8, 10, 11, 134] have indicated that the thermal and electrical properties of liver tissue are random values that can follow certain probability distribution. Since normal distribution model can fit the data in previous literatures well, we assumed that the thermal and electrical properties of liver tissue are normally distributed. The mean value and standard deviation (STD) of each property were calculated based on the data in literatures (as shown in Table 3.1). The initial and boundary temperatures were set to be 37 °C in the simulation

Table 3.1: Liver tissue thermal and electrical properties [6–8, 10, 11, 134].

Properties	Temperature Dependency	Parameters
$\rho(Kg \cdot m^{-3})$	$\rho = \rho_0$	ρ_0 (mean:1064 STD:16) [7]
$k(W \cdot m^{-1} \cdot K^{-1})$	$k = k_0 + 0.00116T$	k_0(mean:0.4692 STD:0.13) [10, 134]
$c(J \cdot Kg^{-1} \cdot K^{-1})$	$c = c_0$, if $T < 63.5$ $c = c_0 + 28.9(T - 63.5)$,if $T \geq 63.5$	c_0(mean:3399.9 STD:522.34) [8]
$\omega(s^{-1})$	$\omega = \omega_0(1 - DS)$ (as in Equation 3.4)	ω_0(mean:0.007 STD:0.0027) [6]
$\gamma(S \cdot m^{-1})$	$\gamma = \gamma_0 + 0.00889(T - 35)$, if $T < 80$ $\gamma = \gamma_0 + 0.4 - 0.01(T - 80)$, if $T \geq 80$	γ_0(mean:0.4 STD:0.03) [11]

model. Next step is meshing the model. A convergence analysis was conducted to obtain the optimum mesh for the model. We defined the optimum mesh by decreasing the mesh element size until differences between maximum temperatures at 300s in consecutive simulations were less than 0.5%. In our simulation, we controlled the maximum element size for each mesh setting. The maximum element size was varied from 15mm to 1mm, and we observed that when the maximum element size is smaller than 12mm, differences between maximum temperatures at 300s in consecutive simulations were less than 0.5%. Therefore, 12mm was used in the maximum element size setting. The FE model was built with 221525 domain elements, 12608 boundary elements, and 3084 edge elements. To make the simulation realistic and to be validated by experiment, temperature-control protocol was applied in the simulation as in the real RFA system. In the radiofrequency

generator we used for experimentation(RITA 1500X), a target temperature should be set before RFA procedure, and the device can measure the temperature of the RFA needle tips. RFA voltage of the radiofrequency generator is controlled by proportional-integral (PI) strategy so that the tissue temperature would increase first and then keep stable at the target temperature. The RFA voltage in our simulation was controlled by

$$V = KP * (T_{set} - T_{tip}) + KI * \int (T_{set} - T_{tip})dt, \tag{3.16}$$

where V is the applied RFA voltage, T_{set} is the predefined RFA target temperature, which is $105°C$ in this study, T_{tip} is the average temperature of the RFA needle tips, KP and KI are the proportional coefficient and integral coefficient respectively. KP and KI were adjusted so that the temperature rising time in the simulation is the same as the rising time in the experiment. The values for KP and KI are 0.5 and 0.02 respectively. The RFA power was applied for 300 seconds in all simulations.

3.3.2 Simulation Results

The spatial distribution of temperature T and tissue injury degree Ω can be obtained from the FE model. Both T and Ω follow normal distribution. In this study, RFA lesion was defined as region where $\Omega > 1$. Figure 3.3(a) shows the shape of a 3D RFA lesion and the highlighted plane that we analyzed. The temperature distribution on the analyzed plane is shown in Figure 3.3(b), and Figure 3.3(c) shows the shape of the RFA lesion on the analyzed plane.

As described in Section 3.2, the RFA lesions we obtained should be normally

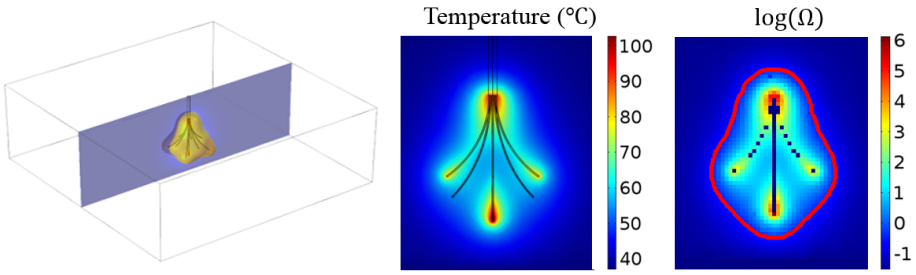

(a) (b) (c)

Figure 3.3: Simulation results. (a)Shape of 3D RFA lesion and the plane we examined. (b)Temperature distribution on the examined plane. (c)Tissue injury degree in log scale, the red line represents the damage contour where $\Omega = 1$ (i.e. $log(\Omega) = 0$).

distributed. The confidence level of a RFA lesion was defined as

$$p = 1 - p_{(\Omega \leq 1)}, \tag{3.17}$$

where $p_{(\Omega \leq 1)}$ represents probability of existing living tumor cells within the above defined RFA lesion (RFA lesion was defined as region where $\Omega > 1$).

Figure 3.4 shows the lesion sizes of different confidence levels. The possibility of living cells within the negative 3 sigma lesion damage contour is 0.13%, which means the probability of completely destroying the whole tumor within the negative 3 sigma lesion damage contour is 99.87%. The probabilities of completely destroying the tumor within the mean and positive 3 sigma lesion damage contours are 50% and 0.13% respectively.

To identify which parameter has the greatest impact on RFA simulation, numerical values of $\partial T / \partial_{U_i}$ were calculated. The partial derivatives values at any interested point in the FE model can be obtained. A point 15mm away from the bottom tip of the RFA probe in the above mentioned plane was selected to illustrate the result. The partial derivatives of the selected point at different times were shown in Table 3.2. We can observe that the values of $\partial T / \partial_{\omega_{bl}}$ are the largest, which indicates that blood perfusion rate is the most dominant parameter

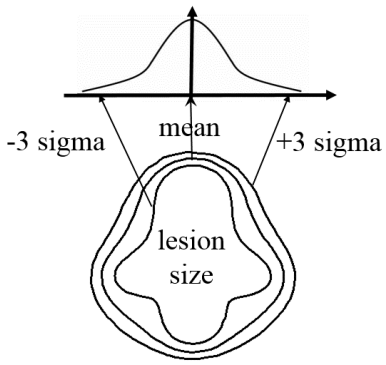

Figure 3.4: lesion sizes with confidence level of 99.87% (-3sigma), 50% (mean) and 0.13% (+3sigma).

determining the temperature during the RFA heating.

Table 3.2: Numerical values of $\partial T / \partial U_i$ at different times.

Time(s)	$\partial T / \partial c$	$\partial T / \partial \gamma$	$\partial T / \partial k$	$\partial T / \partial \rho$	$\partial T / \partial \omega_{bl}$
100	-8.6329e-04	6.7234	1.1728	-0.0027	-177.2743
200	-9.1350e-04	10.7023	1.6738	-0.0029	-531.5399
300	-6.2980e-04	13.0513	2.1997	-0.0020	-749.8232

3.3.3 Monte Carlo Validation of the MVFOSM method

Monte Carlo method is commonly used for computer simulation in physical and mathematical systems when it is infeasible to compute an exact solution with a deterministic approach [135][136][137]. Monte Carlo method relies on repeated random sampling. A large number of simulations are required to obtain results with high confidence. Despite its computationally expensiveness, it is an effective approach to verify newly proposed probabilistic analysis methods.

In order to validate the RFA simulation results calculated by MVFOSM method, RFA FE analysis were performed for 1000 times. For every simulation, properties of liver tissue were randomly generated according to their normal distributions shown in Table 3.1. Temperature distributions calculated in Section 3.3.2 are compared with Monte Carlo simulation results. Figure 3.5 shows CDFs of the

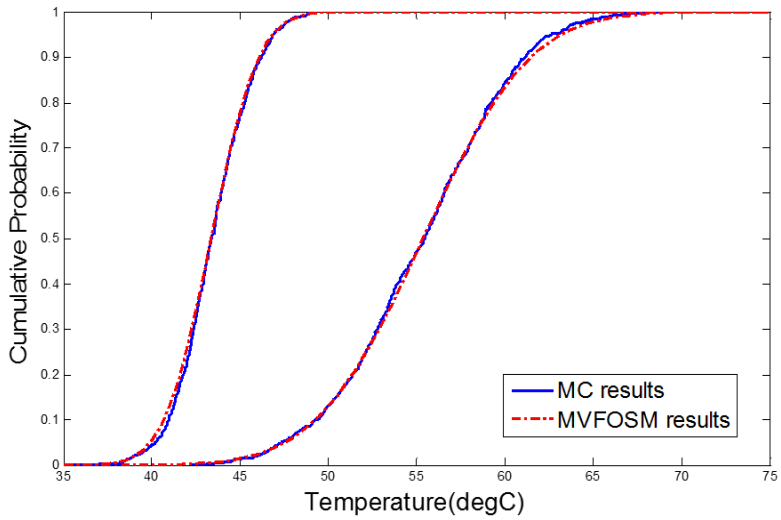

Figure 3.5: CDFs of temperature at two different points; the right two curves are temperature CDFs of the point 5mm away from the bottom tip of the RFA probe, the left two curves are temperature CDFs of the point 15mm away from the bottom tip of the RFA probe.

temperature of two points located 5mm and 15mm away from the RFA probe center. CDFs calculated by the MVFOSM method correspond well with those of the Monte Carlo simulation results. Small discrepancies can result from the use of first order Taylor linearization to approximate the nonlinear process of FE analysis.

3.3.4 Comparison between simulated RFA lesion and experimental RFA lesion

To demonstrate that the computational RFA lesions are reliable, experiments were conducted to compare the simulation results with experimental results. Figure 3.6 shows the setup for the RFA experiment. A RITA 1500X radiofrequency generator and a RITA Starburst RFA probe were used to conduct experiments on a recently harvested pig liver. In this experiment, the target temperature was set to be $105°C$ as in the simulation and the RFA power was delivered for 300s in each experiment. 20 ablations were conducted and the lesions were split from

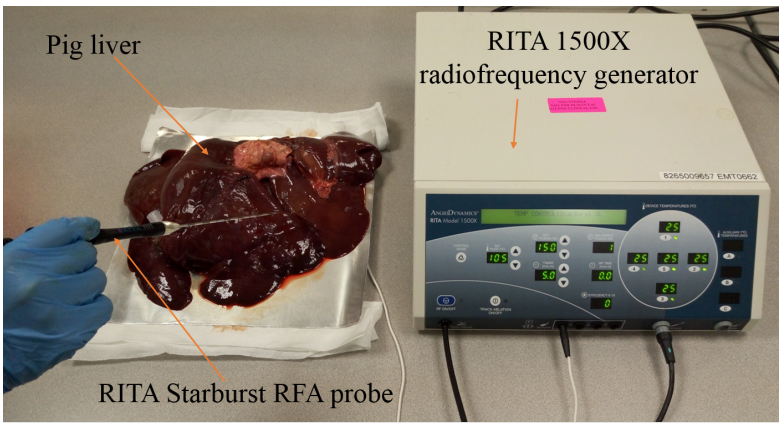

Figure 3.6: RFA device for experiment.

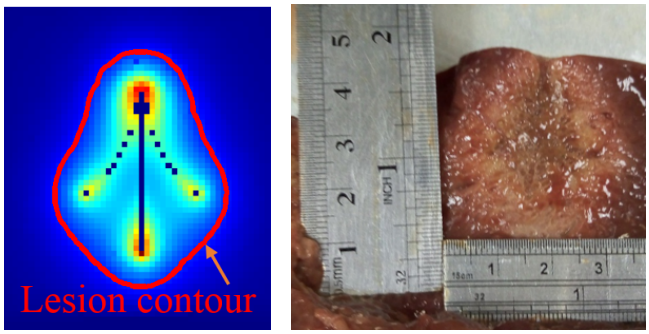

(a) (b)

Figure 3.7: Comparison between simulated RFA lesion and experimental RFA lesion. (a)Computational lesion. (b)Experimental lesion.

the middle to reveal their shapes. Figure 3.7 shows a computational RFA lesion and an experimental RFA lesion. We can see that the shapes of these two lesions are similar. The central white zone excluding the pink zone in Figure 3.7(b) was defined as the thermal lesion. To evaluate the experimental lesions, GetData Graph Digitizer (an open source digitizing software) was used to grab the lesion contour data from experimental pictures. We drew the lesion contours manually in the software and exported the data to Matlab for further evaluation of the experimental lesions. To compare the experimental and computational lesions quantitatively, the area, depth and maximal width of experimental and computational lesions are measured. The mean value and standard deviation of each

property (area, depth and maximal width) are calculated. Standard deviation is defined as the square root of the average of the squared deviations of the values from their average value. The mean and standard deviations of each property are shown in Table 3.3. The mean area of the 20 experimental lesions is $816.7mm^2$ and this is close to the computational mean area, which is $822.4mm^2$. The standard deviations of the experimental area and computational area are $115.8mm^2$ and $87.1mm^2$ respectively. CDFs of the computational area and experimental area correspond well as shown in Figure 3.8. From Table 3.3, we can observe that the mean values of area, depth and maximal width of experimental lesions are a little smaller than those of computational lesions while the standard deviations of experimental lesions are bigger than computational lesions. The small discrepancies between computational and experimental lesions may result from the small differences between human liver and pig liver. The error in measuring the experimental lesions may also lead to the discrepancies between computational and experimental lesions.

Table 3.3: Comparison between experimental and computational lesions

Categories	Experimental results	Computational Results
Area (mm^2)	mean:816.7 STD:115.8	mean:822.4 STD:87.1
Depth (mm)	mean:37.1 STD:2.8	mean:41.2 STD:2.1
Maximal width (mm)	mean:26.6 STD:3.8	mean:29.5 STD:2.7

Although there are only 20 sets of experimental data to validate the probabilistic method, we have observed that the experimental lesions can be approximated by normal distribution in Figure 3.8. This is consistent with our prediction. Since probability distribution presents in real RFA lesions, it is not feasible to use simulations that give constant outputs for RFA planning. By using our simulation model, different sizes of RFA lesions along with their probabilities can be obtained.

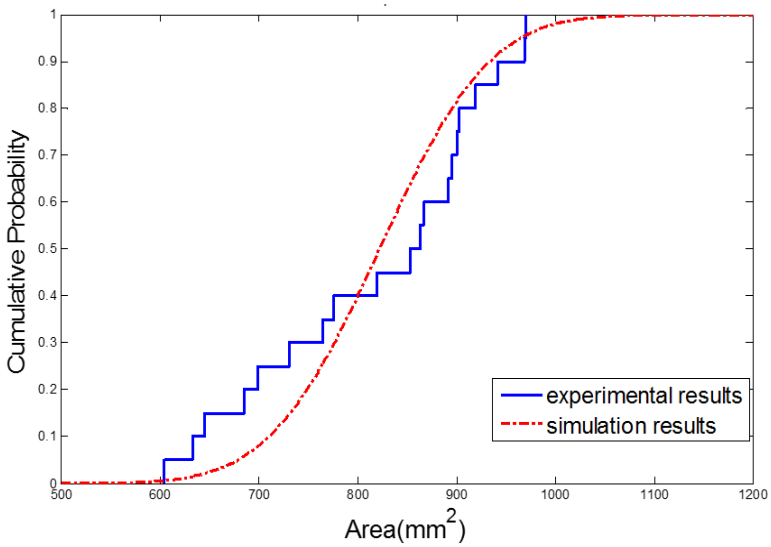

Figure 3.8: Cumulative Distribution Functions (CDFs) of the simulated RFA lesion area and the experimental RFA lesion area. The cumulative distribution function of a random variable X, evaluated at x, is the probability that X will take a value less than or equal to x.

This can improve the reliability of RFA planning. Since our probabilistic RFA simulation is able to produce the probability distribution of RFA lesions as that of real experiment, it is therefore useful and effective.

3.4 Probabilistic RFA Planning Results

For large tumor treatment, multiple sequential RFAs are required to fully cover the tumor and thus a planning strategy is needed. In our RFA planning for large tumor, we do not provide a mathematical model to generate RFA needle placements to cover a large tumor. Instead, we let the clinician to define the needle placements and showed the computational lesions of multiple RFAs. The clinician can try different needle placements until a satisfactory result has been achieved. Based on our experience, this strategy is more robust for RFA treatment planning. Since the burned tissue has an effect on subsequent ablation, the properties of the burned tissue should be modeled in the simulation of multiple sequential RFAs. The blood perfusion in the burned tissue was updated during the simulation be-

cause it has the greatest impact on RFA simulation result (as shown in Table 3.2). For multiple sequential RFAs simulation, we assumed that the blood perfusion of the burned tissue is zero because blood perfusion ceases after coagulation occurs. For other properties of the burned tissue, we assumed that they remain the same as that of the normal tissue since there are very few literatures studying the properties of burned tissue.

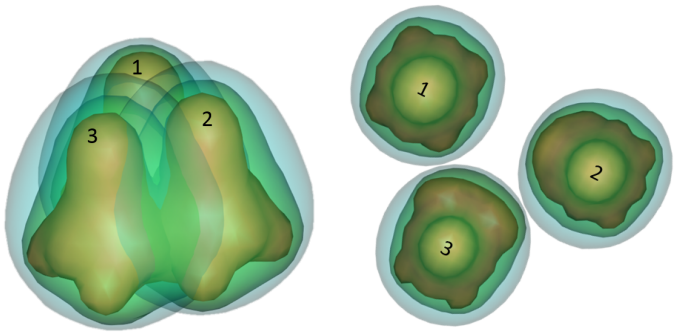

(a) (b)

Figure 3.9: Lesions of three sequential RFAs.The numbers indicate the ablation sequence. The shapes in maroon, green and cyan represent lesions with confidence level of 99.87% (-3sigma), 50% (mean) and 0.13% (+3sigma) respectively.(a) Lesion volumes of three sequential RFAs. (b) Lesion shapes of every ablation.

Considering that the properties change in burned tissue, the shape of each RFA lesion should be different. Figure 3.9 shows the computational lesions of three sequential RFAs. Lesions in 3D with different probabilities can be obtained from our probabilistic simulation method. The numbers in Figure 3.9(a) illustrate the sequence of needle placement. The shape of each RFA lesion is shown in Figure 3.9(b). We can clearly observe that each lesion shape is different and the lesion shapes bulge towards the burned region. The reason is that blood perfusion can take away the heat during RFA heating, whereas blood perfusion has ceased in burned tissue. Therefore, more heat flows from the currently ablating tissue to the already burned tissue.

Figure 3.10 shows the lesions of three sequential RFAs in human liver near a big

blood vessel. The results can be displayed in 3D within a hepatic environment to clinicians as shown in Figure 3.10(a). The heat sink effect of the big blood vessel was considered in the simulation. We assumed that the surface temperature of the blood vessel is always 37 °C. It can be observed that there are hollows on the lesion shapes near the blood vessel as shown in Figure 3.10(b). Using our probabilistic simulation method, the RFA lesions in different sizes with different confidence levels can also be displayed to clinicians as shown in Figure 3.10(c). Based on our simulation, clinicians can try different RFA needle placements for multiple RFAs. By choosing different confidence levels, clinicians are able to identify the probability of fully covering the tumor by RFA lesions.

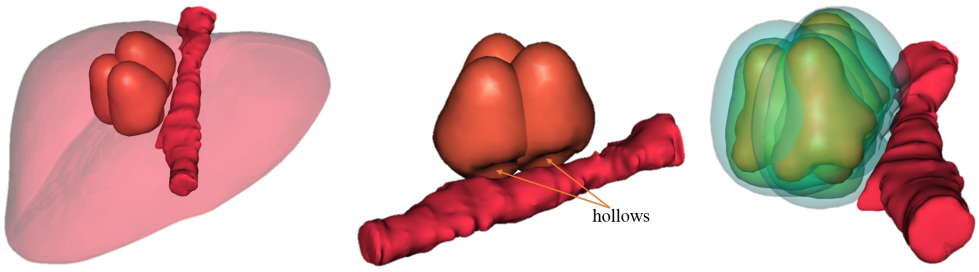

(a) (b) (c)

Figure 3.10: Lesions of three sequential RFAs in human liver near a big blood vessel. (a) 3D RFA lesion volumes inside the liver. (b) Effect of blood vessel on RFA lesions. (c) RFA lesions in different sizes with different confidence levels.

3.5 Summary

This chapter describes a generalized probabilistic bio-heating FE model for RFA simulation. It can be useful to assist clinicians to make a reliable RFA plan by providing them 3D views of predicted RFA lesions with different confidence levels. This simulation method incorporates probabilistic uncertainty analysis and bio-heating FE model which integrates inherent thermal-electrical variations of target tissue. In this FE model, we focused only on electrical and thermal prop-

erties of the liver and mechanical properties are not considered. The probabilistic bio-heating FE model-based planning method enables the clinician to specify a confidence level for practical patient-specific cases. To our best knowledge, this is the first study on a preoperative RFA estimation with probabilistic bio-heating FE modeling method.

The RFA simulation and planning presented in this chapter are both based on the probabilistic method. Unlike typical materials, the structure of biological tissue is much more complicated and the anatomic micro-structure differences always exist among different individuals and different parts of the same individual. Therefore, it is not feasible to model the thermal-electrical properties of biological tissue as a constant or a temperature dependent function. It is more reasonable to model them using normal distribution, as shown in many literatures [6–8, 10, 11, 134]. We have proved that the RFA temperature fields and RFA lesions follow normal distribution. The advantage of providing clinicians results with probabilistic distribution is that it allows the clinicians to know how much confidence they have to fully cover the tumor.

In our RFA planning for large tumor, we did not set the RFA needle placements automatically by computer. Instead, we let the clinician to define the needle placements and showed the computational lesions of multiple RFAs with different confidence levels. The clinician can try different needle placements until a satisfactory result has been achieved. Based on our experience, this strategy is more robust for RFA treatment planning. One innovation in our planning is that we take into consideration the change of tissue properties after each ablation. In this study, only the blood perfusion in the burned tissue was updated since it has the greatest impact on RFA simulation result and there are very few literatures studying other properties of the burned tissue. The results of sequential ablations shows that the shapes and sizes of sequential lesions are different.

A limitation of our RFA simulation and planning system is that the properties of liver tumor were regarded as the same as those of healthy liver tissue. Liver tumors is caused by the uncontrolled growth of cells in the liver. The thermal-electrical properties of liver tumor is likely to be different from that of healthy liver tissue. For example, the cells in the tumor are denser and there are more blood vessels around the tumor to provide nutrition to the tumor. We have been collaborating with clinicians in our local hospital. We will try to acquire real tumor tissue and measure its material properties in the future. We did not come across similar studies in the literature. Another limitation is that our RFA planning is a computationally intensive process. It takes about one and half hour to run the simulation on a PC with Intel Core i5 CPU and 8GB memory. Hence, the RFA planning may not be suitable for certain clinical situation. For example, it will result in longer operation duration if the clinician intend to investigate new needle placements during the operation. Currently, our planning can only help the clinician in the preoperative stage. Nonetheless, our idea of applying probabilistic method and considering change of properties during multiple sequential ablations is useful for RFA simulation and planning.

Chapter 4

RFA Needle Insertion Robot

Multiple needle insertions and ablations are required in percutaneous Radiofrequency Ablation (RFA) for large liver tumor treatment. Current RFA procedure for large liver tumor treatment is challenged by inaccurate needle placement, inconsistent execution of needle insertion, and large invasiveness created by multiple needle insertions. In this chapter, we developed a Remote Center of Motion (RCM) robot mechanism for multiple RFA needle insertions covering the entire tumor volume through a Single Insertion Port (SIP). A spherical mechanism comprising two semi-circular arches were used to realize the RCM. Two motorized linear slides were incorporated into the system to achieve SIP. A novel analytical method for modeling this RCM mechanism was proposed. This method can overcome the limitation of previous method in literature. Simulation was conducted with real patient data including liver and tumor model to show the correctness of our analytical method and to validate feasibility of the mechanism. Integrative speed and position control strategy was implemented to allow the robot to move smoothly and precisely. Experiments were conducted to test the accuracy and feasibility of the RFA needle insertion robot. The results demonstrate that our robot system is capable of accurately executing multiple RFAs of large liver tumor

through SIP.

4.1 Needle Insertion Robot Design

In order to enable the multiple RFA needle insertions to pass through SIP in large tumor treatment, a RCM mechanism for RFA needle insertion is designed. The movement of RFA needle insertion can be divided into two parts (Figure 4.1). Firstly, to adjust the needle to the desired direction so that it can reach the target point through the insertion port. Secondly, to lead the needle in the adjusted direction to the target point. The proposed RCM mechanism is accordingly divided into two parts: a rotational subassembly which is able to adjust the direction of the needle and a translational subassembly that can realize the translational motion of the RFA needle.

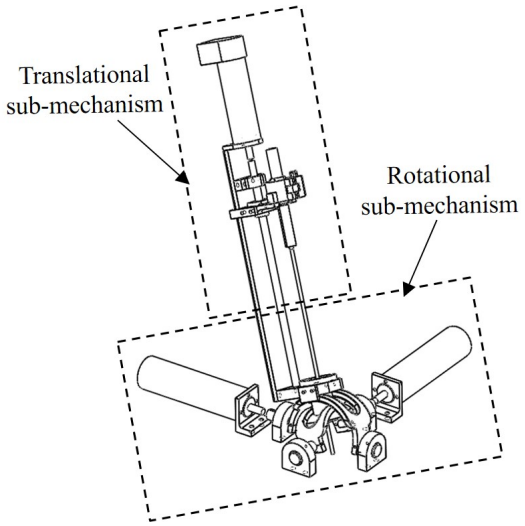

Figure 4.1: Overview of the RCM mechanism for robotic RFA needle insertion.

In the rotational subassembly (Figure 4.2), two semi-circular arches are crosswise constructed to guide the RFA needle direction. The two arches are mounted in a perpendicular configuration. Each semi-circular arch has a slot, in which a pipe slider is placed inside. The pipe slider is restricted to slide within the two

arches at the same time. The two semi-circular arches are driven by two direcct current (DC) motors respectively. The translational subassembly (Figure 4.3) realizes the translational motion of the RFA needle through a ball screw system. The needle is attached to a holding mechanism via a needle clamp. This holding mechanism is attached to the ball screw nut which provide translational motion when the ball screw shaft is driven by the DC motor.

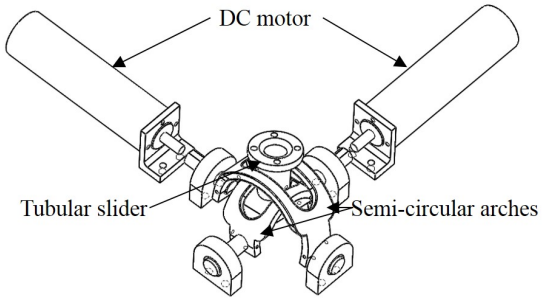

Figure 4.2: Rotational subassembly of the RCM mechanism.

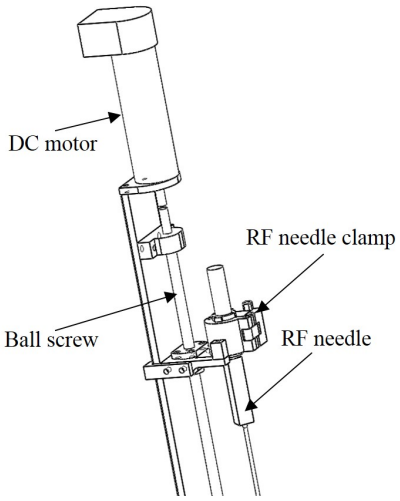

Figure 4.3: Translational subassembly of the RCM mechanism.

A problem of many RCM mechanisms is that the remote center of the surgical tool could not coincident with the insertion port. As illustrated in Figure 4.4, a gap between remote center of the surgical tool and insertion port on patient skin always exist because of the supporting parts in the RCM mechanism. One way to

resolve this problem is to improve the mechanical design to make the gap as small as possible so that the size of the hole opened on human is acceptable. However, in previous designs [88, 92–97], the gap cannot be ignored even when the design was optimized and the mechanism was adjusted to appropriate position. In our design, we can minimize the gap between remote center of the RFA needle and insertion port on patient skin to about $30mm$. The RFA needle can move within 30° from the centerline (as shown in Figure 4.4) in the proposed RCM mechanism. In this case, the radius r of the hole created on human can be calculated by:

$$r = 30 \times tan(30°) = 10\sqrt{3}mm \approx 17.3mm, \tag{4.1}$$

which is quite a large incision and not suitable for percutaneous procedure. This implies that the multiple RFA needle insertions could not go through a SIP.

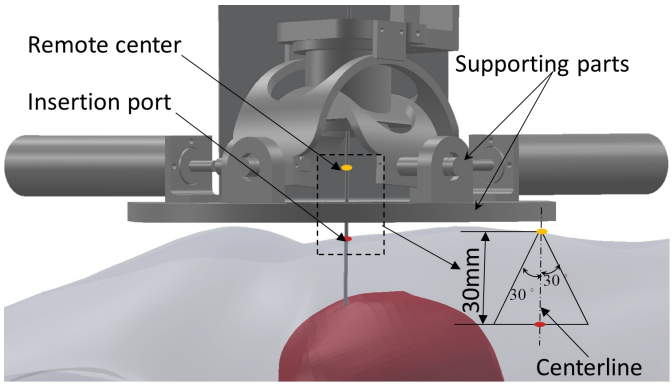

Figure 4.4: Gap between remote center of the surgical tool and insertion port on patient skin.

To overcome this problem caused by the gap between remote center of the needle and insertion port on patient skin, additional two degree of freedom for our RCM mechanism are added. Figure 4.5 shows an overview of our robotic system for RFA needle insertion. Two motorized linear slides are added to our robot system so that the RCM mechanism can move on a horizontal plane. For each RFA needle insertion, the RCM mechanism is moved to a position where the remote center of

RFA needle, insertion port on the patient and target point in the liver is on the same line (this line will be called "insertion line" for short). After the RCM is moved to the proper position, the RFA needle is adjusted to the direction of the insertion line by the rotational mechanism. Finally, The translational mechanism drives the RFA needle to the target point.

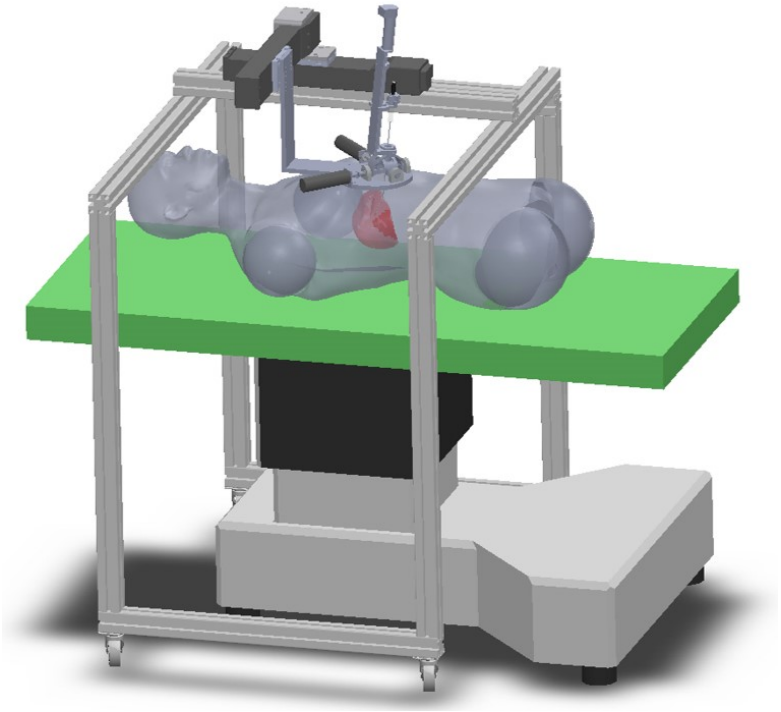

Figure 4.5: Overview of the robot system for RFA needle insertion.

To demonstrate that our design is suitable for RFA of large liver tumor in real surgical environment. The workspace of the RCM mechanism under different working conditions was investigated. Figure 4.6 shows the workspace of the proposed RCM mechanism. The shape of this workspace is a spherical sector which consists of a cone and a sphere cap. The volume covered by the workspace can be calculated by:

$$V = \frac{2\pi r^3}{3}(1 - cos(\theta)), \tag{4.2}$$

where r is the radius of the sphere, θ is half the cone angle which is the angle

between the rim of the cap and the direction to the middle of the cap as seen from the sphere center. For this spherical sector, r equals 180 mm and θ equals 30°.

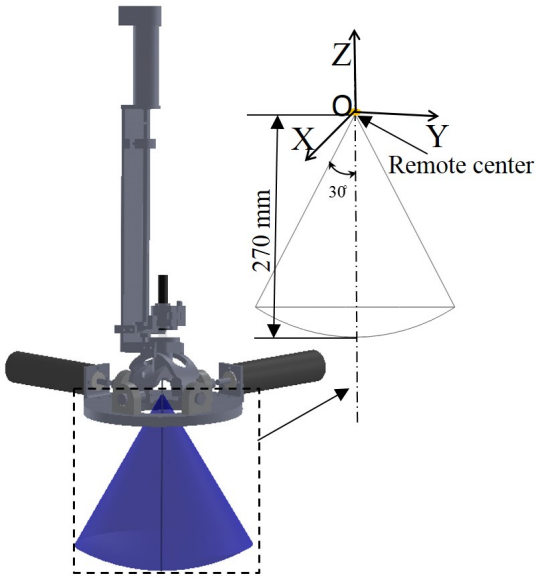

Figure 4.6: Workspace of the RCM mechanism.

As mentioned before, two motorized linear slides is added in our design because of the gap between remote center of the surgical tool and insertion port on patient skin. The distance of travel of the two motorized linear slides is 200 mm. Therefore, the range of motion of the RCM point is a square, the side length of which is 200 mm. The reachable workspace of the robot system can be obtained by moving the apex of the spherical sector (the workspace of the RCM mechanism) along the square. Figure 4.7 shows the reachable workspace of the robot system. However, the RFA needle is required to go through one selected insertion port on patient skin during percutaneous RFA of liver tumor. Considering this constrain, an effective workspace of the robot system in percutaneous RFA through SIP was simulated (Figure 4.8). In practice, the insertion port should be chosen where the effective workspace can cover the whole tumor.

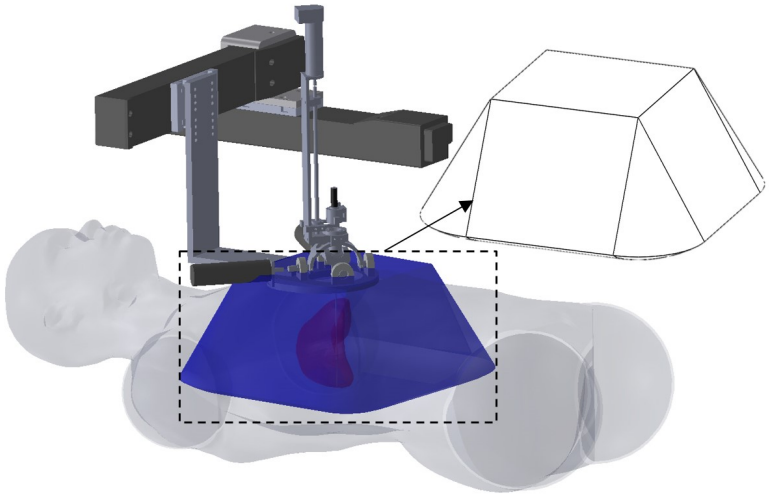

Figure 4.7: Reachable workspace of the robot system consisting of two translational robot arms and the RCM mechanism.

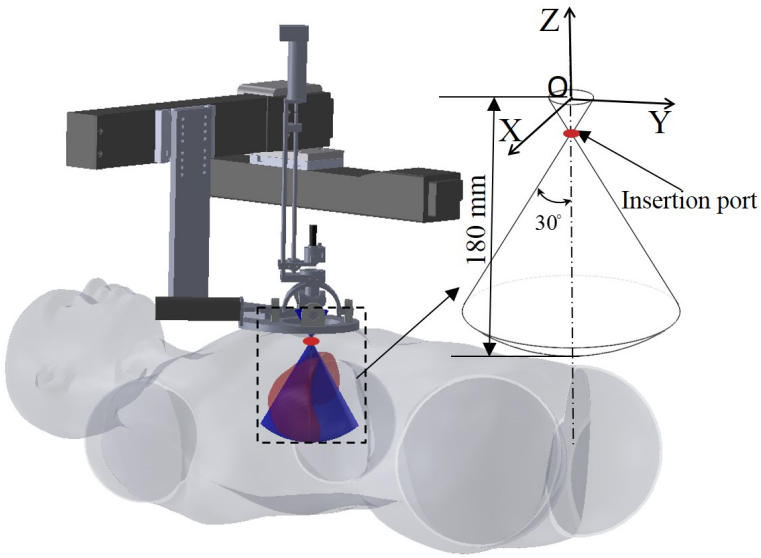

Figure 4.8: Effective workspace of the robot system in percutaneous RFA.

4.2 Kinematic Analysis and Simulation

In this section, we describe the kinematic analysis of the proposed RCM mechanism using a novel method. The new method is able to overcome the limitations of traditional kinematics analyzing method in previous studies [92, 93, 95] on similar mechanism. Instead of considering the motion of this RCM mechanism as a

result of two consecutive rotation about the X and Y axis of a fixed frame respectively, we showed that the motion of this RCM mechanism is actually determined by the intersection line of two planes attached to the two semi-circular arches. Jocobian analysis showed that singularity only occurs at this RCM point of this mechanism.

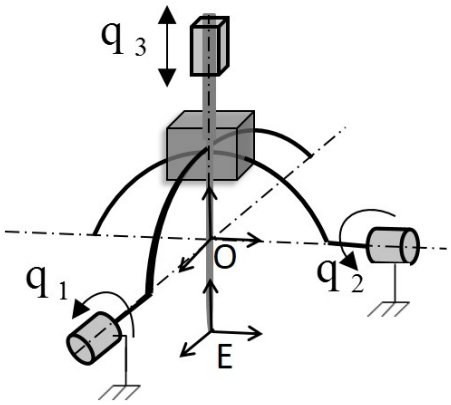

Figure 4.9: Schematic representation of RCM mechanism kinematics. $q_i, (i = 1, 2, 3, 4)$ represents the joint variable of each joint. O and E represent the base frame and tool frame respectively.

Figure 4.9 shows the schematic representation of RCM mechanism kinematics. The proposed RCM mechanism for RFA needle insertion has three independent joints: two revolution joints and one prismatic joint. In some studies([92, 93, 95]), the rotational motion of this kind of RCM mechanism is regarded as the result of two consecutive motion: roll (rotation about a fixed axis X) and pitch (rotation

about a fixed axis Y)(Figure 4.10). The rotation matrix ${}^{O}_{O'}\mathrm{R}$ is calculated by:

$$
\begin{aligned}
{}^{O}_{O'}\mathrm{R} &= R_Y(\beta)R_X(\gamma) \\
&= \begin{bmatrix} c\beta & 0 & s\beta \\ 0 & 1 & 0 \\ -s\beta & 0 & c\beta \end{bmatrix} \begin{bmatrix} 1 & 0 & 0 \\ 0 & c\gamma & -s\gamma \\ 0 & s\gamma & c\gamma \end{bmatrix} \\
&= \begin{bmatrix} c\beta & s\beta s\gamma & s\beta c\gamma \\ 0 & c\gamma & -s\gamma \\ -s\beta & c\beta s\gamma & c\beta c\gamma \end{bmatrix},
\end{aligned} \tag{4.3}
$$

where γ and β represent the roll and pitch angle respectively.

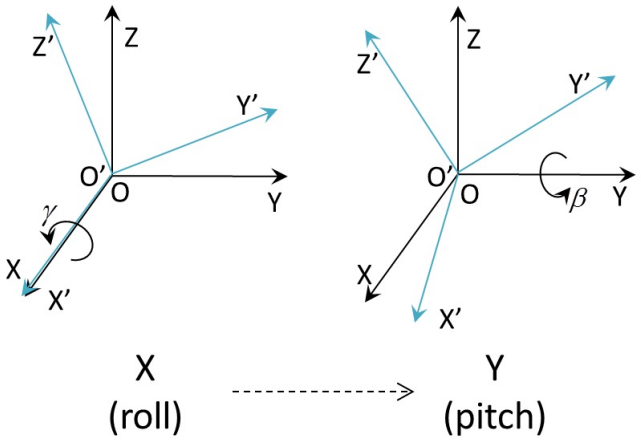

Figure 4.10: Kinematic analysis in previous paper. O and O' denote the fixed and moving frame respectively. γ and β are the roll and pitch angle respectively.

The problem of the previous kinematic analysis would be noticed by considering the following two cases: A. Do the roll motion first and then do the pitch motion; B. Do the pitch motion first and then do the roll motion. Assume the pitch angles in the two cases are the same and so are the roll angles. From Equation 4.3, the rotation matrix will be different in cases A and B. However, it is obvious that the orientation of the RFA needle is the same when we change the rotation order in

our RCM mechanism. The motion of this RCM mechanism is not simply pitch and roll motion because the pipe slider inside the two arches is a moving part. In our analysis, we will show that the motion of this RCM mechanism is actually determined by the intersection line of two planes attached to the two semi-circular arches.

Suppose the joint vector $q = [q_1, q_2, q_3]$ denotes the rotation angle about base frame X axis, rotation angle about base frame Y axis and translation along tool frame Z axis respectively. Axis Z_x is obtained by rotating Z axis about X by q_1, and axis Z_y is obtained by rotating Z axis about Y by q_2. As illustrated in Figure 4.11, the forward kinematics of the RCM mechanism is derived by finding the intersection line of two planes XOZ_x and YOZ_y. This intersection line is coincident with the Z axis of the tool frame.

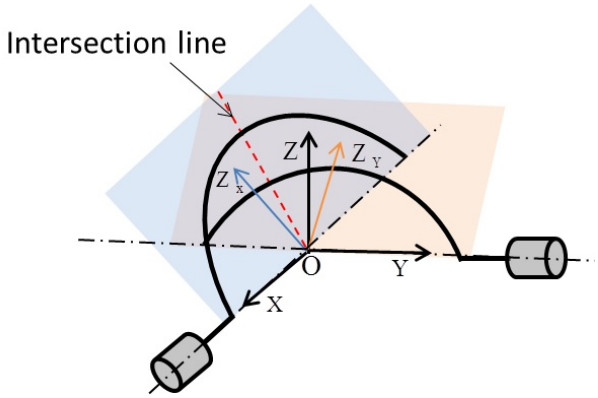

Figure 4.11: Illustration of the forward kinematics.

Suppose $\vec{x}$, $\vec{y}$, $\vec{z_x}$, $\vec{z_y}$ are the unit vector along OX, OY, OZ_x, OZ_y respectively. n_x and n_y are the normal vector to the plane XOZ_x and YOZ_y respectively. $\vec{t_z}$ represents a vector along the intersection line of plane XOZ_x and plane YOZ_y.

$\vec{t_z}$ could be obtained by

$$\begin{aligned}
\vec{t_z} &= n_x \times n_y \\
&= (z_x \times \vec{x}) \times (z_y \times \vec{y}) \\
&= \left(\begin{bmatrix} 0 \\ -s_1 \\ c_1 \end{bmatrix} \times \begin{bmatrix} 1 \\ 0 \\ 0 \end{bmatrix} \right) \times \left(\begin{bmatrix} s_2 \\ 0 \\ c_2 \end{bmatrix} \times \begin{bmatrix} 0 \\ 1 \\ 0 \end{bmatrix} \right) \\
&= \begin{bmatrix} c_1 s_2 \\ -s_1 c_2 \\ c_1 c_2 \end{bmatrix},
\end{aligned} \tag{4.4}$$

where s_i and c_i denote sine and cosine function of joint variable q_i. The vector $\vec{t_z}$ represents the direction of the Z axis of tool frame. The position of the needle tip with respect to the base frame can be obtained by

$${}^{O}\mathrm{P}_{E} = \begin{bmatrix} p_x \\ p_y \\ p_z \end{bmatrix} = \frac{q_3 \vec{t_z}}{\left\| \vec{t_z} \right\|} = \frac{q_3}{\alpha} \begin{bmatrix} c_1 s_2 \\ -s_1 c_2 \\ c_1 c_2 \end{bmatrix}, \tag{4.5}$$

where $\alpha = (c_1^2 s_2^2 + s_1^2 c_2^2 + c_1^2 c_2^2)^{\frac{1}{2}} = (1 - s_1^2 s_2^2)^{\frac{1}{2}}$.

Let the X axis of tool frame lie in plane XOZ_x. Therefore, a vector $\vec{t_y}$ along the tool frame Y axis can be obtained by

$$\begin{aligned}\vec{t_y} &= \vec{t_z} \times \vec{x} \\ &= \begin{bmatrix} c_1 s_2 \\ -s_1 c_2 \\ c_1 c_2 \end{bmatrix} \times \begin{bmatrix} 1 \\ 0 \\ 0 \end{bmatrix} \\ &= \begin{bmatrix} 0 \\ c_1 c_2 \\ s_1 c_2 \end{bmatrix}. \end{aligned} \tag{4.6}$$

Assume $\vec{t_x}$ is a vector along the tool frame X axis, $\vec{t_x}$ can then be calculated from $\vec{t_y}$ and $\vec{t_z}$

$$\begin{aligned}\vec{t_x} &= \vec{t_y} \times \vec{t_z} \\ &= \begin{bmatrix} 0 \\ c_1 c_2 \\ s_1 c_2 \end{bmatrix} \times \begin{bmatrix} c_1 s_2 \\ -s_1 c_2 \\ c_1 c_2 \end{bmatrix} \\ &= \begin{bmatrix} c_2^2 \\ s_1 s_2 c_1 c_2 \\ -c_1^2 s_2 c_2 \end{bmatrix}. \end{aligned} \tag{4.7}$$

The homogeneous transformation matrix from base frame O to tool frame E

can be constructed by

$$
\begin{aligned}
{}^{O}_{E}\mathrm{T} &= \begin{bmatrix} \frac{\vec{t_x}}{\|\vec{t_x}\|} & \frac{\vec{t_y}}{\|\vec{t_y}\|} & \frac{\vec{t_z}}{\|\vec{t_z}\|} & {}^{O}\mathrm{P}_{E} \\ 0 & 0 & 0 & 1 \end{bmatrix} \\
&= \begin{bmatrix} \frac{c_2^2}{\beta} & 0 & \frac{c_1 s_2}{\alpha} & \frac{q_3 c_1 s_2}{\alpha} \\ \frac{s_1 s_2 c_1 c_2}{\beta} & c_1 & \frac{-s_1 c_2}{\alpha} & \frac{-q_3 s_1 c_2}{\alpha} \\ \frac{-c_1^2 s_2 c_2}{\beta} & s_1 & \frac{c_1 c_2}{\alpha} & \frac{q_3 c_1 c_2}{\alpha} \\ 0 & 0 & 0 & 1 \end{bmatrix},
\end{aligned} \tag{4.8}
$$

where $\beta = (c_2^4 + s_1^2 s_2^2 c_1^2 c_2^2 + c_1^4 s_2^2 c_2^2)^{\frac{1}{2}}$.

The inverse kinematics can then be derived from Equation 4.5 as below

$$
\begin{bmatrix} q_1 \\ q_2 \\ q_3 \end{bmatrix} = \begin{bmatrix} -arctan(p_y/p_z) \\ arctan(p_x/p_z) \\ \sqrt{p_x^2 + p_y^2 + p_z^2} \end{bmatrix}, \tag{4.9}
$$

where $q_1, q_2 \in (-\pi/2, \pi/2)$.

The Jocobian matrices of this mechanism can be calculated by

$$
\begin{aligned}
J &= \begin{bmatrix} \frac{\partial(p_x)}{\partial q_1} & \frac{\partial(p_x)}{\partial q_2} & \frac{\partial(p_x)}{\partial q_3} \\ \frac{\partial(p_y)}{\partial q_1} & \frac{\partial(p_y)}{\partial q_2} & \frac{\partial(p_y)}{\partial q_3} \\ \frac{\partial(p_z)}{\partial q_1} & \frac{\partial(p_z)}{\partial q_2} & \frac{\partial(p_z)}{\partial q_3} \end{bmatrix} \\
&= \begin{bmatrix} \frac{-\alpha^2 q_3 s_1 s_2 + q_3 s_1 c_1^2 s_2^3}{\alpha^3} & \frac{\alpha^2 q_3 c_1 c_2 + q_3 s_1^2 c_1 s_2^2 c_2}{\alpha^3} & \frac{c_1 s_2}{\alpha} \\ \frac{-\alpha^2 q_3 c_1 c_2 - q_3 s_1^2 c_1 s_2^2 c_2}{\alpha^3} & \frac{\alpha^2 q_3 s_1 s_2 - q_3 s_1^3 c_2^2 s_2}{\alpha^3} & \frac{-s_1 c_2}{\alpha} \\ \frac{-\alpha^2 q_3 s_1 c_2 + q_3 s_1 c_1^2 s_2^2 c_2}{\alpha^3} & \frac{-\alpha^2 q_3 c_1 s_2 + q_3 s_1^2 c_1 s_2 c_2}{\alpha^3} & \frac{c_1 c_2}{\alpha} \end{bmatrix}.
\end{aligned} \tag{4.10}
$$

The determinant of the Jacobian matrices is

$$det(J) = q_3^2 c_1 c_2 (c_1^2 + c_2 s_1^2 + \frac{s_1^2 s_2^2}{\alpha^3}). \tag{4.11}$$

Since $q_1, q_2 \in [-\pi/6, -\pi/6]$, every term in $c_1 c_2 (c_1^2 + c_2 s_1^2 + \frac{s_1^2 s_2^2}{\alpha^3})$ is larger than zero. Thus the determinant of the Jacobian matrices would be zero only if q_3 equals zero. Hence, the singularity occurs only at the RCM point, which is an expected characteristic of RCM mechanism.

To verify the correctness of our kinematic analysis and validate the feasibility of this robot system for multiple RFA needle insertions, we conducted a simulation study based on a CT image of a patient's liver organ. Firstly, three dimensional models of human, liver and liver tumor were reconstructed from CT data. A preoperative RFA ablation planning method according to our previous research [17] was then applied to determine the location of each ablation. Each ablation volume was represented by a sphere. The multiple ablations were aligned so that the total ablation volume covers the entire tumor. After the ablation planing, the two motorized linear slides adjusted the RCM mechanism to a proper position where the effective workspace of the robot system could cover the entire tumor. For the convenience of inverse kinematics calculation, the base frame was attached to the supporting plane of the RCM mechanism with the origin located at the RCM point. The coordinate system was then established with regard to this base frame. From the ablation plan, the coordinates of all the RFA needle insertion target points could be obtained. A sequence of these target points was specified for the RFA needle insertion simulation. For every target point, inverse kinematics was conducted to calculate the joint parameters. In order to maintain SIP during multiple RFA needle insertions, the RCM mechanism was moved to the position where the RCM point, insertion port and target point of insertion are located at the same line. Since the base frame is attached to the RCM mechanism, the

coordinates of the target points were adjusted after every movement of the RCM mechanism.

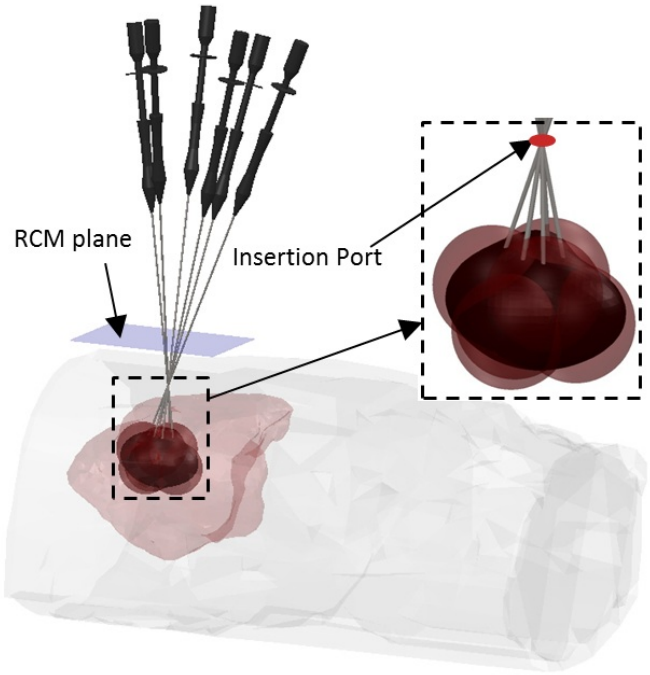

Figure 4.12: Multiple RFA ablations of liver tumor using our robot system. The models of human (in gray color), liver (in light red color) and liver tumor (in black) are constructed from a set of CT data of a real patient. Sphere (in dark red) with radius 25mm is used to estimate the destruction volume of one RFA ablation. The horizental plane where the RCM point moves is indicated as RCM plane.

Figure 4.12 shows the simulation results of multiple RFA ablations of liver tumor using our robot system. The effect of gap between RCM point and insertion port is counteracted by allowing the RCM mechanism move in a horizontal plane. In this simulation, six ablations are required to cover the entire tumor. All six ablations pass through SIP as indicated by the red dot in the figure.

To prove the correctness of our new analytical method for modeling the kinematics of the RCM mechanism, each RFA needle insertion is displayed in Figure 4.13. As shown in Figure 4.13, every needle is inserted to the correct position (the center of each sphere) as planned in the preoperative ablation planing. The needle insertion in this simulation is controlled by the joint parameters, which is

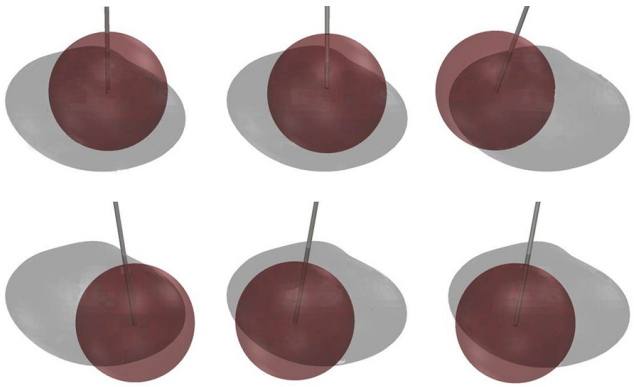

Figure 4.13: Each RFA needle insertion and ablation volume. The shape in gray represents liver tumor. Each red sphere represents one ablation volume. The position of each sphere is preplanned in the ablation plan. The goal of this simulation is to show that the RFA needle can be placed in the center of each planned sphere through SIP.

calculated from the inverse kinematics presented in previous section. The results indicate that our new understanding of the motion of this RCM mechanism is correct.

4.3 Dynamics Analysis

The kinematic analysis in Section 4.2 describes the motion of the RCM mechanism without consideration of the associated torques. In order to know the torques that have caused the motion, the dynamic model of this RCM mechanism is required. This dynamic model can help us to select appropriate motors and design control strategies.

In our RCM mechanism, there are two rotational joints and one translational joint. The translational joint is realized using a ball screw system. The axial force along the ball screw can be calculated by:

$$F = 2\pi M/P, \tag{4.12}$$

where F is the axial force along the ball screw, M is the torque of the motor, P is

the lead of the ball screw. The lead of our ball screw is $P = 0.001m$. According to Equation 4.12, $F \approx 6283M$. The translational joint can provide sufficient force for the needle insertion. Therefore, the translational joint is ignored in the dynamic analysis.

Some assumptions and simplifications are made to derive the dynamic model. Firstly, the mass of the two semi-circular arches (see Figure 4.2) are ignored since they are very light compared to the sliding mechanism within them (see Figure 4.14). Secondly, the mass of the sliding mechanism is assumed to be lumped at its center of gravity and the center of gravity will not move when the needle moves. Lastly, the frictions are ignored in the dynamics analysis.

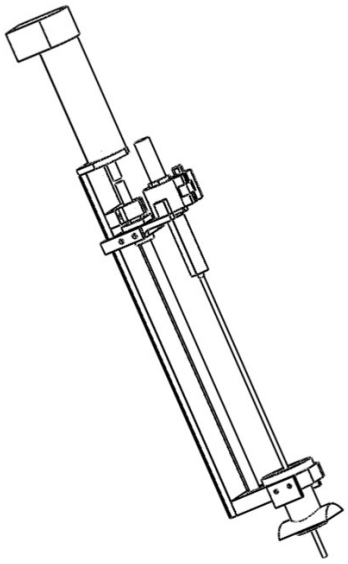

Figure 4.14: The sliding mechanism within the two arches.

The schematic representation of the simplified dynamic model is shown in Figure 4.15. The motion of this RCM mechanism can be considered as a point mass doing circular motions around the x axis and y axis. Assuming L is the distance from the point mass to the RCM point and m is the mass of the sliding mechanism. The point mass has multiple motions, the circular motion around x axis and circular motions around y axis; v_1 is the speed orbiting x axis and v_2 is the speed orbiting

y axis; q_1 and q_2 are the rotational angles of the two joints respectively.

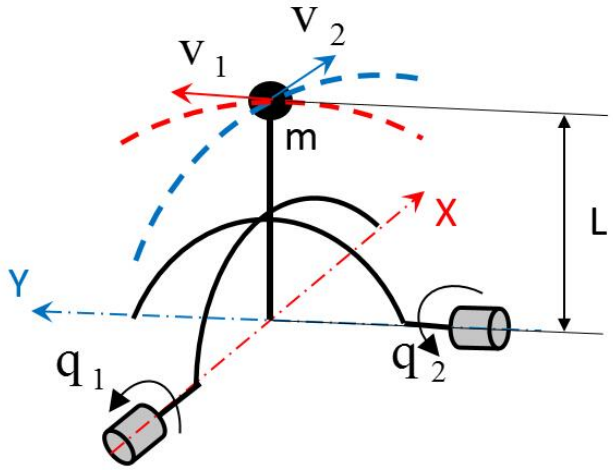

Figure 4.15: Schematic representation of the simplified dynamic model.

The dynamic model can be derived by Newton-Euler formulation with dynamic equation represented by

$$\tau = D(q)\ddot{q} + C(q,\dot{q})\dot{q} + Gq, \tag{4.13}$$

where $D(q)$, $C(q,\dot{q})$ and $G(q)$ are the dynamic coefficients of the robot. The inertia matrix, $D(q)$ is a square matrix and contains the acceleration terms. Each diagonal element of the matrix, for example, d_{ii} , describes the acceleration of joint i caused by torque τ_i. Every other element, for example, d_{ik}, describe the reaction torque which is induced by the acceleration of joint k and acts at joint i and vice versa. The $C(q,\dot{q})$ matrix is a nonlinear coriolis and centrifugal force vector. The centrifugal force terms contain the square of the joint velocities ($\dot{q}_i^2$) whereas the Coriolis force terms contain the product of two joint velocities ($\dot{q}_i\dot{q}_j$). The $G(q)$ matrix is a vector of the gravitational forces acting on the mechanism. It represents the moment generated by gravity at the axis of joint i, in the current configuration of the system. The three matrices $D(q)$, $C(q,\dot{q})$ and $G(q)$ can be

calculated by the following procedure.

As shown in Figure 4.15, the speed v_1 and v_2 can be calculated by

$$v_1 = \dot{q}_1 L cos q_2, \tag{4.14}$$

and

$$v_2 = \dot{q}_2 L cos q_1. \tag{4.15}$$

The kinetic energy of the system, K, can be derived by

$$\begin{aligned} K &= \frac{1}{2} m {v_1}^2 + \frac{1}{2} m {v_1}^2 \\ &= \frac{1}{2} \dot{q}^T \begin{bmatrix} mL^2 cos^2 q_2 & 0 \\ 0 & mL^2 cos^2 q_1 \end{bmatrix} \dot{q}, \end{aligned} \tag{4.16}$$

where $\dot{q} = [\dot{q}_1, \dot{q}_2]^T$. So, $D(q)$ can be calculated by

$$D(q) = \begin{bmatrix} mL^2 cos^2 q_2 & 0 \\ 0 & mL^2 cos^2 q_1 \end{bmatrix}. \tag{4.17}$$

$C(q, \dot{q})$ can be calculated by $C_{kj} = \sum_{i=1}^{n} C_{ijk} \dot{q}_i$, where $C_{ijk} = \frac{1}{2}(\frac{\partial d_{kj}}{\partial q_i} + \frac{\partial d_{ki}}{\partial q_j} -$

$\frac{\partial d_{ij}}{\partial q_k}$). Hence,

$$
\begin{aligned}
C_{111} &= \frac{1}{2}\frac{\partial d_{11}}{\partial q_1} = 0 \\
C_{112} &= \frac{\partial d_{21}}{\partial q_1} - \frac{1}{2}\frac{\partial d_{11}}{\partial q_2} = mL^2 sinq_2 cosq_2 \\
C_{121} = C_{211} &= \frac{1}{2}\frac{\partial d_{11}}{\partial q_2} = -mL^2 sinq_2 cosq_2 \\
C_{122} = C_{212} &= \frac{1}{2}\frac{\partial d_{22}}{\partial q_1} = -mL^2 sinq_1 cosq_1 \\
C_{221} &= \frac{\partial d_{12}}{\partial q_2} - \frac{1}{2}\frac{\partial d_{22}}{\partial q_1} = mL^2 sinq_1 cosq_1 \\
C_{222} &= \frac{1}{2}\frac{\partial d_{22}}{\partial q_2} = 0,
\end{aligned}
$$

and

$$
\begin{aligned}
C_{11} &= C_{111}\dot{q}_1 + C_{211}\dot{q}_2 = -mL^2 sinq_2 cosq_2 \dot{q}_2 \\
C_{12} &= C_{121}\dot{q}_1 + C_{221}\dot{q}_2 = mL^2(sinq_1 cosq_1 \dot{q}_2 - sinq_2 cosq_2 \dot{q}_1) \\
C_{21} &= C_{112}\dot{q}_1 + C_{212}\dot{q}_2 = mL^2(sinq_2 cosq_2 \dot{q}_1 - sinq_1 cosq_1 \dot{q}_2) \\
C_{22} &= C_{122}\dot{q}_1 + C_{222}\dot{q}_2 = -mL^2 sinq_1 cosq_1 \dot{q}_1.
\end{aligned}
$$

$C(q, \dot{q})$ is

$$
C(q,\dot{q}) = \begin{bmatrix} -mL^2 sinq_2 cosq_2 \dot{q}_2 & mL^2(sinq_1 cosq_1 \dot{q}_2 - sinq_2 cosq_2 \dot{q}_1) \\ mL^2(sinq_2 cosq_2 \dot{q}_1 - sinq_1 cosq_1 \dot{q}_2) & -mL^2 sinq_1 cosq_1 \dot{q}_1 \end{bmatrix}. \tag{4.18}
$$

The potential energy of the system P is

$$
P = mgLcosq_1 cosq_2. \tag{4.19}
$$

Hence, $G(q)$ is:

$$P = \frac{\partial P}{\partial q} = \begin{bmatrix} -mgLsinq_1cosq_2 \\ -mgLcosq_1sinq_2 \end{bmatrix}. \tag{4.20}$$

Substituting the expressions of $D(q)$, $C(q, \dot{q})$ and $G(q)$, the dynamic equation of the mechanism can be expressed as

$$\begin{aligned} \tau = & \begin{bmatrix} mL^2cos^2q_2 & 0 \\ 0 & mL^2cos^2q_1 \end{bmatrix} \begin{bmatrix} \ddot{q}_1 \\ \ddot{q}_1 \end{bmatrix} \\ & + \begin{bmatrix} -mL^2sinq_2cosq_2\dot{q}_2 & mL^2(sinq_1cosq_1\dot{q}_2 - sinq_2cosq_2\dot{q}_1) \\ mL^2(sinq_2cosq_2\dot{q}_1 - sinq_1cosq_1\dot{q}_2) & -mL^2sinq_1cosq_1\dot{q}_1 \end{bmatrix} \begin{bmatrix} \dot{q}_1 \\ \dot{q}_1 \end{bmatrix} \\ & + \begin{bmatrix} -mgLsinq_1cosq_2 \\ -mgLcosq_1sinq_2 \end{bmatrix}. \end{aligned} \tag{4.21}$$

4.4 Integrative Velocity and Position Control

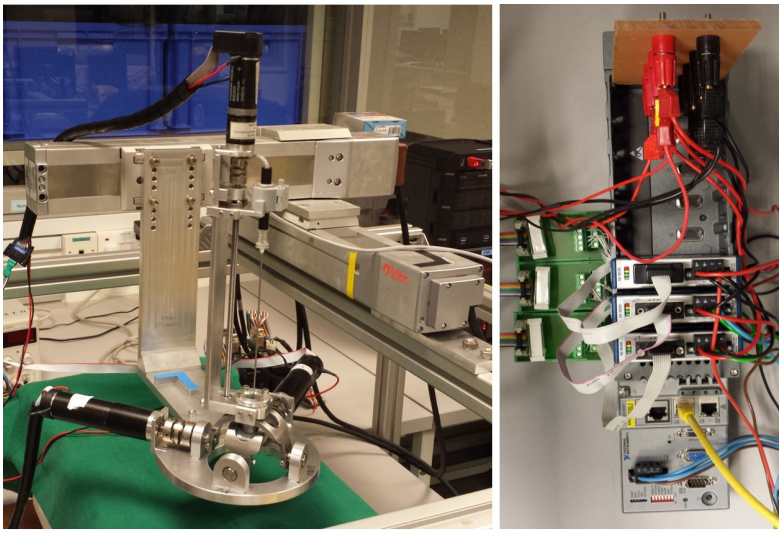

(a) RFA needle insertion robot (b) Controller

Figure 4.16: Robot system overview. (a)Setup of RFA needle insertion robot,which consists of the RCM mechanism and the motorized linear slides, in real scenario. (b)Controller of the RFA needle insertion robot.

The RFA needle insertion robot consists of a RCM mechanism and two motorized linear slides. The two motorized linear slides are used to move the RCM mechanism in horizontal plane (see Figure 4.16(a)). The RCM mechanism has three independent DOFs. The control scheme we described here is focuses on the three DC motors of the RCM mechanism. As shown in Figure 4.16(a), the two rotational joints and one translational joints of the RCM mechanism are all driven by DC motors. An integrated controller and chassis (NI cRIO-9081) is used to achieve real-time control of the DC motors.

The goal of this RFA needle insertion robot is to guide the RFA needle to the target spots in tumor accurately. Therefore, precise position control for the three DC motors is required. Moreover, to guarantee the RFA procedure performs safely and smoothly, the robot should move at a slow and steady speed. Speed control should also be added to the control scheme. Thus, an integrative speed and position control strategy was applied in our application.

The DC motor can be represented by a transfer function. A transfer function describes the mathematical relationship of the inputs and outputs of a system. In this case, the input to the system is voltage (V_m) and the output from the system is angular speed (Ω_m). The equation below can be used to represent the model of our DC Motor:

$$G(s) = \frac{\Omega_m(s)}{V_m(s)} = \frac{K_m}{J_{eq}R_m s + K_m^2}, \tag{4.22}$$

where K_m = Motor back electromotive force constant ($V/(rad/s)$), R_m = Motor armature resistance (Ω), J_{eq} = Equivalent moment of inertia ($kg * m^2$).

Figure 4.17 shows the control scheme for each DC motor. There are two closed-loops in the control scheme: speed control loop and position control loop. Proportional-integral-derivative(PID) controllers are used in both loops. The "Position/speed control selector" is used to determine which control command is selected as the in-

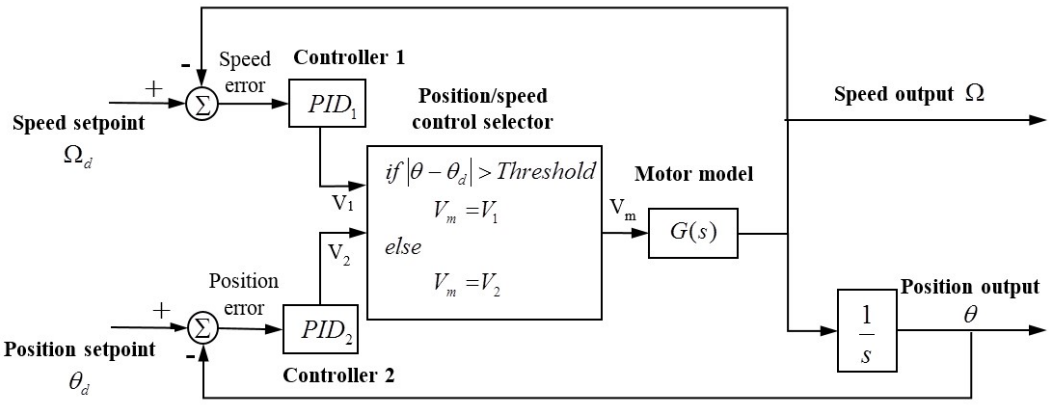

Figure 4.17: Schematic of the closed-loop control system

put of the motor. The "Position/speed control selector" works as follows. Firstly, a small threshold of the position value is determined. Then when the control commands(V_1 and V_2) of the speed and position control loop go into the selector, the following decision is made to determining which command is send to the motor: if the difference of motor position θ and position setpoint θ_d is greater than the threshold, V_1 will be send to the motor. Otherwise, V_2 is send to the motor. So, the motor firstly move at a given speed toward the new position under the speed control when a new position is send to the control system. Then when the motor position is closed enough to the new position, position control is applied to make sure the motor arrives at the given position.

The speed and position trajectories of the motors during an ablation process are plotted in Figures 4.18 to 4.20. From the figures, we can observe that the overshoots and oscillations for the position and speed trajectories are small for each motor. The motors can hence, move smoothly.

4.5 Experiments

To test the RFA needle insertion robot, we conducted two ex-vivo experiments and one in-vivo experiment. The first ex-vivo experiment aimed to test the ac-

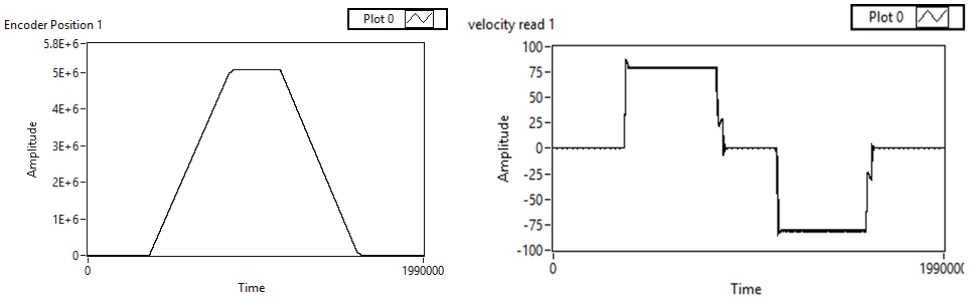

(a) (b)

Figure 4.18: Trajectories of motor 1 for one ablation. (a)Position trajectories of motor 1. (b)Speed trajectories of motor 1.

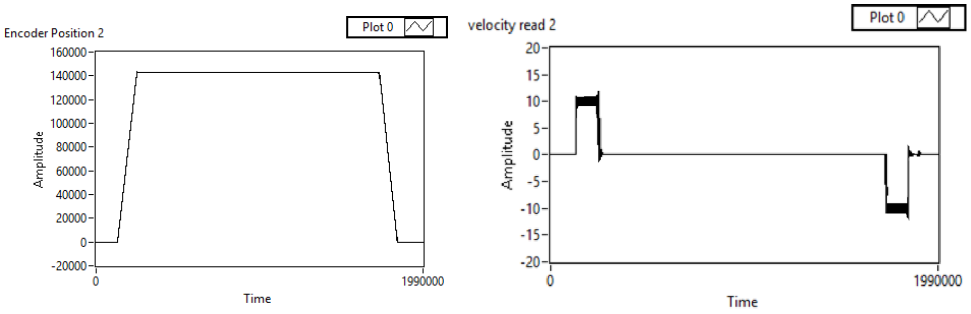

(a) (b)

Figure 4.19: Trajectories of motor 2 for one ablation. (a)Position trajectories of motor 2. (b)Speed trajectories of motor 2.

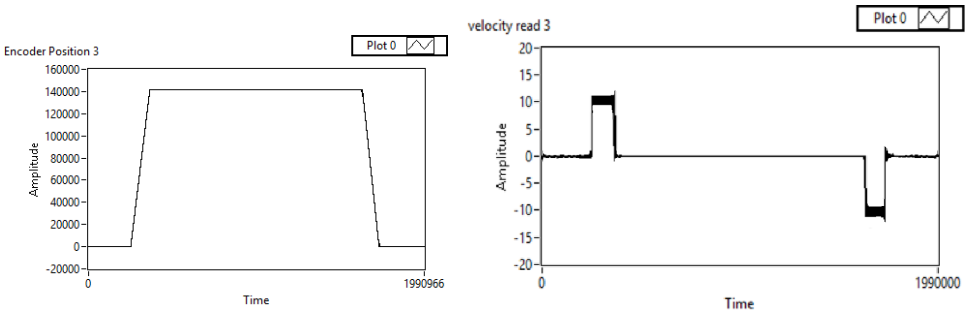

(a) (b)

Figure 4.20: Trajectories of motor 3 for one ablation. (a)Position trajectories of motor 3. (b)Speed trajectories of motor 3.

curacy of the robot while the second one demonstrated that the robot is able to guide the RFA needle to multiple targets through a single insertion port. The specifications of the RFA needle insertion robot were shown in Table 4.1. The

motors used to drive the two semi-circular arches are DC motors from Maxon (part number: 268214). The nominal torque for this motor is $85.6mNm$. This motor is equipped with a gear box with reduction rate of 1093:1 (part number: 166961). The motor used to drive the ball screw system is also DC motors from Maxon (part number: 339152). The nominal torque for this motor is $28.8mNm$. This motor is equipped with a gear box with reduction rate of 24:1 (part number: 144033).

Table 4.1: Specifications of the RFA needle insertion robot

Specifications	value	Specifications	value
Range of rotation angle (rad)	$(-\pi/6, \pi/6)$	Range of translation (mm)	(0,180)
Rotation speed (rad/s)	$\pi/30$	Translation speed(mm/s)	4
Maximum torque for arch rotation (N/m)	92.9	Maximum torque for ball screw system (N/m)	0.691
Accuracy of the linear slides (mm)	0.01	Weight of the sliding mechanism(kg)	0.62

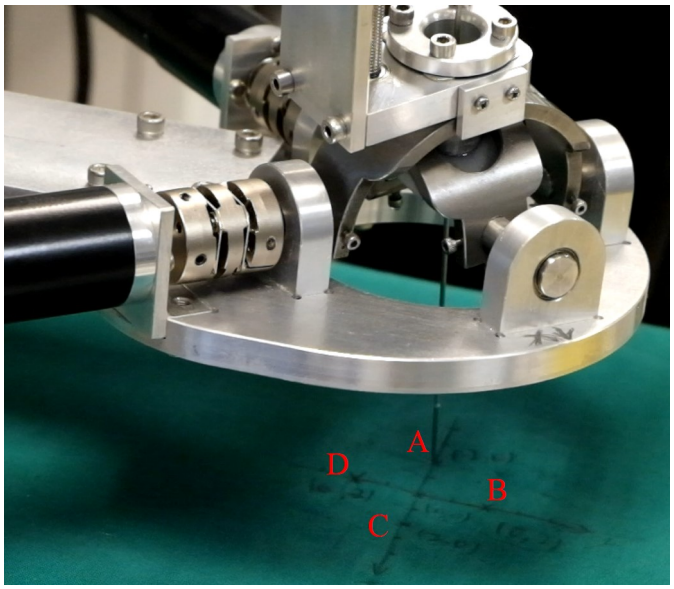

Figure 4.21: Accuracy test of the RFA needle insertion robot

Figure 4.21 shows the accuracy test of the RFA needle insertion robot. We drew a coordinate system and four target points(A, B, C, D) on a plane below the robot. The robot was required to guide the RFA needle to each target point. The experimental results show that the RFA needle can get to the target points very

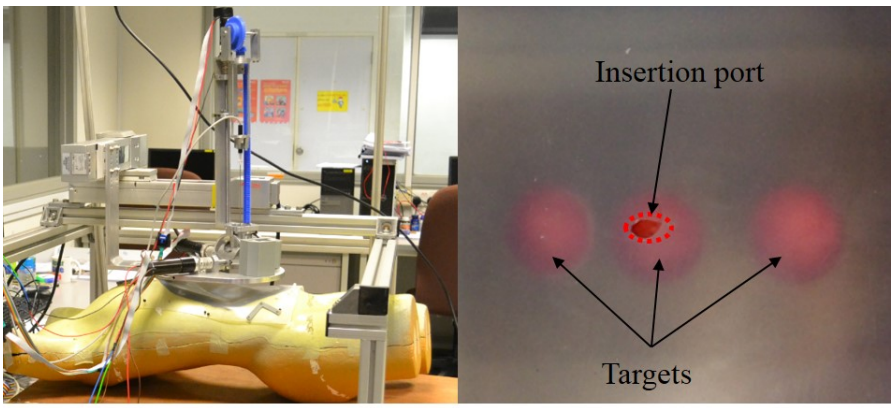

(a) Phantom test setup (b) Closeup on the Phantom

Figure 4.22: The RFA needle insertion robot tested on phantom. (a) System setup in a laboratory environment. (b) A silicon cover overlaying the phantoms chest and belly was used to simulate human skin. Three plasticine models (red balls) were used to mimic target tumors.

accurately: the errors are within 1mm. Figure 4.22 demonstrates a phantom test of the RFA needle insertion robot. In this experiment, the task for robot was to guide the RFA needle to the three targets through the insertion port on the skin(as shown in Figure 4.22(b)) and the robot completed the task very well.

Through the experiments, we showed that the accuracy of the RFA needle insertion robot is quite high and can satisfy the accuracy requirements in RFA application(as indicated by the doctor). The proposed robot can also achieve SIP during multiple RFAs, and this will greatly reduce the invasiveness of the RFA procedure.

4.6 Summary

In this chapter, a novel RCM mechanism for RFA needle insertion was designed, analyzed and implemented. The RCM mechanism used in our study is based on the concept of a spherical mechanism with two semi-circular arches. Compared to previous mechanisms in literature [91–98], additional two translational degrees were integrated to our mechanism. The modified RCM mechanism is capable of

conducting multiple RFA needle insertions through a SIP. We proposed a novel analyzing method to accurately model the motion of this mechanism. This method is able to overcome the limitations of previous methods in the literature. An integrative speed and position control strategy was used to achieve smooth and precise motion of the robot. Experimental results demonstrate the feasibility of our proposed RFA needle insertion robot in multiple RFAs application.

Chapter 5

Registration

In our robotic RFA needle insertion system, computed tomography (CT) images are used for pre-operative RFA planning. Clinicians are able to define the needle placements for RFA needle insertions. Accurately transforming the CT planning data to the robot coordinate system is a key issue in our study. In this chapter, a maker-based registration method was proposed to transform the CT image data to the robot coordinate system. This registration method achieves the registration by targeting feature points on the maker using our robot. This method works well in our system but may have limitations in other robotic systems. Therefore, a generic vision-based registration method was also proposed. The experiment results showed that both registration methods can achieve the required accuracy in RFA for liver tumor based on the clinician's feedback.

5.1 Reason for Registration

In pre-operative stage of RFA, CT images are used to do ablation planning. The planning data is based on a patient coordinate system. The patient coordinate system is built by the following step. First, we attached a L-shape marker to

the patient (see Figure 5.1(a)) and do a CT scan for the patient to obtain the 2D CT images (see Figure 5.1(b)). From the 2D CT images, we can reconstruct the 3D patient model (see Figure 5.1(c)). The patient coordinate system can then be established based on the marker (see Figure 5.1(c)). The planning data, including insertion port position and ablation target positions, are all based on this patient coordinate system.

(a) (b) (c)

Figure 5.1: Preoperative CT planning data in the patient coordinate system. (a)marker on the patient. (b)2D CT image. (c)3D reconstructed patient model.

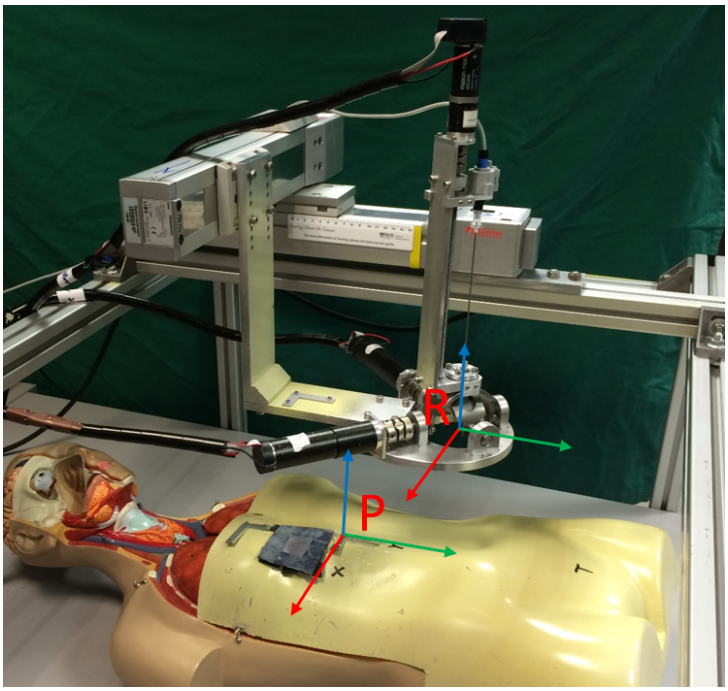

Figure 5.2: Illustration of the coordinate transformation from patient coordinate system P to robot frame coordinate system R.

To execute the RFA needle insertion using our robot system, the planning data need to be transformed from the patient coordinate system P to robot frame coordinate system R (as shown in Figure 5.2). The RFA needle insertion robot can then execute the task based on the kinematic analysis in Chapter 4.2. Therefore, an accurate registration method is required to enable correct execution of robotic RFA needle insertion.

5.2 Registration by Targeting Feature Points using Robot

As shown in Figure 5.2, the objective of registration is to find out the relationship between the patient coordinate system P and robot frame coordinate system R. An easy way to achieve this is to find the feature points on the marker and establish the transformation matrix based on the feature points' positions. As shown in Figure 5.3, the L-shape marker has three feature points which are O, X and Y respectively. O indicates the origin of the patient coordinate system P. X and Y indicate a point on the x axis and y axis of P respectively. The origin

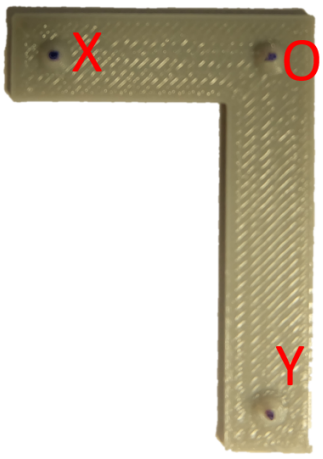

Figure 5.3: Feature points on the marker.

of the robot coordinate system R is the RCM point of the spherical mechanism, and the x axis and y axis of R are parallel to the two motorized linear stages (as shown in Figure 5.2). Let ${}^{R}_{P}T$ denote the transformation matrix from the patient coordinate system P to the robot coordinate system R. ${}^{R}_{P}T$ can be calculated by the following steps.

Firstly, we obtain coordinates of the three feature points in the robot coordinate system R. We control the robot to move along the x axis, y axis and z axis of R to reach the three feature points and record their coordinates by a LabVIEW program. The interface of the program is shown in Figure 5.4. The robot is allowed to move along the x axis, y axis and z axis by step ranging from 0.5 mm to 10 mm. After the needle reach a feature point, the user can click the related button to save the position. Assuming $O = (O_x, O_y, O_z)$, $X = (X_x, X_y, X_z)$ and

Figure 5.4: Interface of the position-obtaining LabVIEW program. The robot is allowed to move along the x axis, y axis and z axis by step ranging from 0.5mm to 10 mm. After the needle reach a feature point, the user can click the related button to save the position.

$Y = (Y_x, Y_y, Y_z)$, the vector along x axis and y axis of P expressed in R can be

calculated by

$$OX = (X_x - O_x, X_y - O_y, X_z - O_z), \tag{5.1}$$

and

$$OY = (Y_x - O_x, Y_y - O_y, Y_z - O_z). \tag{5.2}$$

The orthogonal unit vectors of P expressed in R can then be calculated by

$${}^{R}x_P = \frac{OX}{|OX|}, \tag{5.3}$$

and

$${}^{R}y_P = \frac{OY}{|OY|}, \tag{5.4}$$

and

$${}^{R}z_P = {}^{R}x_P \times {}^{R}y_P, \tag{5.5}$$

where ${}^{R}x_P$ is x_P expressed in R, ${}^{R}y_P$ is y_P expressed in R, ${}^{R}z_P$ is z_P expressed in R.

The rotation matrix from P to R can be calculated by

$${}^{R}_{P}R = [{}^{R}x_P, {}^{R}y_P, {}^{R}z_P]. \tag{5.6}$$

The transformation matrix ${}^{R}_{P}T$ can be calculated by

$${}^{R}_{P}T = \begin{pmatrix} {}^{R}_{P}R & O' \\ 0 & 1 \end{pmatrix}, \tag{5.7}$$

where $O' = (O_x, O_y, O_z)'$ is the origin of P expressed in R. With the transformation matrix ${}^{R}_{P}T$, the planning data can be transformed to the robot coordinate

system.

5.3 Registration Using Vision-based Method

Since our robot system can realize the movement along x axis, y axis and z axis by the two motorized linear slides and the translational mechanism for the RFA needle (as shown in Figure 5.5), we can conveniently move the RFA needle to the feature points by sending commends to robot manually. Therefore, the registration method by targeting feature points can be easily implemented in our robot system. However, this registration method may not suitable for other robot system which cannot realize the movement along x axis, y axis and z axis easily. For example, the Da Vinci robot (see Figure 5.6) achieves the movement of surgical

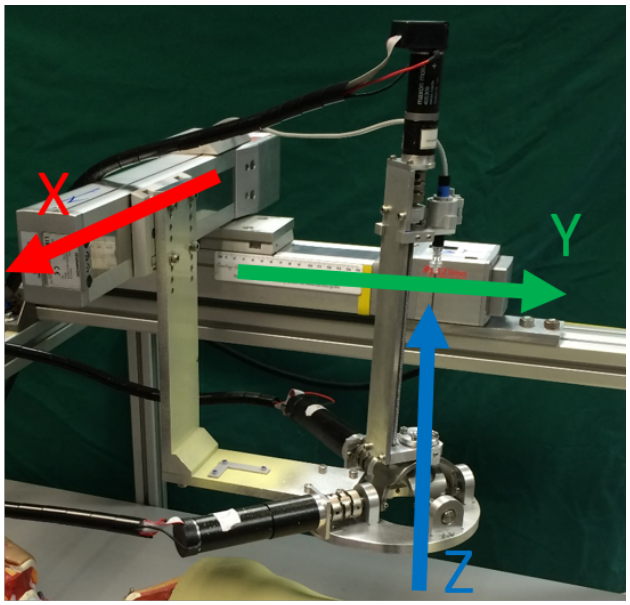

Figure 5.5: Realization of the movement along x axis, y axis and z axis in our robot system

tool by controlling multiple joints to work in coordination. It is hard to estimate how each joint should move in order to reach a point in the Cartesian coordinate system. Therefore, a vision-based registration method which can be applied in

general robot systems was proposed.

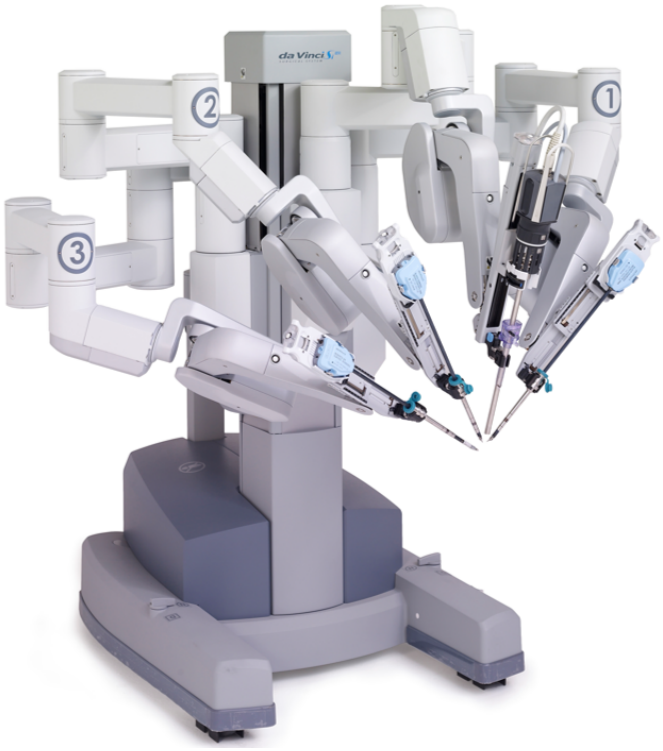

Figure 5.6: Davinci robot system.
(https://www.emaze.com/@AOIZCIFT/Surgical-Robot)

5.3.1 Vision-based Registration Process

The principle of this vision-based registration method is similar to that of the manually registration method in Section 5.2. Instead of obtaining the feature points position by the robot, KINECT (Microsoft, Redmond, Washington, United States) was used to detect the feature points on the markers and obtain their coordinates. As shown in Figure 5.7, two L-shape markers were used in the vision-based registration process. One marker was attached to the patient and the other was attached to the robot. Let W, P, R^*, R denote the world coordinate system established by the KINECT, the patient coordinate system, the robot marker coordinate system and the robot coordinate system respectively (See Figure 5.7).

Since R^* to R is a simple translation and the relative position of the two coordinate systems is fixed, the transformation matrix ${}^{R}_{R^*}T$ from R^* to R can be easily obtained. The transformation matrix ${}^{P}_{R}T$ from patient coordinate system P to robot coordinate system R can then be calculated by

$$ {}^{R}_{P}T = {}^{R}_{R^*}T \; {}^{R^*}_{P}T, \tag{5.8} $$

where ${}^{R}_{R^*}T$ denotes the transformation matrix from the patient coordinate system P to the robot marker coordinate system R^*. Therefore, the objective of this

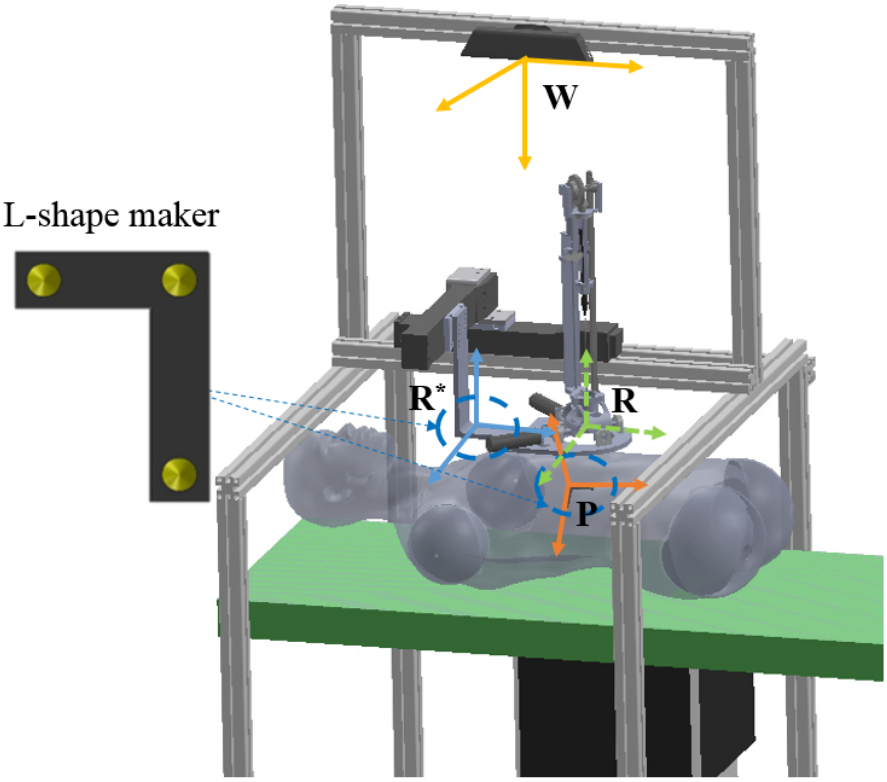

Figure 5.7: Vision-based registration process illustration.

vision-based registration is to find the transformation matrix ${}^{R^*}_{P}T$ from the patient coordinate system P to the robot coordinate system R^*. ${}^{R^*}_{P}T$ can be calculated

by

$$ {}^{R^*}_{P}T = {}^{R^*}_{W}T \; {}^{W}_{P}T = ({}^{W}_{R^*}T)^{-1} \; {}^{W}_{P}T, \tag{5.9} $$

where ${}^{W}_{R^*}T$ denotes the transformation matrix from the robot marker coordinate system R^* to the world coordinate system W and ${}^{W}_{P}T$ denotes the transformation matrix from the patient coordinate system P to the world coordinate system W. With KINECT, we are able to obtain the positions of feature points on patient marker and robot marker.

The marker used in the vision-based registration has two layers (see Figure 5.8). The marker cover has a flat surface and can be used to indicate the marker plane. After the marker plane is identified, the marker cover will be removed. The bottom marker with features can be used to mark the features on the 2D color image.

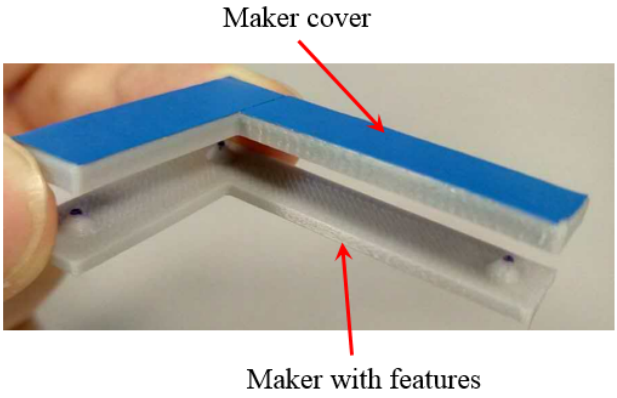

Figure 5.8: Maker used in the vision-based registration.

The positions of feature points on the marker can be obtained by the following steps. Firstly, the range (x, y, z range in W) of marker region should be identified so that the marker can be segmented from a small region. As shown in Figure 5.9(a), the environment in the full range point cloud view is very complex and it is hard to segment the marker. By defining the range of the marker, we can extract a very small region (see Figure 5.9(b)) to segment the marker. Based on

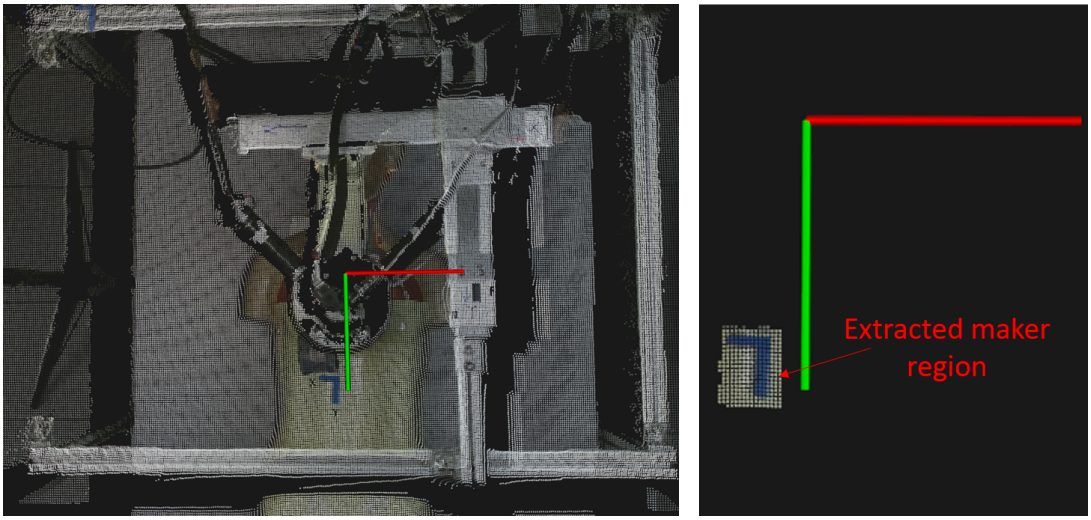

(a) (b)

Figure 5.9: Maker region extraction by defining the range of the marker region. (a)Full range point cloud view. (b)Extracted marker region.

the color difference of the marker (blue) and the background (yellow), the marker can be segmented out from the environment. Since noises exist in the point cloud data from the KINECT range camera, linear regression method is used to find the marker plane (See Figure 5.10). With the estimated marker plane, the feature

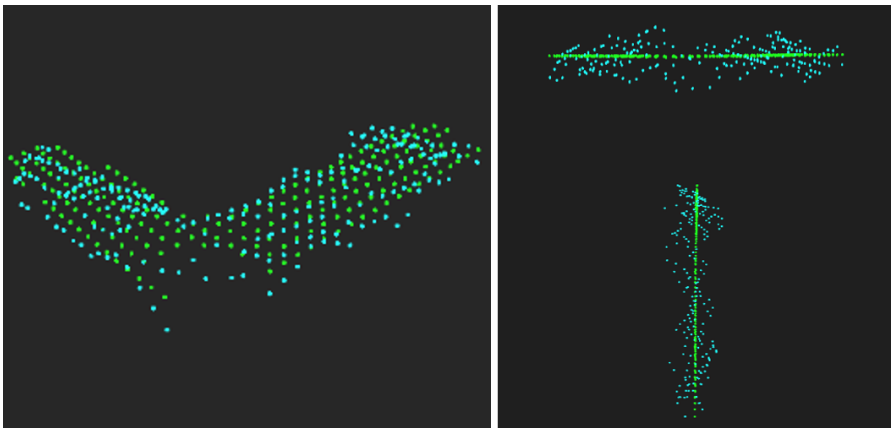

Figure 5.10: Marker plane fitting for patient coordinate system construction.

points on the marker can be determined by finding the feature points on the 2D color image from KINECT. Since there is a mapping between the depth image and the 2D color image, coordinates of the feature points can be obtained. ${}^{W}_{R^*}T$

and ${}^{W}_{P}T$ can then be calculated by following Equation 5.1 to Equation 5.7.

5.3.2 Registration Error Compensation

In our vision-based registration method, the feature points on marker are used to establish the coordinate system. However, small errors are inevitable when detecting the features on the marker due to the limit of camera precision. As shown in Figure 5.11, a small deviation in identifying the feature points can cause obvious errors of the coordinate system. The errors can be classified into two categories: rotational error and translational error. Since the translational error

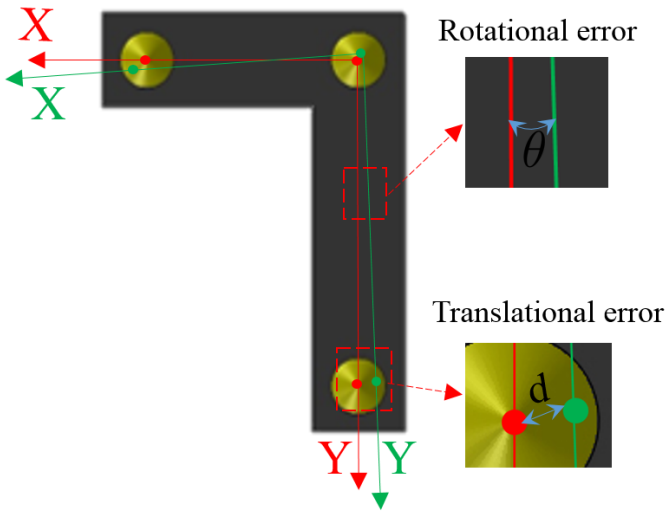

Figure 5.11: Illustration of the registration error when detecting the marker features.

d is always smaller than the radius of the feature region ($1.5mm$), it can be ignored in this application. However, the rotational error of the coordinate system may cause large error of the RFA targets. As shown in Figure 5.11, the rotational error θ can be estimated by

$$\theta = arctan(\frac{d}{L}), \tag{5.10}$$

where d is the translational error and L is the distance between two feature points. θ is a smaller angle since d is always very small. The targeting error will increase

as its distance from marker increases. In our application, the marker on the robot is quite far from the liver (about 200mm). Therefore, the errors caused by the robot marker cannot be ignored.

A simulation based on an animal experiment data was conducted to demonstrate the errors in a robotic RFA experiment environment. In this simulation, we assume the error of feature point x in robot marker is $-1mm$ and other feature points' positions are accurate. 16 targets inside the pig liver is selected. The actual targets and deviated targets are plotted in Figure 5.12. The error of every target is shown in Table

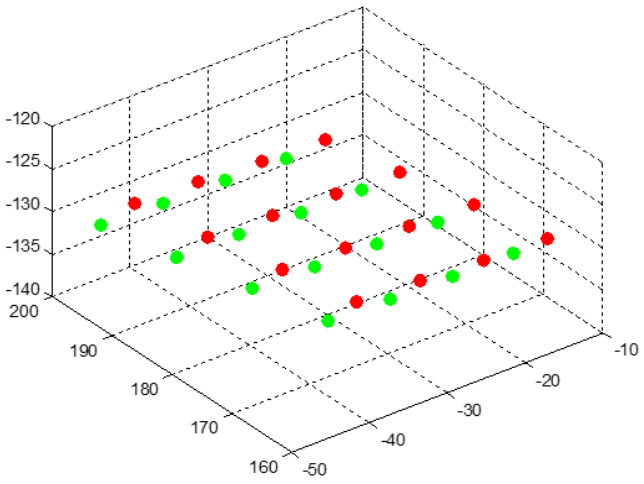

Figure 5.12: Simulation of the errors of 16 RFA targets. Red dots represent the actual targets, and green dots represent the deviated targets.

Table 5.1: Error of every target.

No.	Error(mm)	No.	Error(mm)	No.	Error(mm)	No.	Error(mm)
1	(-9.4,-1.4,0)	2	(-9.2,-1.6,0)	3	(-9.1,-2.1,0)	4	(-9.0,-2.7,0)
5	(-9.9,-1.2,0)	6	(-9.8,-1.7,0)	7	(-9.7,-2.3,0)	8	(-9.6,-2.8,0)
9	(-10.5,-1.3,0)	10	(-10.4,-1.8,0)	11	(-10.2,-2.4,0)	12	(-10.1,-2.9,0)
13	(-11.0,-1.4,0)	14	(-10.9,-2.0,0)	15	(-10.7,-2.5,0)	16	(-10.7,-3.0,0)

Although the error of each point is different, they can be regarded as the same value within a small zone. In practice, the size of ablated zone is small compared to the distance from the liver to robot marker. Therefore, it is possible to

compensate the errors by finding the error of one test point near the targets and calibration after the vision-based registration was proposed. The errors of targets can be compensated by the following steps. Firstly, a test point near the targets' zone (liver) should be defined. Since the patient marker is just near the liver, we can define one of its feature points as the the test point. The position of this test point can be obtained from the CT image. The position of this test point is then transformed to the robot coordinate system by ${}^{R}_{P}T$ so that the RFA needle can reach the test point. The error between the actual position of the needle tip and the test point can be obtained by two ways: (1). We can control the robot to move the needle to the test point and record the robot movement as described in Section 5.3. (2). Since the needle tip is close to the patient marker, the needle tip position in the patient marker coordinate system can be easily measured. The error with respect to the patient marker coordinate system P can be obtained. The error expressed in the robot coordinate system can be calculated by

$$E_R = {}^{R}_{P}T \; E_P, \tag{5.11}$$

where E_R and E_P is the error expressed in the robot coordinate system and the patient coordinate system respectively, ${}^{R}_{P}T$ is the transformation matrix from the patient coordinate system to the robot coordinate system. For each target, this error can be compensated before execution.

5.4 Evaluation for Registration Methods

To test the accuracy of the two registration methods, nine points on a coordinate paper were set as ablation target points(see Figure 5.13(a)). After registration, the robot performed the multiple RFA needle insertion to the nine points in se-

quence. Deviation of the RFA needle tip from target point was recorded as the execution error. The execution error can be read directly from the coordinate paper (see Figure 5.13(b)). The execution errors of the two registration methods are

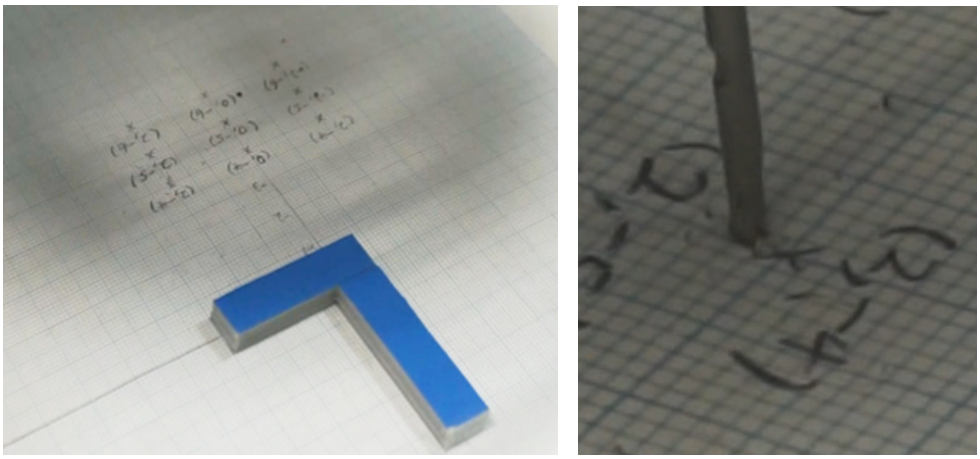

(a) (b)

Figure 5.13: Accuracy test for the two registration methods. (a)Target points on a coordinate paper . (b)Registration error read.

showed in Table 5.2. Method 1 represents the registration by targeting feature points using robot. Method 2 represents the vision-based registration method. The mean error and the standard deviation(STD) of the nine insertions were calculated. For Method 1, the mean error is $1.2mm$ and the STD is $0.1mm$. For Method 2, the mean error is $2.0mm$ and the STD is $0.5mm$. The small mean

Table 5.2: Execution errors of the two registration methods.(unit: mm)

	1	2	3	4	5	6	7	8	9	mean	STD
Method 1	1.3	1.2	1.3	1.4	1.1	1.2	1.3	1.1	1.2	1.2	0.1
Method 2	1.5	1.2	1.5	2.1	2.3	2.5	2.8	1.8	2.1	2.0	0.5

errors ($1.2mm$ and $2.0mm$) indicate that the robot system can achieve good accuracy using both registration methods. The STD of Method 1 ($0.1mm$)is much smaller than that of Method 2 ($0.5mm$). The reason is that a constant error for the test point was used to compensate all the targets' errors, which are actu-

ally different. Nonetheless, the experiment results showed that both registration methods can achieve the required accuracy in RFA for liver tumor.

5.5 Summary

In this chapter, two registration methods were proposed to transform the computed tomography (CT) image data to the robot coordinate system. The first registration method achieves the registration using our robot. This method can result in higher accuracy and can be easily implemented in our robotic system. However, it may have limitations in other robotic manipulators that cannot reach a target intuitively. Therefore, a generic vision-based registration method was also proposed. KINECT was used to detect the maker features in this method. To compensate the detecting error in KINECT, a calibration process need to be conducted before executing the task. The experiment results showed that both registration methods can achieve the required accuracy in RFA for liver tumor.

Chapter 6

Experiments

In this chapter, an ex-vivo experiment on phantom Model and an in-vivo experiment on Porcine Model are presented to test the effectiveness of our RFA needle insertion robot system in clinical environment. The aim of this RFA needle insertion robot system is to execute multiple RFAs from a single insertion port. Therefore, we tested two major performances of the robot system. Firstly, we want to ascertain that the robot can insert the RFA needle to the targets as planned. Secondly, we want to ascertain that the multiple insertions actually enter the patient body through a single insertion port. The experimental setup and work flow are introduced. Pre-operative planning, registration and intra-operative robot execution were conducted to test the whole system. During in-vivo experiment, the liver tissue is ablated after the needle insertion. The ablation result were evaluated by the clinician. The ex-vivo and in-vivo experimental results demonstrated that our robot system is able to conduct multiple RFAs with minimal incision effectively. Challenges and limitations are also discussed in this chapter.

6.1 Experimental Setup

Figure 6.1 shows the experimental setup of our robotic RFA needle insertion system. The system includes 1) the RFA needle insertion robot, 2) a computer for preoperative CT image processing and RFA planning, 3) a computer for robot control and 4) KINECT for registration. For in-vivo experiment on porcine model,

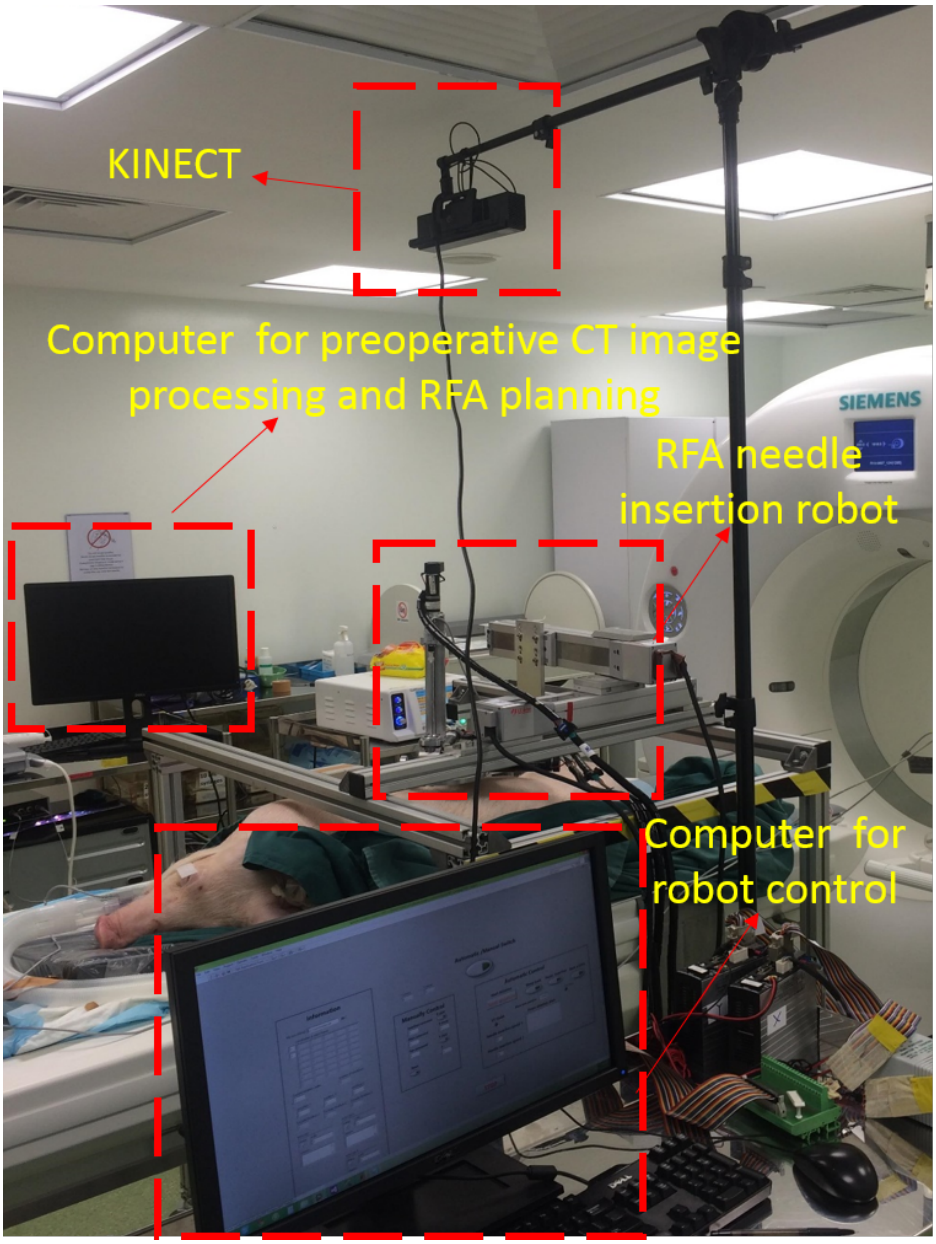

Figure 6.1: Experimental set-up of our robotic RFA needle insertion system.

the radio-frequency ablation generator (see figure 6.2(a)), breath control device for the patient (see Figure 6.2(b)), and monitoring equipment (see Figure 6.2(c)) for the patient are also included in the system. Since we use CT image data to

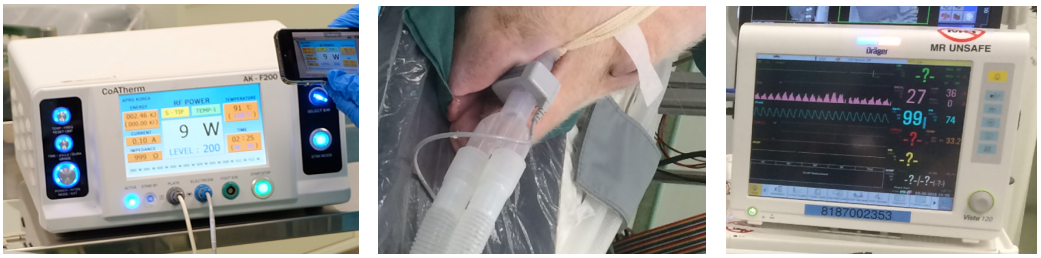

(a) (b) (c)

Figure 6.2: Additional devices for in-vivo experiment. (a)Radio-frequency ablation generator. (b) breath control device for the patient. (c) monitoring equipment for the patient

do RFA planning, it is important to avoid moving the patient too much after CT scan. Therefore, the whole system was set up in the CT room to make sure that the patient and liver positions during the RFA procedure is similar to those in the CT image. The robot frame has four wheels and can be moved when the patient need to do CT scan. After the CT scan is done, the robot can be moved to the right position and fixed by locking the wheels. The patient should be placed close to the RCM mechanism so that the workspace of the robot can cover a large volume of tumor. This can be achieved by adjusting the height of the surgical bed.

6.2 Experimental Work Flow and Software Architecture

As shown in Figure 6.3, the work flow of the robotic RFA needle insertion experiment can be divided into four main parts: preoperative RFA simulation, preoperative RFA planning, registration and robot execution. To reduce the du-

ration of the experiment, RFA simulation was conducted before the experiment. During the experiment, simulation results can be displayed to the clinician as a reference. The experiment begins with CT scan for the patient. When the pa-

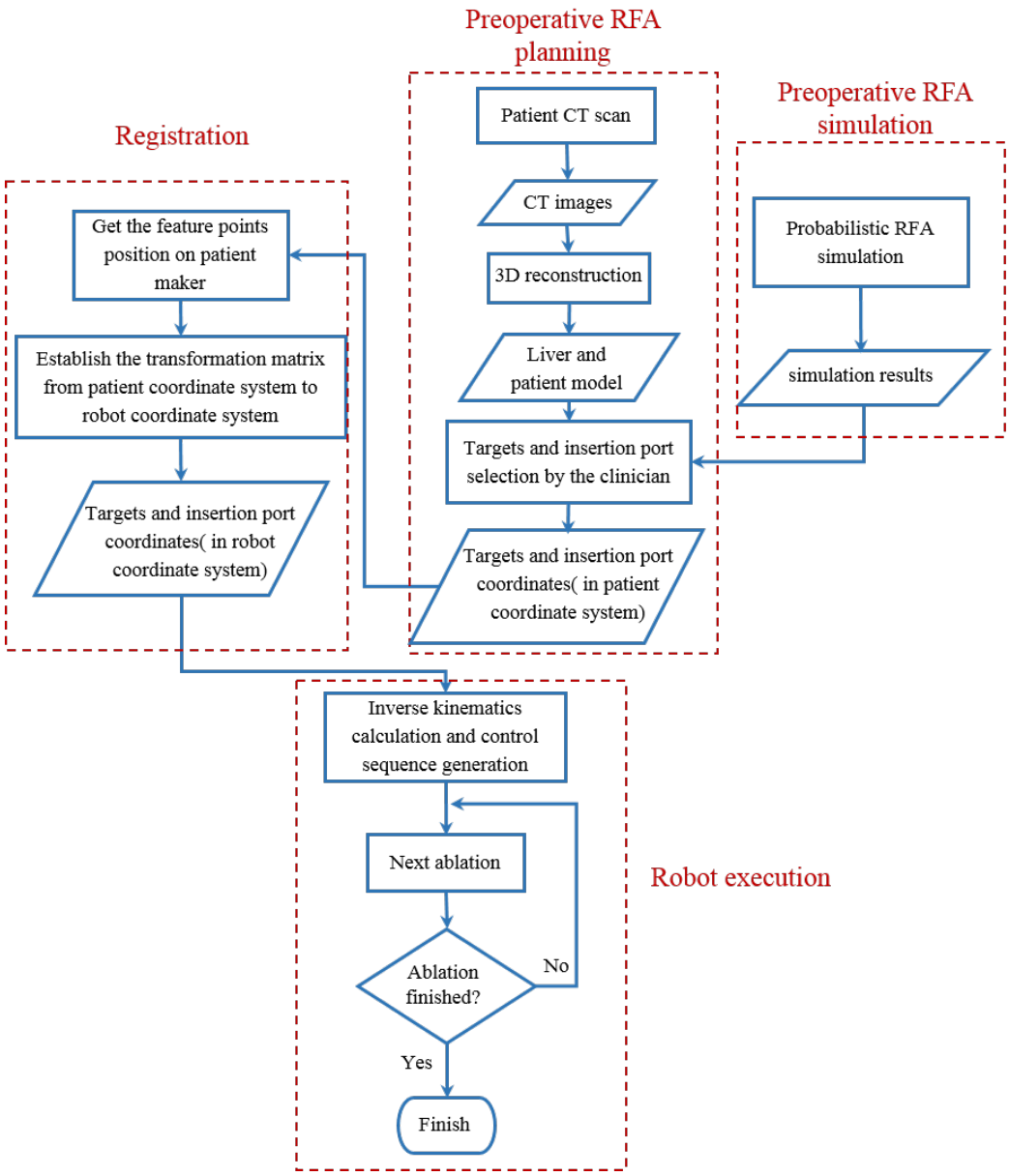

Figure 6.3: Work-flow of the experiment.

tient arrives at the CT room, the L-shape marker is attached to the patient. The patient is then send to do CT scan with the marker. A RFA planning software (see Figure 6.4) is used to process the 2D CT images. The planning software is

able to reconstruct the 3D model of the patient and establish a marker-based coordinate system. The clinician is allowed to choose the insertion port and ablation targets from the software. The positions of the insertion port and the targets

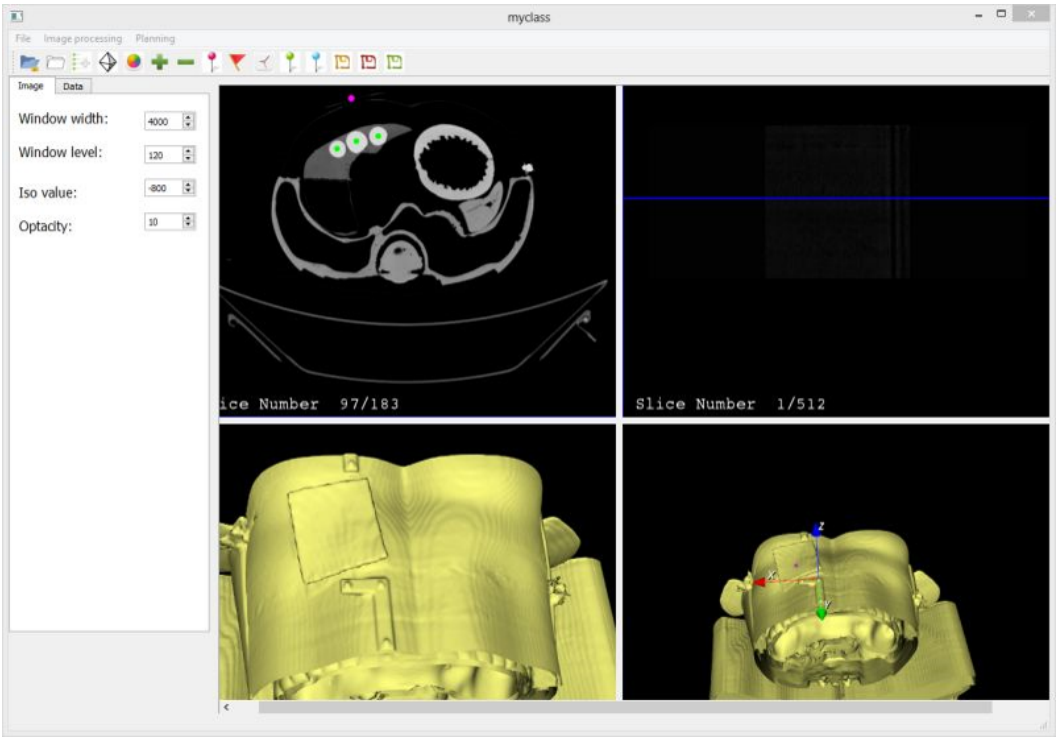

Figure 6.4: The RFA planning software.

with respect to the patient coordinate system can be exported as the input of patient-robot registration. Registration is then conducted by targeting feature points on the patient marker. The transformation matrix from patient coordinate system to the robot coordinate system is established. The position of the insertion port and the targets are thus converted to the robot coordinate system. Inverse kinematics is conducted to calculate the joints' variable values for each target. A user interface (see Figure 6.5) is designed to control the RFA needle insertion process. By using the control software, the robot can be moved either manually or automatically. In manual control mode, the robot can be controlled by defining each joint variable command. This mode can be used in testing the

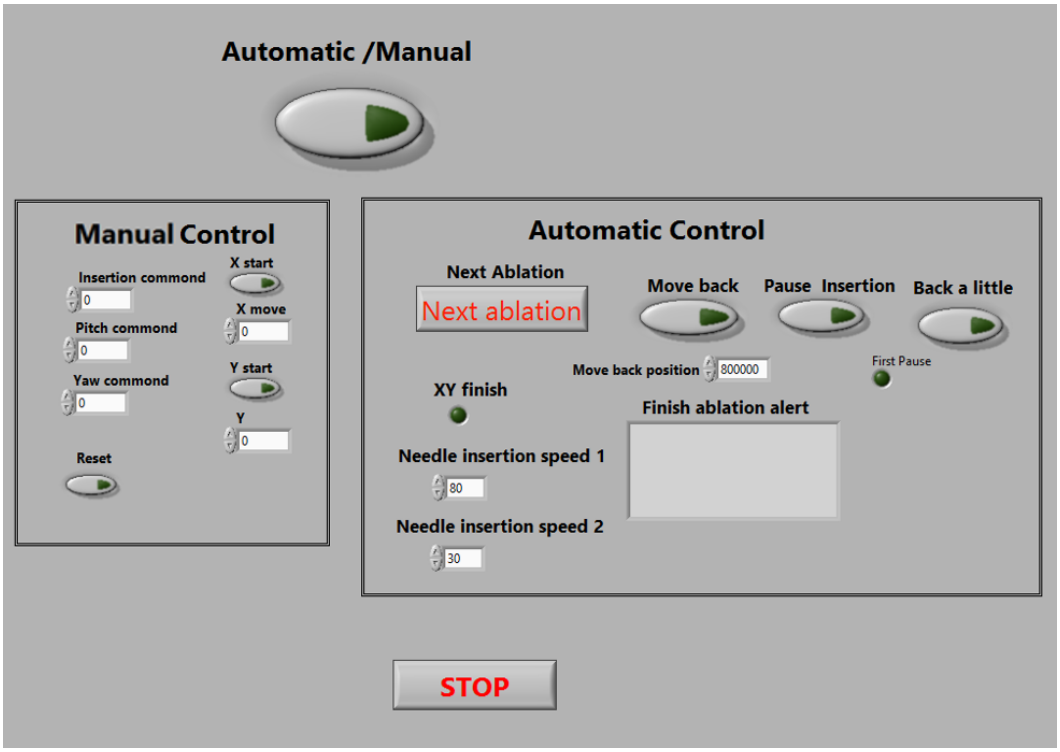

Figure 6.5: Robot control interface.

robot. In automatic control mode, the software obtains ablation data from outside and moves the RFA needle automatically. Some control functions, such as "move back", "pause" and "insertion speed", are integrated to the automatic control mode. In this RFA needle insertion experiment, the control software read the ablation data calculated from registration process and automatic control mode is used during the experiment. During needle insertion, the direction of RFA needle is first adjusted and then inserted after the needle orientation is ascertained. When the needle moves close to the patient skin, insertion is paused to allow the clinician to cut a small incision for the needle to go in. In the in-vivo experiment, the RFA generator is turned on for two minutes after the needle reaches the ablation target. The needle is moved back after one ablation is done. This ablation process is repeated for every ablation until all targets have been ablated.

6.3 Ex-vivo Experiment on Phantom Model

This section presents the results of the RFA needle insertion experiment conducted on a human phantom. The phantom used for this experiment is shown in Figure 6.6. The liver model in the phantom was replaced by a silicon liver to allow the RFA needle to go inside. A mold is fabricated using 3D printer to build the silicon liver. As shown in Figure 6.7(a), the mold is used to build the top half of the liver. For our RFA needle insertion experiment, only the top half silicon liver is sufficient. The bottom half of the liver is solid so that it can support the top half and keep the liver stable in the human phantom (see Figure 6.7(b)). To

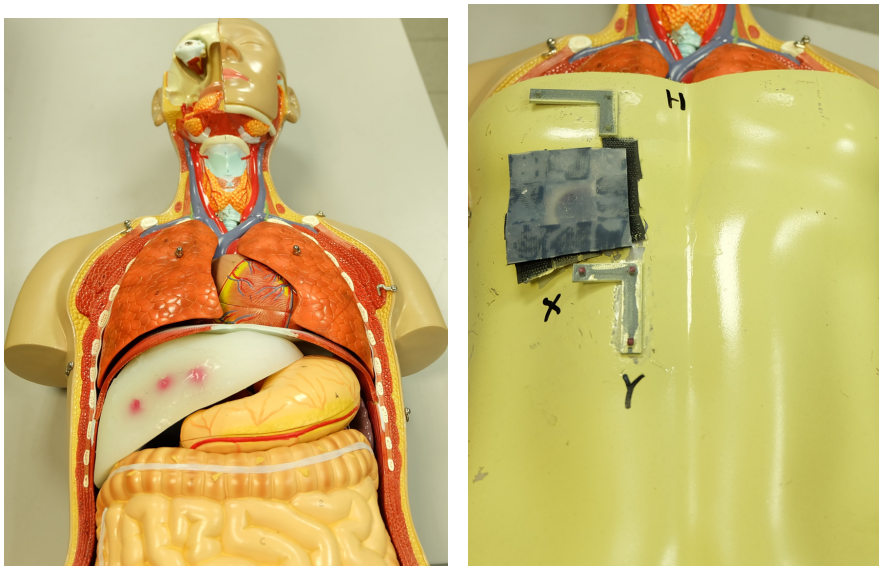

(a) (b)

Figure 6.6: Phantom model used in the experiment. (a)Inside of the phantom model. (b) Phantom cover with a small silicon skin to mimic the human skin.

mimic the tumor and make it easy to select targets in the RFA planning, three fake tumors made of red clay balls are also included in the silicon liver (see Figure 6.7(c)). On the cover of the phantom, a small hole is cut to allow the RFA needle to go through and a piece of fake skin made of silicon is attached on top of the hole to simulate human skin (see Figure 6.6(b)). A L-shape marker is also attached

to the phantom to establish the patient coordinate system.

(a) (b) (c)

Figure 6.7: Fabrication of the liver in phantom test. (a) Liver mold for top half of the liver. (b) Bottom half of the liver model (solid). (b) Silicon half liver using the liver mold with three red clay balls as the tumor.

The CT images of the phantom are used to construct the 3D model of the phantom and establish the marker-based patient coordinate system (see Figure 6.8). By establishing the marker-based coordinate system, all the planning data can be expressed in this coordinate system. The ablation targets are selected

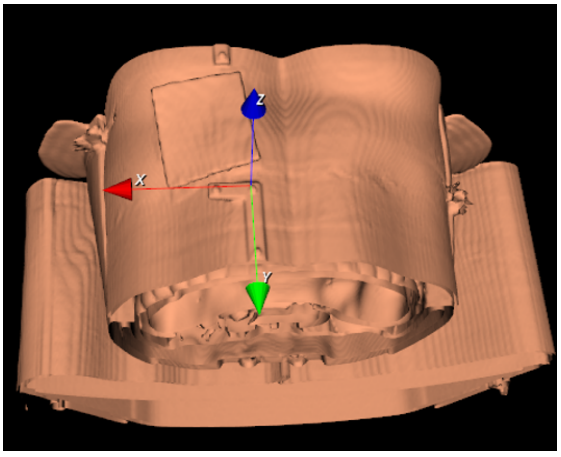

Figure 6.8: Reconstructed 3D phantom model from CT image and marker based patient coordinate system.

as the centers of the three clay balls and the insertion port are selected on the silicon skin. As shown in Figure 6.9(a), the insertion port and targets can be selected in 2D CT images. The red dot indicates the selected insertion port and the green dots indicate the selected targets. The 3D planning effect is shown in figure 6.9(b). The red dot indicates the selected insertion port and the green

balls indicate the ablation spheres on the targets. The results of this ex-vivo

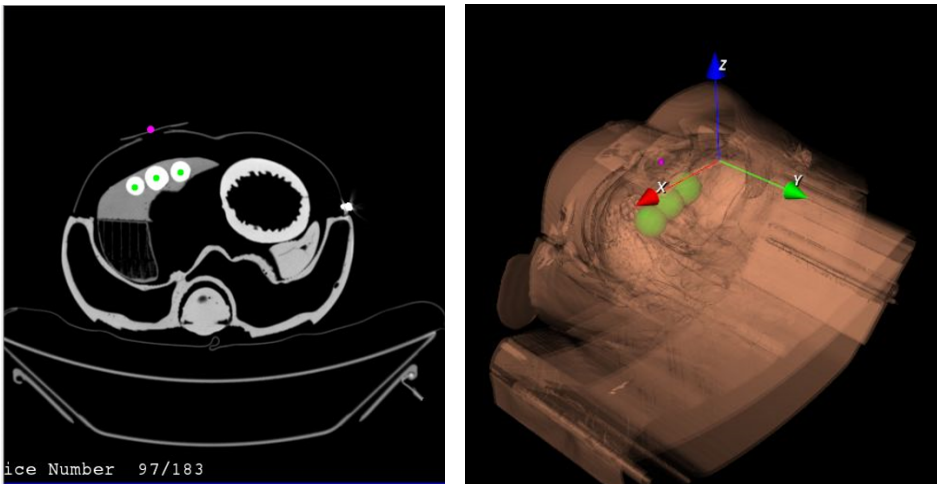

(a) (b)

Figure 6.9: Preoperative planning for phantom test (a)Selected insertion port (red dot) and targets (green dots) on 2D slice. (b) Insertion port (red dot) and targets (green balls) in the patient coordinate system.

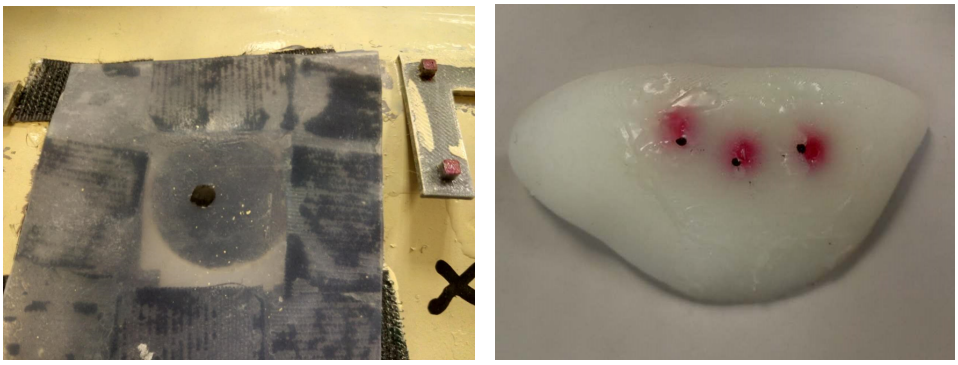

(a) (b)

Figure 6.10: Phantom test results (a) Actual insertion port (black dot) on the skin. (b) Actual entry ports (black dots) on the liver.

phantom test is shown in Figure 6.10. As shown in Figure 6.10(a), the three insertions all go through a single insertion port (as indicated by the black dot). Figure 6.10(b) shows the silicon liver after the experiment. The three black dots indicate the three entry points to the liver. From their positions and the direction of the RFA needle, we can assert that the RFA needle has reached the three targets

as planned. After the experiment, the fake tumors were taken out from the silicon liver. To demonstrate the accuracy of this experiment, each tumor was split along the insertion trajectory (see Figure 6.11). Since our targets were at the centers of the tumors, the execution errors can be measured approximately. Table 6.1 shows the execution errors in targeting the tumors. The errors are acceptable in the application of RFA needle insertion.

Figure 6.11: Insertion trajectory inside the fake tumor.

Table 6.1: Execution errors for in the tumors.

Tumor Number	Execution error(Unit: mm)
Tumor 1	1.5
Tumor 2	1.2
Tumor 1	2.1

6.4 In-vivo Experiment on Porcine Model

To test the system feasibility in real clinical environment, an in-vivo experiment on porcine model was conducted (see Figure 6.12). Since breath of the pig can affect the position of the targets in liver and also the insertion port on the skin, the breath of the pig is hold during the CT scan and RFA process. To make the internal organs' positions during the RFA the same as those in the CT image, CT scan and the RFA were both conducted during the inhale phase of the pig. As in the phantom experiment, a L-shape marker is attached to the patient before the

CT scan. Figure 6.13 shows the reconstructed 3D porcine model from CT images.

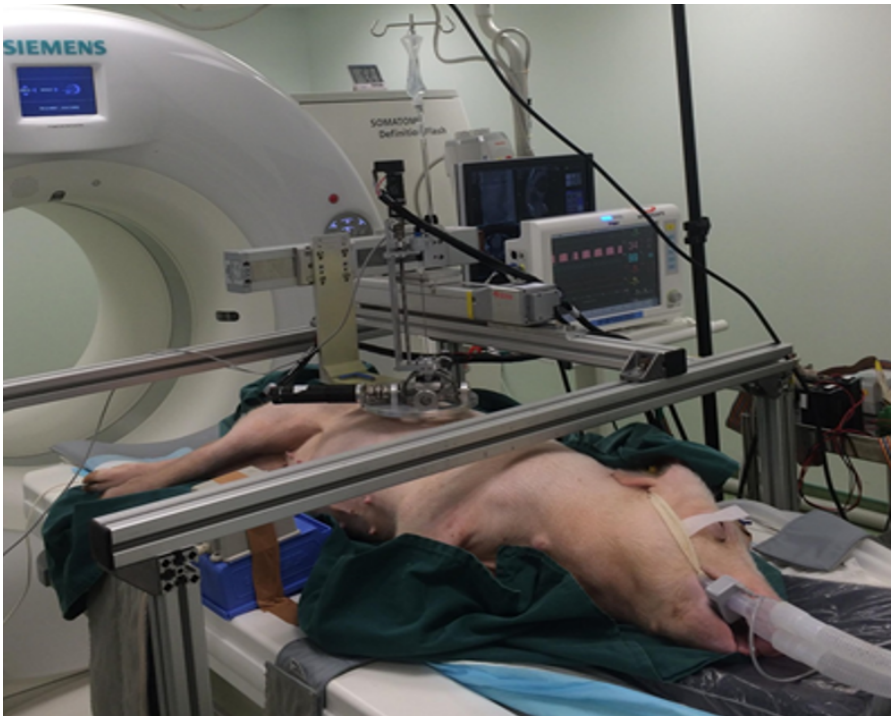

Figure 6.12: an in-vivo experiment on porcine model.

Patient coordinate system (see Figure 6.13) can also be established based on the marker features. In this in-vivo experiment, the RFA planning was conducted

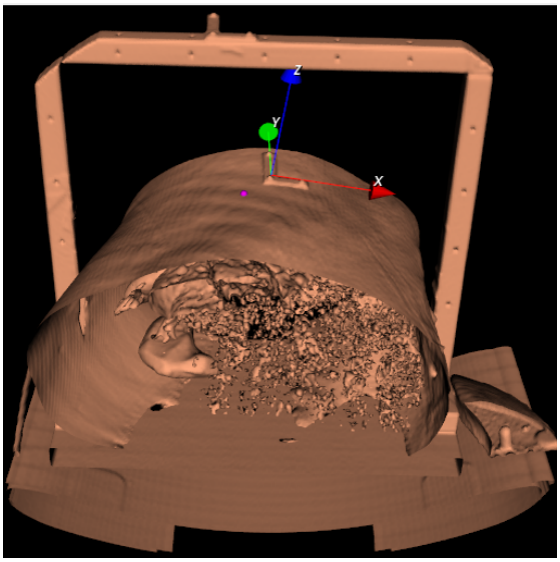

Figure 6.13: Reconstructed 3D porcine model from CT image and marker based patient coordinate system.

by the clinician. By using our planning software (see Figure 6.4), clinician was allowed to select the insertion port and ablation targets in the 2D CT image (see Figure 6.14(a)). After the selection, they can check the plan by inspecting the predicted outcomes on the 3D model (see Figure 6.14(b)).

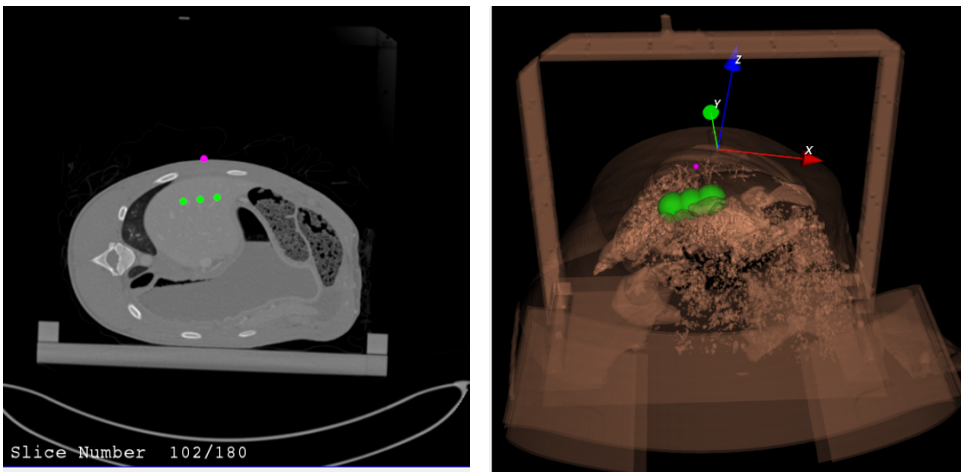

(a) (b)

Figure 6.14: Preoperative planning for porcine model test (a)Selected insertion port (red dot) and targets (green dots) on 2D slice. (b) Insertion port (red dot) and targets (green balls) in the patient coordinate system.

Figure 6.15 shows the results of the in-vivo experiment on porcine model. In this experiment, the clinician selected three locations to conduct RFA. In each location, one insertion port and three targets were selected. From Figure 6.15(a), we can observe that there are three small incisions left on the patient skin. On the liver, we can observe that three separate RFA lesion zones (see Figure 6.15(b)). Each lesion zone consists of three sequential RFA lesions.

This in-vivo experiment shows that our RFA needle insertion system is able to conduct multiple RFAs through a single insertion port. The target ablation volume can be covered by the RFA lesions as we planned in preoperative stage. The feasibility and effectiveness of our system has been proven. Table 6.2 presents the duration for successful targeting one ablation. The times for the robot are measured from our experiment and the times for manual ablation are obtained from

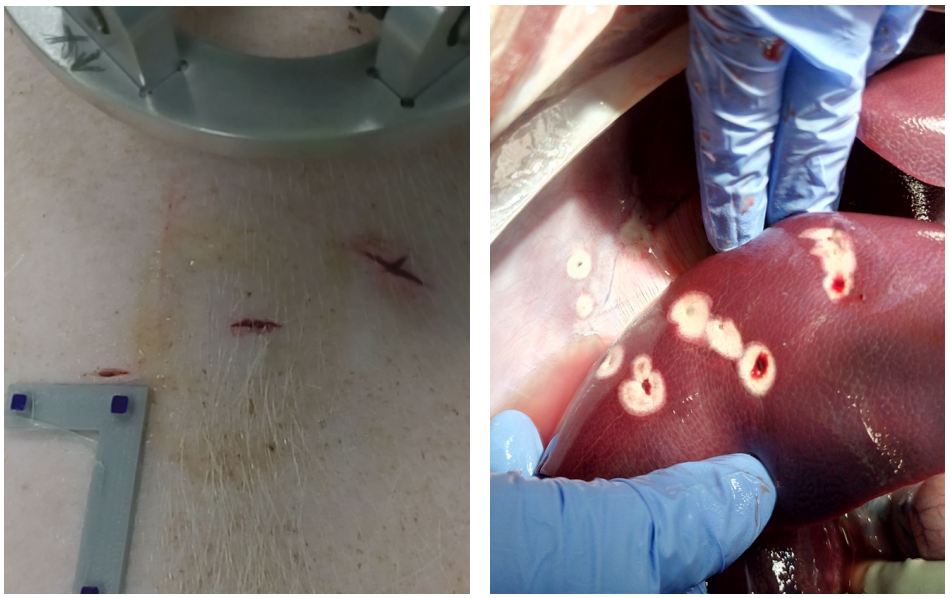

(a) (b)

Figure 6.15: Porcine test results (a) Insertion ports on the skin. (b) Ablation results on the liver.

Patriciu's study [16]. Since our robotic execution depends on the pre-operative planning data, we do not need to do CT scan for every insertion. We can observe that the targeting time for robot is much less than the time for manual ablation. The robotic RFA needle insertion is thus more efficient than manual ablation.

Table 6.2: Time for successful targeting (min)

	Mean	STD	Max	Min
Robotic	0.43	0.04	0.51	0.38
Manual	8.57	1.99	12	6

6.5 Summary

In this chapter, an ex-vivo experiment on phantom model and an in-vivo experiment on porcine model are presented to test the feasibility and effectiveness of our RFA needle insertion robot system in clinical environment. The experimental setup and work flow are introduced. Pre-operative planning, registration and

intra-operative robot execution were conducted to test the whole system. During in-vivo experiment, the liver is ablated after the needle insertion. The ablation result were evaluated by the clinician. The ex-vivo and in-vivo experimental results demonstrated that our robot system is able to conduct multiple RFAs with minimal incision effectively and efficiently. Our system demonstrates good potential for percutaneous RFA of large liver tumor.

Chapter 7

Conclusion and Future Work

Three main issues related to computer-aided and robot-assisted RFA of large liver tumor, i.e. preoperative simulation and planning, robotic RFA execution, and surgical registration, are investigated in this research. A computer-aided and robot-assisted RFA needle insertion system was built to implement and test our methods. Ex-vivo and in-vivo experimental results show that our RFA needle insertion system is capable of conducting RFA procedure for large liver tumor with small incision. For the patients who are not physically fit to undergo liver resection, the computer-aided and robot-assisted RFA needle insertion system offers them an alternative. Hence, their chance of survival can be increased.

The probabilistic RFA simulation method we proposed takes account of the intrinsic variations of liver tissue and shows that the temperature inside the liver tissue follows normal distribution. Compared to previous studies about RFA simulation, our study improves the reliability of current RFA simulations. The probabilistic nature of biological tissue is revealed, and this probabilistic method can be useful for other simulations on biological tissue.

To achieve 'Remote Center of Motion (RCM)' of the RFA needle and realize single insertion port on patient skin, a novel spherical mechanism was designed

and implemented. A new kinematic analysis method was proposed in our study. This method overcomes the limitations of previous methods. To realize smooth motion of the manipulator during RFA needle insertion, an integrative speed and position control strategy was also investigated. The ex-vivo experiment proves that the RFA needle insertion robot is able to do multiple RFA needle insertions through a single insertion port accurately and efficiently, showing that this robot is capable of executing multiple RFAs for large liver tumor treatment.

Registration is a process that synthesizes the preoperative planning data and the real surgical environment. The accuracy of the RFA needle insertion largely depends on the accuracy of registration. A novel L-shape marker-based registration method was proposed to transform the computed tomography (CT) image data to the robot coordinate system. This method establishes the transformation between the patient coordinate system and robot coordinate system by finding the feature points of the patient marker using the robot. This method works well in our system but has limitations for other robot systems. Therefore, a generic vision-based registration was also proposed. The experiment results showed that both registration methods can achieve the required accuracy in RFA for liver tumor based on the clinician's feedback.

However, it should be noted that our study also has some limitations. Firstly, some assumptions was used in the RFA simulation model. For example, we assumed that the temperature on the liver surface and the initial temperature of the liver is always $37°C$. We also assumed that the voltage on the liver surface is zero. These assumptions may not be accurate in real situation, and they may lead to inaccuracy of the model. As far as we know, all the models for liver have some simplifications and assumptions. This is because human liver is a very complex organ and it is almost impossible to model it exactly. However, for our RFA planning application, this model can provide enough information. Secondly,

our study does not take into account the deformation of liver and RFA needle. When the RFA needle is inserted to the liver, both the needle and the liver will be deformed. The temperature change during RFA could also cause deformation of the tissue [9]. The deformation of liver and RFA needle could affect the accuracy of RFA needle insertion. This deformation process is very hard to model because the initial condition for each insertion is different and it is impossible to model it when we do not know the initial condition. Nevertheless, the error caused by the deformation is acceptable because we always ablate more volume than the actual tumor volume to make sure the tumor is completely destroyed and we are targeting large tumors. In addition, real-time image feedback is still needed to monitor any possible accident during the RFA process even when we have preoperative RFA planning.

In order to make the RFA needle insertion robot be routinely used in clinic, several improvements are required in our prototype system. Firstly, our robotic RFA needle insertion are purely based on preoperative CT data. Therefore, real-time feedback of patient images for example, via intraoperative ultrasound imaging should be incorporated into the RFA needle insertion system. With real-time feedback, we can avoid possible complications such as damaging of vital organs during RFA execution. Secondly, the human-machine interface should also be optimized to provide clear guidance to the clinician and clinical team. Finally, more animal experiments are required to test the safety, precision and stability of our system.

List of Publications

Journal Publications

1. **B. Duan**, R. Wen, Y. Fu, K. J. Chua, C. K. Chui, Probabilistic Finite Element Method for Large Tumor Radiofrequency Ablation Simulation and Planning [J]. Medical Engineering & Physic. (2016)

2. P. Liu, **B. Duan**, Q. Wang, J. Qin, J. L. Peneyra, K. Y. Chang, C. K. Chui, P. A. Heng, A Human-machine Collaborative RFA system of Large Tumor with Single Incision [J]. IEEE Transactions on Biomedical Engineering. (Under review)

Patent

1. C. K. Chui, R. Wen, **B. Duan** and Y. Fu, Method of Probabilistic Finite Element Modelling for Radiofrequency Ablation Treatment Planning, Singapore Patent Application 10201402356S, 15 May 2014

Conference Proceedings

1. **B. Duan**, C. K. Chui, K. J. Chua, (2014). Integrated RF and Cryo ablation of Liver Tumor for Computer Integrated Surgery. In the 15th International Conference on Biomedical Engineering, ICBME (pp. 500-503)

2. **B. Duan**, Y. Fu, K. J. Chua, C. K. Chui, (2014). Probabilistic Modeling

and Simulation of Thermal Ablation, in the 10th Anniversary Asian Conference on Computer Aided Surgery.

3. **B. Duan**, R. Wen, C. B. Chng, W. Wang, P. Liu, J. Qin, L. B. Jonnathan, C. stephen, P. A. Heng, C. K. Chui, (2015, October). Image-guided robotic system for radiofrequency ablation of large liver tumor with single incision. In Ubiquitous Robots and Ambient Intelligence (URAI), 2015 12th International Conference on (pp. 284-289). IEEE.

4. **B. Duan**, C. K. Chui, (2016). Multiscale Modeling of Liver Bio-impedance and Frequency Control for Radiofrequency Ablation. In TENCON 2016-2016 IEEE Region 10 Conference. IEEE (Under review)

5. C. B. Chng, **B. Duan**, C. K. Chui, (2016). Modeling and Simulation of a Remote Center of Motion Mechanism. In TENCON 2016-2016 IEEE Region 10 Conference. IEEE (Under review)

6. X. Tan, C. B. Chng, **B. Duan**, Y. Ho, K. B. Lim, C. K. Chui, (2016).In 2013 IEEE International Conference on Systems, Man, and Cybernetics (pp. 1582-1587). IEEE. (Accepted)

Bibliography

[1] F. X. Bosch, J. Ribes, M. Díaz, and R. Cléries, "Primary liver cancer: worldwide incidence and trends," *Gastroenterology*, vol. 127, no. 5, pp. S5–S16, 2004.

[2] M. W. Miller and M. C. Ziskin, "Biological consequences of hyperthermia," *Ultrasound Med boil*, vol. 15, no. 8, pp. 707–722, 1989.

[3] S. K. Chang, W. W. Hlaing, L. Yang, and C. K. Chui, "Current technology in navigation and robotics for liver tumours ablation," *Ann Acad Med Singapore*, vol. 40, no. 5, p. 231, 2011.

[4] S. N. Goldberg, G. S. Gazelle, L. Solbiati, T. Livraghi, K. Tanabe, P. Hahn, and P. Mueller, "Ablation of liver tumors using percutaneous rf therapy." *AJR. American journal of roentgenology*, vol. 170, no. 4, pp. 1023–1028, 1998.

[5] D. Choi, H. K. Lim, S. H. Kim, W. J. Lee, H.-J. Jang, J. Y. Lee, S. W. Paik, K. C. Koh, and J. H. Lee, "Hepatocellular carcinoma treated with percutaneous radio-frequency ablation: Usefulness of power doppler us with a microbubble contrast agent in evaluating therapeutic response–preliminary results 1," *Radiology*, vol. 217, no. 2, pp. 558–563, 2000.

[6] M. J. K. Blomley, R. Coulden, P. Dawson, M. Kormano, P. Donlan, C. Bufkin, and M. J. Lipton, "Liver perfusion studied with ultrafast ct," *J Comput Assist Tomogr*, vol. 19, no. 3, pp. 424–433, 1995.

[7] C. K. Chui, E. Kobayashi, X. Chen, T. Hisada, and I. Sakuma, "Combined

compression and elongation experiments and non-linear modelling of liver tissue for surgical simulation," *Med Biol Eng Comput*, vol. 42, no. 6, pp. 787–798, 2004.

[8] D. Haemmerich, I. d. Santos, D. J. Schutt, J. G. Webster, and D. M. Mahvi, "In vitro measurements of temperature-dependent specific heat of liver tissue," *Med Eng Phys*, vol. 28, no. 2, pp. 194–197, 2006.

[9] W. H. Huang, C. K. Chui, E. Kobayashi, S. H. Teoh, and S. Chang, "Multi-scale model for investigating the electrical properties and mechanical properties of liver tissue undergoing ablation," *Int J Comput Assist Radiol Surg*, vol. 6, no. 5, pp. 601–607, 2011.

[10] V. M. Nahirnyak, S. W. Yoon, and C. K. Holland, "Acousto-mechanical and thermal properties of clotted blood," *J Acoust Soc Am*, vol. 117, no. 4, pp. 2413–2413, 2005.

[11] U. Zurbuchen, C. Holmer, K. S. Lehmann, T. Stein, A. Roggan, C. Seifarth, H.-J. Buhr, and J.-P. Ritz, "Determination of the temperature-dependent electric conductivity of liver tissue ex vivo and in vivo: Importance for therapy planning for the radiofrequency ablation of liver tumours," *Int J Hyperth*, vol. 26, no. 1, pp. 26–33, 2010.

[12] R. H. Taylor and P. Kazanzides, "Medical robotics and computer-integrated interventional medicine," *Advances in Computers*, vol. 73, pp. 219–260, 2008.

[13] R. H. Taylor and D. Stoianovici, "Medical robotics in computer-integrated surgery," *Robotics and Automation, IEEE Transactions on*, vol. 19, no. 5, pp. 765–781, 2003.

[14] C.-H. Kuo and J. S. Dai, "Robotics for minimally invasive surgery: a historical review from the perspective of kinematics," in *International Symposium on History of Machines and Mechanisms*. Springer, 2009, pp. 337–354.

[15] G. Zong, X. Pei, J. Yu, and S. Bi, "Classification and type synthesis of 1-

dof remote center of motion mechanisms," *Mechanism and Machine Theory*, vol. 43, no. 12, pp. 1585–1595, 2008.

[16] A. Patriciu, M. Awad, S. B. Solomon, M. Choti, D. Mazilu, L. Kavoussi, and D. Stoianovici, "Robotic assisted radio-frequency ablation of liver tumors–randomized patient study," in *International Conference on Medical Image Computing and Computer-Assisted Intervention*. Springer, 2005, pp. 526–533.

[17] L. Yang, R. Wen, J. Qin, C. K. Chui, K. B. Lim, and S. Y. Chang, "A robotic system for overlapping radiofrequency ablation in large tumor treatment," *IEEE/ASME Trans Mechatron*, vol. 15, no. 6, pp. 887–897, 2010.

[18] L. R. Jiao, G. Navarra, J.-C. Weber, R. Havlic, J. P. Nicholls, and N. A. Habib, "Radio frequency assisted liver resection: the habib?s technique," in *Liver and Pancreatic Diseases Management*. Springer, 2006, pp. 31–37.

[19] T. Livraghi, S. N. Goldberg, F. Monti, A. Bizzini, S. Lazzaroni, F. Meloni, S. Pellicano, L. Solbiati, and G. S. Gazelle, "Saline-enhanced radio-frequency tissue ablation in the treatment of liver metastases." *Radiology*, vol. 202, no. 1, pp. 205–210, 1997.

[20] S. N. Goldberg, G. S. Gazelle, L. Solbiati, W. J. Rittman, and P. R. Mueller, "Radiofrequency tissue ablation: increased lesion diameter with a perfusion electrode," *Academic radiology*, vol. 3, no. 8, pp. 636–644, 1996.

[21] J. P. McGahan, W.-Z. Gu, J. M. Brock, H. Tesluk, and C. D. Jones, "Hepatic ablation using bipolar radiofrequency electrocautery," *Academic radiology*, vol. 3, no. 5, pp. 418–422, 1996.

[22] I. Chang, "Finite element analysis of hepatic radiofrequency ablation probes using temperature-dependent electrical conductivity," *Biomedical engineering online*, vol. 2, no. 1, p. 12, 2003.

[23] S. Tungjitkusolmun, S. T. Staelin, D. Haemmerich, J.-Z. Tsai, H. Cao,

J. G. Webster, F. T. Lee Jr, D. M. Mahvi, and V. R. Vorperian, "Three-dimensional finite-element analyses for radio-frequency hepatic tumor ablation," *Biomedical Engineering, IEEE Transactions on*, vol. 49, no. 1, pp. 3–9, 2002.

[24] M. K. Jain and P. D. Wolf, "A three-dimensional finite element model of radiofrequency ablation with blood flow and its experimental validation," *Annals of biomedical engineering*, vol. 28, no. 9, pp. 1075–1084, 2000.

[25] I. Chang and U. Nguyen, "Thermal modeling of lesion growth with radiofrequency ablation devices," *Biomed Eng OnLine*, vol. 3, no. 1, p. 27, 2004.

[26] C.-C. R. Chen, M. I. Miga, and R. L. Galloway Jr, "Optimizing electrode placement using finite-element models in radiofrequency ablation treatment planning," *Biomedical Engineering, IEEE Transactions on*, vol. 56, no. 2, pp. 237–245, 2009.

[27] S. Labonté, "A computer simulation of radio-frequency ablation of the endocardium," *Biomedical Engineering, IEEE Transactions on*, vol. 41, no. 9, pp. 883–890, 1994.

[28] S. Labonte, "Numerical model for radio-frequency ablation of the endocardium and its experimental validation," *Biomedical Engineering, IEEE Transactions on*, vol. 41, no. 2, pp. 108–115, 1994.

[29] E. J. Berjano, J. Saiz, and J. M. Ferrero, "Radio-frequency heating of the cornea: theoretical model and in vitro experiments," *Biomedical Engineering, IEEE Transactions on*, vol. 49, no. 3, pp. 196–205, 2002.

[30] E. Berjano, J. Saiz, J. Alio, and J. Ferrero, "Ring electrode for radio-frequency heating of the cornea: Modelling andin vitro experiments," *Medical and Biological Engineering and Computing*, vol. 41, no. 6, pp. 630–639, 2003.

[31] E. J. Berjano and F. Hornero, "Thermal-electrical modeling for epicardial

atrial radiofrequency ablation," *Biomedical Engineering, IEEE Transactions on*, vol. 51, no. 8, pp. 1348–1357, 2004.

[32] E. J. Berjano, J. L. Alió, and J. Saiz, "Modeling for radio-frequency conductive keratoplasty: implications for the maximum temperature reached in the cornea," *Physiological measurement*, vol. 26, no. 3, p. 157, 2005.

[33] H. Cao, M. A. Speidel, J.-Z. Tsai, M. S. Van Lysel, V. R. Vorperian, and J. G. Webster, "Fem analysis of predicting electrode-myocardium contact from rf cardiac catheter ablation system impedance," *Biomedical Engineering, IEEE Transactions on*, vol. 49, no. 6, pp. 520–526, 2002.

[34] D. Haemmerich, L. Chachati, A. S. Wright, D. M. Mahvi, F. T. Lee Jr, and J. G. Webster, "Hepatic radiofrequency ablation with internally cooled probes: effect of coolant temperature on lesion size," *Biomedical Engineering, IEEE Transactions on*, vol. 50, no. 4, pp. 493–500, 2003.

[35] Y.-C. Lai, Y. B. Choy, D. Haemmerich, V. R. Vorperian, and A. G. Webster, "Lesion size estimator of cardiac radiofrequency ablation at different common locations with different tip temperatures," *Biomedical Engineering, IEEE Transactions on*, vol. 51, no. 10, pp. 1859–1864, 2004.

[36] S. Tungjitkusolmun, E. Woo, H. Cao, J. Tsai, V. Vorperian, and J. Webster, "Thermal-electrical finite element modelling for radio frequency cardiac ablation: effects of changes in myocardial properties," *Medical and Biological Engineering and Computing*, vol. 38, no. 5, pp. 562–568, 2000.

[37] D. E. Haines and D. D. Watson, "Tissue heating during radiofrequency catheter ablation: a thermodynamic model and observations in isolated perfused and superfused canine right ventricular free wall," *Pacing and Clinical Electrophysiology*, vol. 12, no. 6, pp. 962–976, 1989.

[38] M. G. Curley and P. S. Hamilton, "Creation of large thermal lesions in liver using saline-enhanced rf ablation," in *Engineering in Medicine and Biology*

Society, 1997. Proceedings of the 19th Annual International Conference of the IEEE, vol. 6, Oct 1997, pp. 2516–2519 vol.6.

[39] H. H. Pennes, "Analysis of tissue and arterial blood temperatures in the resting human forearm," *Journal of applied physiology*, vol. 1, no. 2, pp. 93–122, 1948.

[40] J. A. Mechling and J. W. Strohbehn, "A theoretical comparison of the temperature distributions produced by three interstitial hyperthermia systems," *International Journal of Radiation Oncology* Biology* Physics*, vol. 12, no. 12, pp. 2137–2149, 1986.

[41] D. E. Haines and D. D. Watson, "Tissue heating during radiofrequency catheter ablation: a thermodynamic model and observations in isolated perfused and superfused canine right ventricular free wall," *Pacing and Clinical Electrophysiology*, vol. 12, no. 6, pp. 962–976, 1989.

[42] S. Labonte, "Numerical model for radio-frequency ablation of the endocardium and its experimental validation," *Biomedical Engineering, IEEE Transactions on*, vol. 41, no. 2, pp. 108–115, 1994.

[43] D. Haemmerich, S. Tungjitkusolmun, S. T. Staelin, F. T. Lee Jr, D. M. Mahvi, and J. G. Webster, "Finite-element analysis of hepatic multiple probe radio-frequency ablation," *Biomedical Engineering, IEEE Transactions on*, vol. 49, no. 8, pp. 836–842, 2002.

[44] D. Haemmerich, A. W. Wright, D. M. Mahvi, F. T. Lee Jr, and J. G. Webster, "Hepatic bipolar radiofrequency ablation creates coagulation zones close to blood vessels: a finite element study," *Med Biol Eng Comput*, vol. 41, no. 3, pp. 317–323, 2003.

[45] D. Haemmerich, T. Staelin, S. Tungjitkusolmun, F. T. Lee Jr, D. M. Mahvi, and J. G. Webster, "Hepatic bipolar radio-frequency ablation between separated multiprong electrodes," *IEEE Trans Biomed Eng*, vol. 48, no. 10, pp.

1145–1152, 2001.

[46] E. J. Berjano, J. Saiz, and J. M. Ferrero, "Radio-frequency heating of the cornea: theoretical model and in vitro experiments," *Biomedical Engineering, IEEE Transactions on*, vol. 49, no. 3, pp. 196–205, 2002.

[47] E. Berjano, J. Saiz, J. Alio, and J. Ferrero, "Ring electrode for radio-frequency heating of the cornea: Modelling andin vitro experiments," *Medical and Biological Engineering and Computing*, vol. 41, no. 6, pp. 630–639, 2003.

[48] E. J. Berjano, J. L. Alió, and J. Saiz, "Modeling for radio-frequency conductive keratoplasty: implications for the maximum temperature reached in the cornea," *Physiological measurement*, vol. 26, no. 3, p. 157, 2005.

[49] R. Plonsey and D. B. Heppner, "Considerations of quasi-stationarity in electrophysiological systems," *The Bulletin of mathematical biophysics*, vol. 29, no. 4, pp. 657–664, 1967.

[50] J. D. Doss, "Calculation of electric fields in conductive media," *Medical physics*, vol. 9, no. 4, pp. 566–573, 1982.

[51] M. Ahmed, Z. Liu, S. Humphries, and N. Goldberg, "Computer modeling of the combined effects of perfusion, electrical conductivity, and thermal conductivity on tissue heating patterns in radiofrequency tumor ablation," *Int J Hyperthermia*, vol. 24, no. 7, pp. 577–588, 2008.

[52] S. Tungjitkusolmun, E. Woo, H. Cao, J. Tsai, V. Vorperian, and J. Webster, "Thermal-electrical finite element modelling for radio frequency cardiac ablation: effects of changes in myocardial properties," *Med Biol Eng Comput*, vol. 38, no. 5, pp. 562–568, 2000.

[53] T. Kröger, T. Pätz, I. Altrogge, A. Schenk, K. Lehmann, B. Frericks, J.-P. Ritz, H.-O. Peitgen, and T. Preusser, "Fast estimation of the vascular cooling in rfa based on numerical simulation," *Open Biomed Engin J*, vol. 4,

p. 16, 2010.

[54] M. H. Chen, W. Yang, K. Yan, W. Gao, Y. Dai, L. Huo, S. Y. Shan, Z. Hui, and R. T. P. Poon, "Treatment strategy to optimize radiofrequency ablation for liver malignancies," *J Vasc Interv Radiol*, vol. 17, no. 4, pp. 671–683, 2006.

[55] G. Dodd, M. Frank, M. Aribandi, S. Chopra, and K. Chintapalli, "Radiofrequency thermal ablation computer analysis of the size of the thermal injury created by overlapping ablations," *Am J Roentgenol*, vol. 177, no. 4, pp. 777–782, 2001.

[56] S. A. Nicolau, X. Pennec, L. Soler, X. Buy, A. Gangi, N. Ayache, and J. Marescaux, "An augmented reality system for liver thermal ablation: Design and evaluation on clinical cases," *Med Image Anal*, vol. 13, no. 3, pp. 494–506, 2009.

[57] Y. S. Khajanchee, D. Streeter, L. L. Swanstrom, and P. D. Hansen, "A mathematical model for preoperative planning of radiofrequency ablation of hepatic tumors," *Surg Endosc*, vol. 18, no. 4, pp. 696–701, 2004.

[58] C. Baegert, C. Villard, P. Schreck, and L. Soler, "Multi-criteria trajectory planning for hepatic radiofrequency ablation," in *Medical Image Computing and Computer-Assisted Intervention ? MICCAI 2007*. Springer Berlin Heidelberg, 2007, vol. 4792, no. number, pp. 676–684.

[59] I. Altrogge, T. Preusser, T. Kroger, S. Haase, T. Patz, and M. Kirby, "Sensitivity analysis for the optimization of radiofrequency ablation in the presence of material parameter uncertainty," *Int J Uncertain Quantif*, vol. 2, no. 3, 2012.

[60] A. M. Hasofer and N. C. Lind, "Exact and invariant second-moment code format," *J Eng Mech Division*, vol. 100, no. 1, pp. 111–121, 1974.

[61] Y. G. Zhao and A. H. S. Ang, "System reliability assessment by method of

moments," *J Struct Eng*, vol. 129, no. 10, pp. 1341–1349, 2003.

[62] J. Hu, K. D. Klinich, C. S. Miller, J. D. Rupp, G. Nazmi, M. D. Pearlman, and L. W. Schneider, "A stochastic visco-hyperelastic model of human placenta tissue for finite element crash simulations," *Ann Biomed Eng*, vol. 39, no. 3, pp. 1074–1083, 2011.

[63] A. Delalleau, G. Josse, and J. M. Lagarde, "Dual-parameter optimisation of the elastic properties of skin," *Comput Methods Biomech Biomed*, vol. 15, no. 1, pp. 83–92, 2012.

[64] I. D. Santos, D. Haemmerich, D. Schutt, A. F. da Rocha, and L. R. Menezes, "Probabilistic finite element analysis of radiofrequency liver ablation using the unscented transform," *Phys Med Biol*, vol. 54, no. 3, p. 627, 2009.

[65] W. H. Huang and C. K. Chui, "A radio-frequency ablation planning system using stochastic finite element method," in *System Integration (SII), 2012 IEEE/SICE International Symposium on*, Dec 2012, pp. 603–608.

[66] B. Davies, "A review of robotics in surgery," *Proceedings of the Institution of Mechanical Engineers, Part H: Journal of Engineering in Medicine*, vol. 214, no. 1, pp. 129–140, 2000.

[67] A. R. Lanfranco, A. E. Castellanos, J. P. Desai, and W. C. Meyers, "Robotic surgery: a current perspective," *Annals of surgery*, vol. 239, no. 1, pp. 14–21, 2004.

[68] Y. S. Kwoh, J. Hou, E. A. Jonckheere, and S. Hayati, "A robot with improved absolute positioning accuracy for ct guided stereotactic brain surgery," *IEEE Transactions on Biomedical Engineering*, vol. 35, no. 2, pp. 153–160, 1988.

[69] S. Lavallee, J. Troccaz, L. Gaborit, P. Cinquin, A.-L. Benabid, and D. Hoffmann, "Image guided operating robot: a clinical application in stereotactic neurosurgery," in *Robotics and Automation, 1992. Proceedings., 1992 IEEE*

International Conference on. IEEE, 1992, pp. 618–624.

[70] G. H. Ballantyne and F. Moll, "The da vinci telerobotic surgical system: the virtual operative field and telepresence surgery," *Surgical Clinics of North America*, vol. 83, no. 6, pp. 1293–1304, 2003.

[71] J. Marescaux and F. Rubino, "The zeus robotic system: experimental and clinical applications," *Surgical Clinics of North America*, vol. 83, no. 6, pp. 1305–1315, 2003.

[72] M. Schurr, G. Buess, B. Neisius, and U. Voges, "Robotics and telemanipulation technologies for endoscopic surgery," *Surgical endoscopy*, vol. 14, no. 4, pp. 375–381, 2000.

[73] P. Dario, M. C. Carrozza, and A. Pietrabissa, "Development and in vitro testing of a miniature robotic system for computer-assisted colonoscopy," *Computer Aided Surgery*, vol. 4, no. 1, pp. 1–14, 1999.

[74] T. Hu, A. E. Castellanos, G. Tholey, and J. P. Desai, "Real-time haptic feedback in laparoscopic tools for use in gastro-intestinal surgery," in *International Conference on Medical Image Computing and Computer-Assisted Intervention*. Springer, 2002, pp. 66–74.

[75] G. Tholey, T. Chanthasopeephan, T. Hu, J. P. Desai, and A. Lau, "Measuring grasping and cutting forces for reality-based haptic modeling," in *International Congress Series*, vol. 1256. Elsevier, 2003, pp. 794–800.

[76] C. W. Kennedy, T. Hu, and J. P. Desai, "Combining haptic and visual servoing for cardiothoracic surgery," in *Robotics and Automation, 2002. Proceedings. ICRA'02. IEEE International Conference on*, vol. 2. IEEE, 2002, pp. 2106–2111.

[77] C. W. Kennedy and J. P. Desai, "A vision-based approach for estimating contact forces: Applications to robot-assisted surgery," *Applied Bionics and Biomechanics*, vol. 2, no. 1, pp. 53–60, 2005.

[78] U. Hagn, R. Konietschke, A. Tobergte, M. Nickl, S. Jörg, B. Kübler, G. Passig, M. Gröger, F. Fröhlich, U. Seibold *et al.*, "Dlr mirosurge: a versatile system for research in endoscopic telesurgery," *International journal of computer assisted radiology and surgery*, vol. 5, no. 2, pp. 183–193, 2010.

[79] L. Yang, C. Chng, C. Chui, and D. Lau, "Model-based design analysis for programmable remote center of motion in minimally invasive surgery," in *Robotics Automation and Mechatronics (RAM), 2010 IEEE Conference on.* IEEE, 2010, pp. 84–89.

[80] A. Faraz and S. Payandeh, "A robotic case study: optimal design for laparoscopic positioning stands," *The International Journal of Robotics Research*, vol. 17, no. 9, pp. 986–995, 1998.

[81] T. A. Rockall, "The da vinci telerobotic surgical system," *Primer of robotic & telerobotic surgery. Philadelphia: Lippincott Williams & Wilkins*, pp. 57–60, 2004.

[82] F. R. Jacques Marescaux, "The zeus robotic system: experimental and clinical applications," *Surgical Clinics of North America*, pp. 1305–1315, 2003.

[83] M. J. Lum, J. Rosen, M. N. Sinanan, and B. Hannaford, "Optimization of a spherical mechanism for a minimally invasive surgical robot: theoretical and experimental approaches," *Biomedical Engineering, IEEE Transactions on*, vol. 53, no. 7, pp. 1440–1445, 2006.

[84] P. Mederic, V. Pasqui, and G. Morel, "Preliminary results on the design of a novel laparoscopic manipulator," *the Proc. of 11thWorld Congr. Mechanism and Machine Science*, 2004.

[85] R. Kurtz and V. Hayward, "Multiple-goal kinematic optimization of a parallel spherical mechanism with actuator redundancy," *Robotics and Automation, IEEE Transactions on*, vol. 8, no. 5, pp. 644–651, 1992.

[86] M. Ouerfelli and V. Kumar, "Optimization of a spherical five-bar parallel

drive linkage," *Journal of mechanical design*, vol. 116, no. 1, pp. 166–173, 1994.

[87] M. J. Lum, J. Rosen, M. N. Sinanan, and B. Hannaford, "Kinematic optimization of a spherical mechanism for a minimally invasive surgical robot," in *Robotics and Automation, 2004. Proceedings. ICRA'04. 2004 IEEE International Conference on*, vol. 1. IEEE, 2004, pp. 829–834.

[88] C.-H. Kuo and J. S. Dai, "Kinematics of a fully-decoupled remote center-of-motion parallel manipulator for minimally invasive surgery," *Journal of Medical Devices*, vol. 6, no. 2, p. 021008, 2012.

[89] Y. Fu, G. Niu, B. Pan, K. Li, and S. Wang, "Design and optimization of remote center motion mechanism of minimally invasive surgical robotics," in *ROBIO'13*, 2013, pp. 774–779.

[90] F. Y. Wu, M. Torabi, A. Yamada, A. Golden, G. S. Fischer, K. Tuncali, D. D. Frey, and C. Walsh, "An mri coil-mounted multi-probe robotic positioner for cryoablation," in *ASME 2013 International Design Engineering Technical Conferences and Computers and Information in Engineering Conference*. American Society of Mechanical Engineers, 2013, pp. V06AT07A012–V06AT07A012.

[91] H. Kang, "Robotic assisted suturing in minimally invasive surgery," Ph.D. dissertation, Rensselaer Polytechnic Institute, 2002.

[92] H. Kang and J. T. Wen, "Robotic assistants aid surgeons during minimally invasive procedures," *Engineering in Medicine and Biology Magazine, IEEE*, vol. 20, no. 1, pp. 94–104, 2001.

[93] ——, "Endobot: a robotic assistant in minimally invasive surgeries," in *Robotics and Automation, 2001. Proceedings 2001 ICRA. IEEE International Conference on*, vol. 2. IEEE, 2001, pp. 2031–2036.

[94] C. Bernard, H. Kang, S. K. Singh, and J. T. Wen, "Robotic system for

collaborative control in minimally invasive surgery," *Industrial Robot: An international Journal*, vol. 26, no. 6, pp. 476–484, 1999.

[95] T. Yang, J. Liu, W. Huang, L. Yang, C. K. Chui, M. H. Ang Jr, Y. Su, and S. K. Chang, "Mechanism of a learning robot manipulator for laparoscopic surgical training," in *Frontiers of Intelligent Autonomous Systems*. Springer, 2013, pp. 297–308.

[96] C. J. Walsh, N. C. Hanumara, A. H. Slocum, J.-A. Shepard, and R. Gupta, "A patient-mounted, telerobotic tool for ct-guided percutaneous interventions," *Journal of Medical Devices*, vol. 2, no. 1, p. 011007, 2008.

[97] C. J. Walsh, N. Hanumara, A. Slocum, R. Gupta, and J.-A. Shepard, "Evaluation of a patient-mounted, remote needle guidance and insertion system for ct-guided, percutaneous lung biopsies," in *ASME 2007 2nd Frontiers in Biomedical Devices Conference*. American Society of Mechanical Engineers, 2007, pp. 39–40.

[98] D.-K. Yoon, J.-T. Seo, E.-J. Jung, and B.-J. Yi, "Automatic lighting system using multiple robotic lamps," *IEEE/ASME Transactions on Mechatronics*, vol. 19, no. 3, pp. 963–974, 2014.

[99] L. G. Brown, "A survey of image registration techniques," *ACM computing surveys (CSUR)*, vol. 24, no. 4, pp. 325–376, 1992.

[100] J. A. Maintz and M. A. Viergever, "A survey of medical image registration," *Medical image analysis*, vol. 2, no. 1, pp. 1–36, 1998.

[101] S. C. Strother, J. R. Anderson, X.-L. Xu, J.-S. Liow, D. C. Bonar, and D. A. Rottenberg, "Quantitative comparisons of image registration techniques based on high-resolution mri of the brain." *Journal of computer assisted tomography*, vol. 18, no. 6, pp. 954–962, 1994.

[102] P. F. Hemler, P. A. van den Elsen, T. S. Sumanaweera, S. Napel, J. Drace, and J. R. Adler, "A quantitative comparison of residual error for three dif-

ferent multimodality registration techniques," in *Information processing in medical imaging*. Ile Berder, France: IPMI, Kluwer, 1995, pp. 251–62.

[103] D. Vandermeulen, A. Collignon, J. Michiels, H. Bosmans, P. Suetens, G. Marchal, G. Timmens, P. Van den Elsen, M. Viergever, H. Ehricke *et al.*, "Multi-modality image registration within covira," *STUDIES IN HEALTH TECHNOLOGY AND INFORMATICS*, vol. 19, pp. 29–42, 1995.

[104] T. Peters, B. Davey, P. Munger, R. Comeau, A. Evans, and A. Olivier, "Three-dimensional multimodal image-guidance for neurosurgery," *IEEE Transactions on medical imaging*, vol. 15, no. 2, pp. 121–128, 1996.

[105] C. R. Maurer, J. M. Fitzpatrick, R. L. Galloway, M. Y. Wang, R. J. Maciunas, and G. S. Allen, "The accuracy of image-guided neurosurgery using implantable fiducial markers," in *Computer assisted radiology*. Berlin: Springer-Verlag, 1995, pp. 1197–1202.

[106] S. Li, C. A. Pelizzari, and G. T. Chen, "Unfolding patient motion with biplane radiographs," *Medical physics*, vol. 21, no. 9, pp. 1427–1433, 1994.

[107] D. Simon, R. O?toole, M. Blackwell, F. Morgan, A. DiGioia, and T. Kanade, "Accuracy validation in image-guided orthopaedic surgery," in *Proceedings of the Second International Symposium on Medical Robotics and Computer Assisted Surgery*, vol. 6. Citeseer, 1995, pp. 185–192.

[108] R. Ellis, D. Caramella, and M. M. Fadda, "A biocompatible fiducial marker for evaluating the accuracy of ct image registration," in *Investigative Radiology*. Citeseer, 1996.

[109] W. D. Leslie, A. Borys, D. McDonald, J. O. Dupont, and A. E. Peterdy, "External reference markers for the correction of head rotation in brain single-photon emission tomography," *European journal of nuclear medicine*, vol. 22, no. 4, pp. 351–355, 1995.

[110] S. J. Stapleton, C. B. Caldwell, L. E. Ehrliche, C. L. Leonhardt, S. E.

Black, and M. J. Yaffe, "Effects of non-linear flow and spatial orientation on technetium-99m hexamethylpropylene amine oxime single-photon emission tomography," *European journal of nuclear medicine*, vol. 22, no. 9, pp. 1009–1016, 1995.

[111] M. Y. Wang, J. M. Fitzpatrick, C. R. Maurer Jr, and R. J. Maciunas, "Automatic technique for localizing externally attached markers in mr and ct volume images of the head," in *Medical Imaging 1994*. International Society for Optics and Photonics, 1994, pp. 214–224.

[112] G. E. Christensen, A. A. Kane, J. L. Marsh, and M. W. Vannier, "Synthesis of an individualized cranial atlas with dysmorphic shape," in *Mathematical Methods in Biomedical Image Analysis, 1996., Proceedings of the Workshop on*. IEEE, 1996, pp. 309–318.

[113] D. Vandermeulen, A. Collignon, J. Michiels, H. Bosmans, P. Suetens, G. Marchal, G. Timmens, P. Van den Elsen, M. Viergever, H. Ehricke *et al.*, "Multi-modality image registration within covira," *STUDIES IN HEALTH TECHNOLOGY AND INFORMATICS*, vol. 19, pp. 29–42, 1995.

[114] R. Rubinstein, H. Karger, U. Pietrzyk, T. Siegal, J. M. Gomori, and R. Chisin, "Use of 201 thallium brain spect, image registration, and semi-quantitative analysis in the follow-up of brain tumors," *European journal of radiology*, vol. 21, no. 3, pp. 188–195, 1996.

[115] G. Rizzo, M. C. Gilardi, A. Prinster, F. Grassi, G. Scotti, S. Cerutti, and F. Fazio, "An elastic computerized brain atlas for the analysis of clinical pet/spet data," *European journal of nuclear medicine*, vol. 22, no. 11, pp. 1313–1318, 1995.

[116] P. B. Hoffer, "Difference images calculated from ictal and interictal technetium-. 99m-hmpao specit scans of epilepsy," 1995.

[117] C. Davatzikos, J. L. Prince, and R. N. Bryan, "Image registration based on

boundary mapping," *IEEE Transactions on medical imaging*, vol. 15, no. 1, pp. 112–115, 1996.

[118] L. G. Brown and T. E. Boult, "Registration of planar film radiographs with computed tomography," in *Mathematical Methods in Biomedical Image Analysis, 1996., Proceedings of the Workshop on.* IEEE, 1996, pp. 42–51.

[119] T. M. Lehmann, C. Goerke, W. Schmitt, A. Kaupp, and R. Repges, "Rotation-extended cepstrum technique optimized by systematic analysis of various sets of x-ray images," in *Medical Imaging 1996.* International Society for Optics and Photonics, 1996, pp. 390–401.

[120] L. Chmielewski and D. Kozinska, "Image registration," in *conf. Computer Pattern Recognition SystemsKOSYR*, 2003, pp. 26–29.

[121] H. Shekarforoush, M. Berthod, and J. Zerubia, "Subpixel image registration by estimating the polyphase decomposition of cross power spectrum," in *Computer Vision and Pattern Recognition, 1996. Proceedings CVPR'96, 1996 IEEE Computer Society Conference on.* IEEE, 1996, pp. 532–537.

[122] E. De Castro and C. Morandi, "Registration of translated and rotated images using finite fourier transforms." *IEEE Transactions on pattern analysis and machine intelligence*, vol. 9, no. 5, p. 700, 1987.

[123] A. Collignon, D. Vandermeulen, P. Suetens, and G. Marchal, "3d multi-modality medical image registration using feature space clustering," in *Computer Vision, Virtual Reality and Robotics in Medicine.* Springer, 1995, pp. 195–204.

[124] D. Hawkes, C. Ruff, D. Hill, C. Studholme, P. Edwards, and W. Wong, "3d multimodal imaging in image guided interventions," *STUDIES IN HEALTH TECHNOLOGY AND INFORMATICS*, vol. 19, pp. 83–100, 1995.

[125] A. Patriciu, S. Solomon, L. Kavoussi, and D. Stoianovici, "Robotic kidney and spine percutaneous procedures using a new laser-based ct registra-

tion method," in *International Conference on Medical Image Computing and Computer-Assisted Intervention*. Springer, 2001, pp. 249–257.

[126] R. H. Taylor, B. D. Mittelstadt, H. A. Paul, W. Hanson, P. Kazanzides, J. F. Zuhars, B. Williamson, B. L. Musits, E. Glassman, and W. L. Bargar, "An image-directed robotic system for precise orthopaedic surgery," *IEEE Transactions on Robotics and Automation*, vol. 10, no. 3, pp. 261–275, 1994.

[127] A. M. DiGioia III, B. Jaramaz, and B. D. Colgan, "Computer assisted orthopaedic surgery: Image guided and robotic assistive technologies." *Clinical orthopaedics and related research*, vol. 354, pp. 8–16, 1998.

[128] S. A. Curley, "Radiofrequency ablation of malignant liver tumors," *Ann Surg Oncol*, vol. 10, no. 4, pp. 338–347, 2003.

[129] H. Arkin, L. X. Xu, and K. R. Holmes, "Recent developments in modeling heat transfer in blood perfused tissue," *IEEE Trans Biomed Eng*, vol. 41, no. 2, pp. 97–107, 1994.

[130] R. Agah, J. A. Pearce, A. J. Welch, and M. Motamedi, "Rate process model for arterial tissue thermal damage: Implications on vessel photocoagulation," *Lasers in surgery and medicine*, vol. 15, no. 2, pp. 176–184, 1994.

[131] D. J. Schutt and D. Haemmerich, "Effects of variation in perfusion rates and of perfusion models in computational models of radio frequency tumor ablation," *Med Phys*, vol. 35, no. 8, pp. 3462–3470, 2008.

[132] B. Huang and X. Du, "Probabilistic uncertainty analysis by mean-value first order saddlepoint approximation," *Reliab Eng Syst Safe*, vol. 93, no. 2, pp. 325–336, 2008.

[133] Y. B. Fu, C. K. Chui, and C. L. Teo, "Liver tissue characterization from uniaxial stress–strain data using probabilistic and inverse finite element methods," *J Mech Behav Biomed Mater*, vol. 20, no. 0, pp. 105–112, 2013.

[134] J. W. Valvano, J. R. Cochran, and K. R. Diller, "Thermal conductivity

and diffusivity of biomaterials measured with self-heated thermistors," *Int J Thermophys*, vol. 6, no. 3, pp. 301–311, 1985.

[135] H. L. Anderson, *Metropolis, Monte Carlo, And the Maniac.* Los Alamos Sci, 1986.

[136] K. Ding, Z. Zhou, and C. Liu, "Latin hypercube sampling used in the calculation of the fracture probability," *Reliab Eng Syst Safety*, vol. 59, no. 2, pp. 239–242, 1998.

[137] J. C. Helton and F. J. Davis, "Latin hypercube sampling and the propagation of uncertainty in analyses of complex systems," *Reliab Eng Syst Safety*, vol. 81, no. 1, pp. 23–69, 2003.

Appendix

Video Links

1. **Robot accuracy test**
   https://youtu.be/cAoy0lAOsVc
2. **Single insertion point demonstration**
   https://youtu.be/N5PzMugtKYM
3. **Ex-vivo experiment on human phantom**
   https://youtu.be/mdHRlur_8aw
4. **In-vivo experiment on porcine model**
   https://youtu.be/MFcsQuhQudg